Injection and Evaporation of 100% methanol

Experimental and simulation-based research into the injection and evaporation of 100% methanol for use in a port-injected spark-ignited ICE

Thesis Report

C.J. van Iersel

Injection and Evaporation of 100% methanol

Experimental and simulation-based research into the injection and evaporation of 100% methanol for use in a port-injected spark-ignited ICE

by

ing. C.J. van Iersel

to obtain the degree of Master of Science
at the Delft University of Technology,
to be defended publicly on Monday November 28, 2022 at 10:00 AM.

An electronic version of this thesis is available at `http://repository.tudelft.nl/`.

The photograph on the cover is taken by the author and shows a post-processed image of an ethanol spray entering the evaporation chamber.

T̃U Delft

This page intentionally left blank.

Preface

Coming from a family with a long history in the merchant and Royal Netherlands Navy, I have always been around ships and the ocean. From this followed my own passion for ships, together with an eagerness to learn new things and solve problems. This combination led to my choice to follow in my father's footsteps and become a merchant sailor. Enjoying everything I had learned so far, I followed this up with the Master in Marine Technology. During this program I participated in courses of the specialisations Marine Engineering, Maritime Operations and Management, Ship Design, and Ship and Offshore Structures. The free electives were filled with as many maritime related courses available; such as Introduction to Offshore Engineering, Turbomachinery, and Arctic Engineering. As a final step, a Marine Engineering thesis would have only been suitable, with its main focus on the injection and evaporation of 100% methanol.

This thesis would not have been possible without the help and support of a number of people. First of all, I want to thank the Netherlands Defence Academy (NLDA) for offering me a graduation position, together with the additional guidance and support. I want to give a special thanks to Robert van de Ketterij and Rinze Geertsma for their excellent guidance throughout this thesis. In our weekly meetings you always gave me your critical opinions and helped me make the next steps and pushing the boundaries. Not only did this help with the research, but I also really enjoyed working with you and learned a lot from your experiences. Moreover, I want to thank the laboratory staff; Chris Dijkstra and Marcel Roberscheuten for their help and guidance in the performed experimental research, and express my gratitude to SGT(TD) L.R. van der Kooij and SGT(TD) J. Krieger in building the experimental setup and giving feedback on my design iterations.

From the Delft University of Technology, I want to thank Peter de Vos for introducing me to this project and the NLDA. Subsequently, I would like to thank Klaas Visser for giving feedback and asking questions during all the milestone meetings. I also want to express my gratitude to the secretary of the Marine Technology department for all scheduled appointments and process-related information.

Ultimately, I want to thank everyone around me for their love and support. This includes my family and friends, for both distraction and support in my time at the TU Delft. Last, a special thanks to my girlfriend, who is my biggest support.

C.J. van Iersel
Delft, November 2022

Abstract

The maritime sector faces major challenges to reduce its impact on global warming. The use of methanol as a fuel alternative is considered one of the more promising options to be implemented in a relatively short to medium time frame; based on the potential availability, emission reduction, energy density, potential to be synthetically produced, scalability of production, and its implementation on board ships (both new build and retrofitted).

This report investigates potential improvements of the injection system, to achieve complete evaporation in the air inlet of a port-fuel injection engine to avoid wall-wetting of the scavenger air receiver and inlet valve. As a result, the methanol-air mixture in the cylinder would become more homogeneous and able to provide 100% of the rated engine power. Earlier research indicated that the wall-wetting fuel film and its evaporation rate directly affect the air-fuel ratio of the in-cylinder mixture, stability of the combustion process, and overall engine performance. The study includes the development of an injection model simulating low-pressure port-fuel injection, similar to the system fitted on our Caterpillar test engine, and the development of a single-droplet evaporation model to gain inside into the evaporation process of 100% methanol.

Based on the performed experimental research, we conclude the average droplet size ranges between 100 and 120μm. The average droplet speed was determined at ±35 m/s and the spray angle at 20°. At room temperature and pressure, the injection spray ended against the back-glass of the evaporation chamber, indicating almost none of the ethanol evaporates under these conditions. The injection length exceeds at least ±40 cm at atmospheric temperature and pressure, which is in line with the results of the single-droplet evaporation model.

Keywords: *injection, evaporation, methanol, port-fuel injection, experiment, shadowgraphy*

Contents

List of Figures

List of Tables

Nomenclature

Abbreviations

AFR | A/F	Air to fuel ratio
BDC - BBDC / ABDC	Bottom Dead Center - Before/After
BTE	Brake Thermal Efficiency
CFD	Computational Fluid Dynamics
CI	Compression Ignition
CO_2	Carbon dioxide
DI	Direct injection
ECU	Electrical Control Unit
GHG	Greenhouse gases
GMM	Green Maritime Methanol
HFO	Heavy fuel oil
HRR	Heat Release Rate
ICE	Internal Combustion Engine
IMO	International Maritime Organisation
LHV	Lower Heating Value
LNG	Liquefied Natural Gas
M100	100% methanol
MDO	Marine diesel oil
MGO	Marine gas oil
MVFP	Mean Value First Principle
ND | N-D	Neutral Density
NG	Natural Gas
NPN	Negative-positive-negative
OEM	Original Equipment Manufacturers
PFI	Port-fuel injected
PFI	Port-fuel injection
PNP	Positive-negative-positive
RPM	Revolutions per minute
SFC	Specific Fuel Consumption
SI	Spark-Ignition
STP	Standard temperature and pressure
TDC - BTDC/ATDC	Top Dead Center - Before/After
TRA	Task Risk Analysis
UHC	Unburned hydrocarbons
ULSD	Ultra-Low-Sulphur-Diesel

Greek Symbols

α	Spray angle	[°]
η	Efficiency	[-]
λ	Air excess ratio	[-]
ρ	Density	[kgm^{-3}]
σ	Stoichiometric air-to-fuel ratio	[-]

Symbols

A_0	Area droplet	$[m^2]$
afr	Air to fuel ratio	$[-]$
D_{AB}	Binary diffusion coefficient	$[m^2s^{-1}]$
CN	Cetane number	$[-]$
CRR	Combustion reaction rate	$[kgs^{-1}]$
d	Diameter droplet	$[m]$
K	Evaporation constant	$[m^2s^{-1}]$
$GAHRR$	Gross apparent heat release	$[kJs^{-1}]$
Q_{loss}	Heat loss	$[kJs^{-1}]$
Q_{evap}	Heat of vaporization	$[kJkg^{-1}]$
HRR	Heat release rate	$[kJs^{-1}]$
m	Mass	$[kg]$
$\dot{m}$	Massflow	$[kgs^{-1}]$
$NAHRR$	Net apparent heat release	$[kJs^{-1}]$
Pr	Prandtl number	$[-]$
p	Pressure	$[Pa]$
Re	Reynolds number	$[-]$
SMD	Sauter Mean Diameter	$[m]$
sfc	Specific fuel consumption	$[g(kWh)^{-1}]$
S_n	Stoichiometric number	$[-]$
T	Temperature	$[K]$
t	Time	$[s]$
V	Volume	$[m^3]$
$\dot{V}$	Volume flow	$[m^3s^{-1}]$
We	Weber number	$[-]$

<div style="text-align: right; font-size: 3em;">1</div>

Introduction

1.1. Background

The maritime sector faces major challenges to reduce its impact on global warming. As of 2022, the World Economic Outlook update of the International Monetary Fund (IMF) projected a continuing growth of the global economy [1]. The pre-COVID-19 predictions of the UN Conference on Trade and Development (UNCTAD) expected that the maritime trade continued to rise at an average annual growth rate of 3.4% up to 2024 [2]. These predictions will demanded even more from the shipping industry, which transport about 90% of the world trade. According to UK Research and Innovation [3] is the shipping industry, thereby, responsible for around 940 million tonnes of CO_2-emissions annually. This is at least 2.5% of the world's total CO_2 emissions. At the other end of the spectrum, regulations regarding CO_2 and other greenhouse gas (GHG) emissions increase. The tightening greenhouse gas regulations from the Paris Climate Accords and subsequent agreements of the International Maritime Organisation (IMO), require a reduction of 50% of CO_2-emissions from international shipping sector by 2050 compared to 2008. Therefore, the maritime sector faces tremendous challenges in meeting the set goals in GHG reduction and lowering its climate footprint.

In general, this means that the shipping industry needs to switch from fossil to non-fossil fuels, produced with renewable or zero-carbon energy sources [4]. Thus, developments into new fuel types for the shipping industry are required. However, different shipping sectors have different recommendations for their choice in fuel alternatives, both in the short and long term. This makes that the various shipping sectors play a key role in the decision which fuel alternative fits their requirements. For example, a ship operating on battery power is only useful when it is able to replenish within hours or days. For ships operating on hydrogen, this operational window is extended to approx. one week, while for methanol the operational window could be extended to approx. two weeks. In case longer operational windows are required, fossil fuel remains the main choice. In conclusion, autonomy is the key factor in the consideration which fuel alternative to use [5].

At this time, using methanol as fuel alternative is considered as one of the more promising options to be implemented in a relative short to medium time frame for ships requiring medium autonomy. This is based on the potential availability, emission reduction, energy density, potential to be synthetically produced, scalability of production, and implementation on board ships (both new-build and retrofitted). As an example, in August 2021, A.P. Moller - Maersk announced that they have ordered eight large ocean-going container vessels. The ships have a nominal capacity of approx. 16,000 TEU, capable of being operated on carbon neutral methanol and saving around one million tonnes of CO_2-emission annually [6].

As described by Van de Ketterij [7], using fossil-based methanol as energy carrier could reduce Tank-to-Wake[1] CO_2-emissions by up to 10% compared to Marine Diesel Oil (MDO), as well as improving air quality emissions such as SO_x, NO_x and PM. In addition, Well-to-Tank emissions and energy consumption are associated with the production, transportation, manufacturing and distribution of fuels. The Joint Research Centre of the European Commission provided a comprehensive overview for a large variety of fuels, and stated that the production method and feedstock dominates the overall Well-to-Tank emissions of any bio- or synthetic fuel [9]. However, with the use of renewable energy sources,

---

[1]The tank-to-wake approach solely looks at the emissions derived from on-board fuel combustion, referring only to the life cycle assessments of GHG emissions from the fuel in a ship's tank to the ship's exhaust [8]

the production of synthetic fuel could potentially reduce emissions up to 80%. Methanol showed a significant GHG reduction in Well-to-Tank and Tank-to-Wake emissions when produced from renewable energy and feedstocks [10].

The Green Maritime Methanol (GMM) project has been setup to investigate and research the challenges facing the maritime sector. It is based in the Netherlands and consists of a collaboration between important stakeholders; such as shipbuilders, shipping companies, engine manufacturers, research institutions and universities. Within this project, methanol is researched as a potential fuel alternative on board ships, to replace the current fossil fuels used. For this purpose, the NLDA and TU Delft perform research on a Caterpillar G3508A test-engine, in close collaboration with PON Power in Papendrecht. In this research the conversion to methanol and its implications on the performance and dynamic behaviour were investigated. The goal of these initial performance tests were to establish whether the engine could run stably at several loads and establish its fuel consumption and NO_x emissions, prior to performing more research to improve performance and investigate dynamic responsiveness of methanol fuelled spark ignition engines. The performance tests encountered three major challenges. First, they were unable to start the engine on 100% methanol, still requiring natural gas during a 5-second startup. Second, they were unable to load the engine to 100% rated power. A maximum of 430 kW (86% of maximum load) was reached, but a recommendation was given to modify the fuel system in order to accomplish this goal. Third, the fuel injector of cylinder four had to be replaced due to a malfunction. This gave deviating test results, but after replacement looked normal again. Another challenge present in the Caterpillar G3508A test-engine is the calculated (in-cylinder) evaporation of methanol. Bosklopper [11] described that an increased temperature after the cooler from 40°C to 60°C resulted in an increase in evaporated methanol at IVC from 18.0% vapour to 37.7%. The performance analyse showed a decrease of NO_x emissions at constant load and fuel consumption. Consequently, not all methanol evaporates in the scavenger air inlet. For port-fuel injection engines, injected fuel has a tendency to adsorb on the intake port wall because of the lower temperature and forms a wall-wetting fuel film. Research by Yao et al. [12] analysed the fuel dynamic transfer process, including fuel injection, fuel film deposition and evaporation rate in the intake port of a spark-ignition engine with port-fuel injection. They stated that the wall-wetting fuel film mass and its evaporation rate directly affected the air-fuel ratio of in-cylinder mixture, as well as the performance of the engine itself. This makes the evaporation of sufficient methanol and reducing its wall-wetting effect the limiting factor. It introduces the knowledge gap for this thesis, as currently research on the injection and evaporation of methanol in port-fuel injection conditions is lagging.

1.2. Research Objective

The objective of this thesis is to investigate how to improve the evaporation of methanol, in order to achieve injection and complete evaporation of methanol without causing wall-wetting. This would lead to a homogeneous methanol-air mixture in the cylinder that can provide 100% of rated engine power. The objective regarding injection entails the modelling on an injection model for 100% methanol as fuel. Currently, no research has been found on the modelling of low pressure injection valves, especially for the use of methanol. Thus, this thesis will improve on the previous studies by Zeng [13], Tol [14], and Bosklopper [11]. The objective regarding the evaporation of methanol entails a single-droplet evaporation model especially created for the evaporation of 100% methanol. This single-droplet evaporation model involves the spray development, droplet formation, evaporation, and required heat of vaporisation of the injected methanol. Thus, this thesis will improve on the previous study by Tol [14] that adopted a SMD approximation for methanol/diesel blends and in that neglected the droplet size distribution.

1.3. Research Questions

To support the primary research goal, the following main research question will be answered:

"How could the maximum evaporation of methanol inside the scavenger air inlet be obtained before the installed flame arrestor; by varying the injection pressure, inlet air temperature, spray dimensions, and droplet size?"

The main question can be broken into the following sub-questions, which address the injection of methanol:

1. How could the injector spray characteristics of methanol be improved by varying the injection pressure, inlet air temperature, spray dimensions, and droplet size?
2. How could the port-fuel injector be modelled in such a way that represents the injection of the Caterpillar G3508A test engine?

Subsequently, the following sub-questions will address the evaporation of methanol:

3. What is the influence of fine-spray port-fuel injectors on the evaporation process inside the scavenger air inlet?
4. What is the influence of the inlet air temperature on the evaporation process inside the scavenger air inlet?
5. How can the evaporation process of methanol inside scavenger air inlet be improved?
6. How could the evaporation process of methanol be modelled, using a single-droplet evaporation model?

To conclude, the following sub-question on modelling will be answered:

7. Does the evaporation model give comparable results, as found in the experimental data?

The scope of the above-mentioned sub-questions will only focus on the injection pressure, inlet air temperature, droplet size, and spray dimensions; i.e. injection length and injector selection possibilities. Additionally, modelling of the injection and evaporation of methanol will focus on the airflow speed, droplet size and distribution. This scope will provide a general outline of the research and prevent too much in-depth research on certain aspects or sub-questions during the duration of this graduation thesis.

1.4. Thesis Outline

This report has seven chapters required to answer the seven sub-questions and the research question. Each chapter begins with a brief explanation of the chapter-specific structure, and ends with a sub-conclusion and future developments. Chapter 2 elaborates on the research method of this report, which is based on a "three-stage rocket design"; each stage describes a specific topic of this report before moving on to the next stage. The next chapter, Chapter 3, will describe the theoretical framework behind port-fuel injection and the evaporation of liquid fuels. It will cover the spray structure and atomisation of the spray, the drop size distribution of the spray, and spray evaporation. Subsequently, a brief explanation is given on the injection spray characteristic and evaporation of methanol using port-fuel injection.

With the problem, research method and theoretical background known, it is possible to elaborate on the low-pressure injection model and creation the single-droplet evaporation model. In chapter 4, the development of a new low-pressure injection model is discussed, whereas chapter 5 covers the modelling of the single-droplet evaporation model for the evaporation of a pure liquid droplet suspended in its own vapour.

With both the low-pressure injection model and single-droplet evaporation model now covered, chapter 6 will describe the custom built experimental setup able to test various low-pressure injection nozzles at atmospheric pressure and temperature, as well as measure their individual spray characteristics and droplet size in those conditions using the shadowgraphy technique.

When all the sub-questions are answered, a discussion is started in chapter 7. The discussion makes the translation between the findings of this report and the real-time situation inside the engine. Especially, the results of the experiment and its influence on the engine regarding the lack of space in the inlet manifold. Lastly, the main research question is answered in chapter 8. Followed by some recommendations to improve upon the low-pressure injection model, single-droplet evaporation model, and custom built experimental setup.

2

Method

As previously described, the objective of this research is to optimise the injection and evaporation of methanol. The discovered knowledge gap on these two subjects is especially aimed at the fuel injection at lower pressures, as is the case with the port-fuel injection fitted on the test engine. In order to answer the previously mentioned research questions, this research method is based on a "three-stage rocket design"; each stage describing a specific topic of the thesis before moving on to the next stage. The first chapter, or stage, will describe the theoretical framework behind the injection and evaporation of liquid fuels in general, and methanol in more detail. Next, the modelling methods for both the injection model and single-droplet evaporation model will be briefly described. Finally, measurements will be performed and discussed using an experimental setup to subsequently verify and/or validate the single-droplet evaporation model. This measurement process and the adherent verification and/or validation method will be briefly described.

However, before this "three-stage rocket" will be described, a short system description of the test engine itself will be given. This system description describes the construction of the test engine with regard to the injection nozzle in the inlet air receiver, the flame arrestor, and the inlet valve.

2.1. System Description

Originally, the Caterpillar G3508A test engine is a turbocharged spark-ignited natural gas engine with eight cylinders and a rated power of 500 kW at 1500 rpm. However, the engine has been modified to run on methanol with the use of eight separate injection nozzles; each nozzle being installed off centre on the inlet air receiver of a cylinder.

Figures 2.1–2.2 give an overview of the inlet air receiver of the Caterpillar G3508A. Figure 2.1 visualises the scavenge airflow through the air receiver, showing the injection nozzle on top of the receiver itself. Figure 2.2 shows the arrangement of the inlet air receiver from the inside. It shows the off centre installation of the injection nozzle (blue arrow) – ±2.5 cm off centre, and the location of the flame arrestor (red arrow). Based on some rough measurements of the inlet air receiver of a single cylinder, the following can be stated: the inlet air receiver has a diameter of ±9 cm, and the injection nozzle is approx. 10 cm away from the end of the receiver. However, in case the flame arrestor is installed inside the air receiver, the vertical distance reduces to approx. 7 cm. This means that a reduced distance of approx. 7 cm is available for the evaporation of the entire methanol spray from the nozzle, without the interference of any appendages.

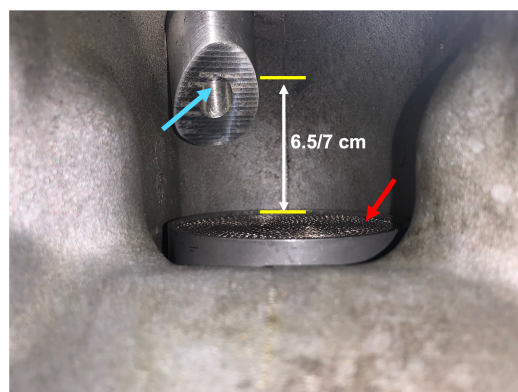Figure 2.1: Airflow through inlet air receiver

Figure 2.2: Arrangement of nozzle inside inlet air receiver

2.2. Theory on the injection and evaporation of methanol

This chapter will describe the theoretical framework behind the injection and evaporation of liquid fuels. First, it will cover the theory on spray characteristics; looking at the spray structure and atomisation of the spray itself, the drop size distribution of the spray, and spray evaporation. Next, the injection spray characteristic and evaporation of methanol using port-fuel injection will be covered.

2.3. Predictions on injection and evaporation behaviour

The next two chapters describe the predictions on injection and evaporation behaviour by covering the modelling methods for the injection model and single-droplet evaporation model.

The creation of a low-pressure injection model is necessary to verify the hypotheses of this research. The modelling methodology of the low-pressure injection model is based on the analytic modelling of three parts, i.e. electric, mechanical and hydraulic. This resulted in an one-dimensional simulation model, based on a mathematical description of a simplified solenoid valve and a mass-spring-damper system. Calculations were performed in the MATLAB/Simulink environment, creating voltage pulses, acting forces and plunger displacement.

Droplet evaporation is of great importance in case of port-fuel injection applications, as it requires a fine enough spray to ensure that a significant portion of fuel would evaporate and follow the airstream into the cylinder. For this reason, a single-droplet evaporation model was created to answer the sub-questions related to the evaporation of methanol. This chapter will explore the development of an one-dimensional mathematical model for the evaporation of a pure liquid droplet suspended in its own vapour. In an attempt to account for all relevant transport mechanisms, a "first principles" approach was used in the development of the model from fundamental conservation equations.

2.4. Experimental Research

The final stage, or chapter, consists of experimental research to perform measurements and verification and/or validation of the single-droplet evaporation model. Measurements will be performed using a custom built experimental setup to test various low-pressure injection nozzles at atmospheric pressure and temperature, as well as measure their individual spray characteristics and droplet size in those conditions. This droplet size is of meaningful importance, as it has a significant effect on the evaporation time of a single droplet. For the measurements of the spray characteristics and droplet size, the shadowgraph measuring technique will be used. The shadowgraph measuring technique is an optical method that visualises non-uniformities in a transparent media, such as air. It is the simplest form of an optical system, suitable for observing a flow exhibiting variations of the fluid density. In principle, shadowgraphy only needs a light source and a recording plane (camera) onto which to project the shadow of the varying density field [15]. After doing the shadowgraphy measurements, an extensive post-processing is performed to determine the spray characteristics and droplet size of specific injection nozzle.

Subsequently to the measurements and post-processing, the verification and/or validation of the single-droplet evaporation model will be performed using this post-processed data. It is expected that both the initial droplet size and evaporation time of the spray from the experimental setup will be determined from the post-processed data. These two parameters will than be used to verify and/or validate if the single-droplet evaporation model generates a similar evaporation timing at an equal initial droplet size as visualised during the experimental setup. If no evaporation of the spray is detected, the post-processed data will be used to determine the initial droplet size, droplet speed, and overall spray pattern generated by the injection nozzle. This is still qualified as valuable information, as such data was not yet available and gives an overall inside into the injection process of the Bosch EV14 injector.

Finally, the last two chapters will cover the discussion, and conclusion & recommendations of this thesis. A discussion will be started regarding the translation to the engine itself. More specifically, how could we couple the results and observations from the research and experimental setup to the Caterpillar G3508A test-engine itself, and how could these conclusions improve upon future work. Consequently, the conclusion & recommendations chapter will give an answer to the main research question, which supports the primary research goal of this thesis.

3

Injection and Evaporation of methanol

This chapter will first describe the theoretical framework behind the port-fuel injection and evaporation of liquid fuels. It covers the spray structure and atomisation of the spray itself, the drop size distribution of the spray, and spray evaporation. Finally, the injection spray characteristic and evaporation of methanol using port-fuel injection will be specifically covered.

3.1. Types of injection

There exist several methods to inject methanol as fuel alternative in internal combustion engines. This section will cover the different injection methods, and the injection and evaporation of methanol. Because of the chemical properties of methanol, it is unable to ignite inside a standard compression ignition engine. This is caused by the low cetane number and high auto-ignition temperature. Two different methods can be used to ignite the air-fuel mixture. Ignition using a spark, or by means of a pilot fuel. Moreover, methanol could be directly injected into the cylinder, or injected via the air injection port, viz. port-fuel injection. This results in the following options for the injection and ignition of methanol in an internal combustion engine:

- Direct injection of methanol-diesel emulsifier blend
- Direct injection of methanol and separate pilot fuel injection
- Port-fuel injection and spark-ignition of methanol
- Port-fuel injection of methanol and pilot fuel ignition
- Combination of port-fuel injection and direct injection

3.1.1. Direct injection

It is possible to directly inject methanol into the cylinder. In this case pilot fuel is required to ignite the methanol. The pilot fuel could be directly injected with the methanol as a blend, or separately. The latter injection method offers some additional potential to optimise the combustion process inside the cylinder.

Direct injection of methanol-diesel emulsifier blend

In this method, a mixture of methanol and pilot fuel is injected directly into the cylinder, as shown in Figure 3.1. The injection process is that of a classical compression ignition engine. Ignition is started by the auto-ignition of the pilot fuel, after which the methanol/air mixture follows. At injection, the methanol-diesel blend will vaporise. This will cause a cooling effect in the cylinder. Methanol has a higher heat of vaporisation compared to diesel, thus achieving a better in-cylinder cooling effect. This cooling effect will reduce the maximum in-cylinder temperature, reducing NO_x emissions and the chance of engine knocking [11]. Performed experiments by Tol [14] gave varying emission results for each run. In general, the following statement can be made: a reduction in CO and HC is associated with an increase in NO_x emissions, whereas reduction in NO_x is associated with an increase in CO and HC emissions [16]. Direct injection of an emulsifier blend is the cheapest way to realise injection and ignition of methanol for existing compression ignition engines. This application requires the least amount of hardware changes to the fuel injection system, meaning that the normal injectors and fuel pipes could be used. However, the use of methanol-diesel emulsifier blends may lead to a reduction in engine power and earlier breakdown of the fuel pipes. Before injecting the methanol-diesel blend, it

must be made sure that the mixture is stable and homogeneously mixed. Otherwise, problems could appear if a pure methanol injection takes place [14].

One of the problems of using a methanol-diesel blend is the poor miscibility, resulting in an emulsion. An emulsion consists of two fluids that will not naturally mix or dissolve. In the case of methanol and diesel, the two fluids will not dissolve as polarity of the fluids are not equal. Polarity of a fluid is the result of a separation on molecular scale of electric charge, leading to the molecules having a negatively charged end and a positively charged end. Methanol is a polar molecule, resulting from the OH-group. When mixing methanol with another polar fluid, the positive and negative ends of the different molecules will attract, enabling the two fluids to dissolve. Diesel consists of carbon atoms connected to hydrogen atoms or other carbon atoms. Both ends of the resulting molecule are equal and consequentially the molecule is apolar. The molecules do not have a dipole moment, and thus will not attract to the polar methanol molecules [7]. In order to overcome phase separation, different additives could be added to the methanol–diesel blend to improve the miscibility. Adding these additives helps the mixture to stay homogeneously stable for a certain time varying from hours to days [14]. Research by Tol [14] and Van de Ketterij [7] showed mixed success rates on keeping a methanol-F76 mixture stable over longer periods of time. A stable mixture was maintained inside an enclosed day tank for longer periods by continuously stirring the mixture. However, extrapolation of these results to a full scale situation on board of a ship were unsatisfying. The daily practices on board a ship are less controlled than those inside a laboratory. This makes it easier for mistakes to happen, which could lead to the complete separation of the methanol-diesel mixture inside the day-tank. As a result, pure methanol could be injected in the engine, which doubtlessly leads to engine failure [7, 14].
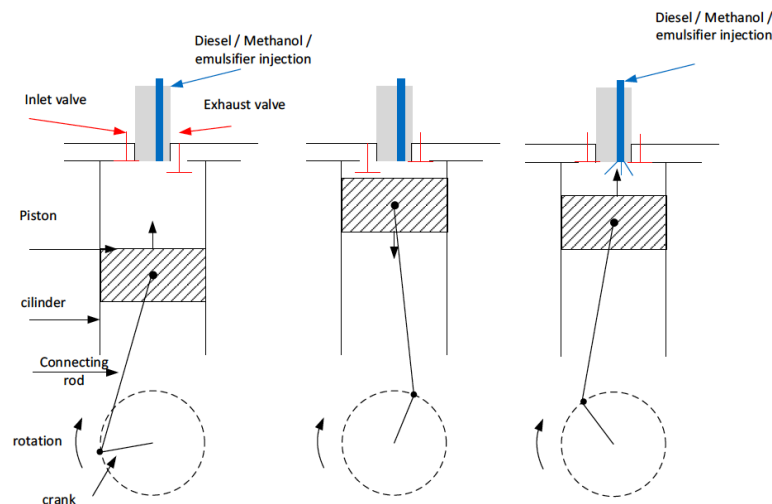
Figure 3.1: Schematic overview of the direct injection of methanol-diesel emulsifier blend [7]

Direct injection of methanol and separate pilot fuel injection
A more advanced injection concept is the separate direct injection of methanol and pilot fuel, as shown in Figure 3.2. This method allows methanol and pilot fuel to be injected separately, enabling the tuning of injection timing. During the first phases of the compression stroke methanol is directly injected in the cylinder, giving the methanol some time to evaporate and mix with the air in the cylinder. Near the end of the compression stroke an explosive air/methanol mixture has formed that needs to be ignited. At that moment a small amount of pilot fuel is injected and ignites, enabling combustion of the methanol/air mixture [7]. However, this ignition method requires a significant reconstruction of existing engines or even a complete redesign. It would be necessary to add additional piping and an extra injection nozzle in the cylinder head. Smaller engines may not have sufficient space in the cylinder head for these two injection nozzle. To conclude, this method therefore seems to require high investment costs for new parts and research into engine capabilities for normally direct injection CI engines [7, 14].
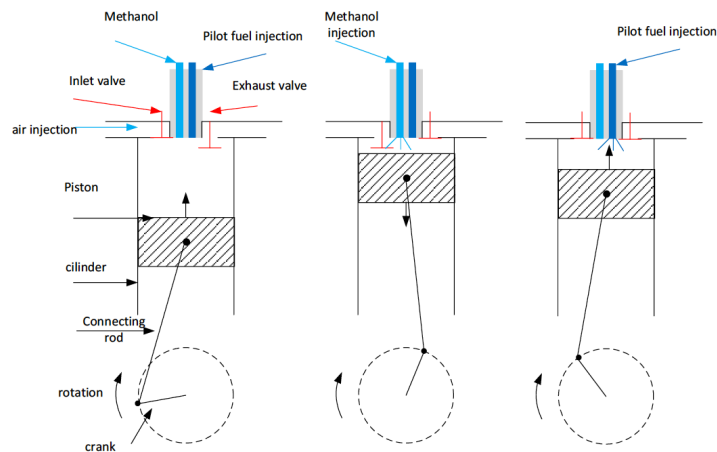
Figure 3.2: Schematic overview of the direct injection of separate methanol and pilot fuel [7]

3.1.2. Port-fuel injection

Methanol has a higher heat of vaporisation compared to diesel fuel. This may negatively influence the in-cylinder combustion process. To overcome this problem, methanol could be injected into the air inlet of the engine, giving the methanol droplets time to evaporate in the air. It has the advantage that the methanol is already in a vapour phase when entering the cylinder. Moreover, the added heat when pressurising the air in the turbocharger could be beneficially used, giving it an additional advantage. The temperature of the scavenging air can be adjusted using an intercooler, thus varying the in-cylinder starting temperature. Cooling the scavenging air has a positive impact on the efficiency of the in-cylinder process and decreases NO_x formation [7].

Port-fuel injection of methanol and pilot fuel ignition

Figure 3.3 shows the schematic overview of the port-fuel injection of methanol and pilot fuel ignition. Methanol is injected into the intake air stream and diesel pilot is injected directly into the cylinder to ignite the methanol-air mixture. It must be noted that this process can be divided into major and minor fraction port-fuel injection, and depends on the ratio methanol and pilot fuel. When more than 50% of methanol is being injected into the scavenge air receiver, it is known as major fraction port-fuel injection. If less than 50% of methanol is injected, it is called minor fraction port-fuel injection. This research thesis looks at direct injection of 100% methanol in a SI engine, thus major fraction port-fuel injection will be used. The port-fuel injection of methanol and pilot fuel ignition requires two separate injectors. A low-pressure injector located in the air inlet and used for injecting the methanol and a high-pressure injector in the cylinder head used for the injection pilot fuel. In addition, a control system is required to control the methanol and pilot fuel injection quantity and timing, etc. A disadvantage of this method is the increase in net weight of the system, due to the additional fuel injection equipment required for the introduction of methanol [11, 16].
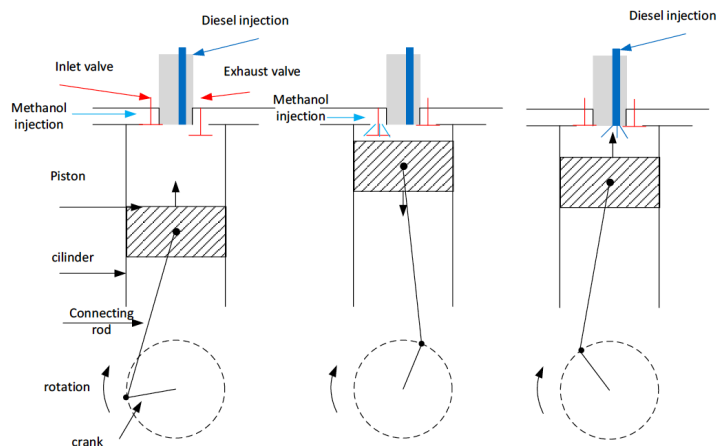

Figure 3.3: Schematic overview of the port-fuel injection of methanol and pilot fuel ignition [7]

Port-fuel injection and spark-ignition of methanol
Port-fuel injection is attractive in spark ignited engines, and often applied on gas engines. These engines use a spark plug to ignite the fuel inside the cylinder. When a sufficient in-cylinder air/fuel ratio is obtained, would the combustion progress in an efficient way after the spark [14]. This type of injection and ignition method was also utilised on the Caterpillar G3508A test-engine, as the low cetane number and high auto-ignition temperature of methanol made the use of port-fuel injection attractive. First, the port-fuel injection and spark-ignition process will be discussed, as shown in Figure 3.4. After the exhaust stroke and closing of the exhaust valve, the inlet valve will open and a (partly evaporated) methanol–air mixture will enter the cylinder. Near the end of the inlet stroke, the inlet valve is closed and the compression stroke starts. This will increase the in-cylinder pressure and temperature, making sure that the remainder of methanol fluid evaporates. Around ±20°BTDC a spark is given and the methanol–air mixture ignites. This results in a steep increase of in-cylinder pressure and temperature, viz. the power stroke. After the power stroke, the exhaust stroke will follow and the process repeats itself [7]. Previous research by Ghent University [17] showed promising results on port-fuel injection with spark-ignition of methanol. They used a converted Volkswagen TDI diesel engine with a 19.5:1 compression ratio. Their research proved that on high loads, spark-timing needed to be retarded due to knocking. A peak Brake Thermal Efficiency (BTE) of 42% was achieved when running on methanol, compared to a BTE of 40% for diesel, and calculated a 20% CO_2 reduction with methanol.
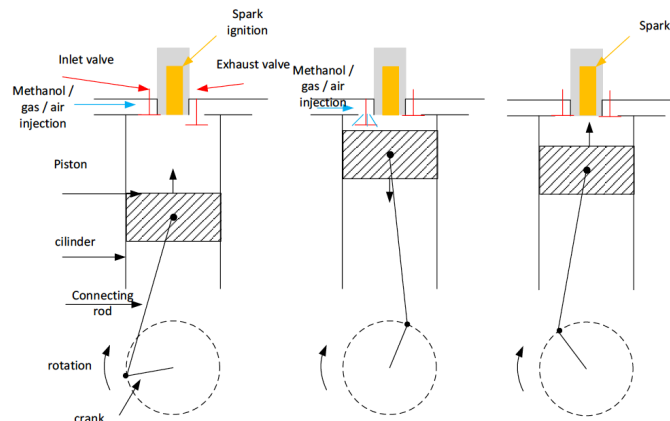
Figure 3.4: Schematic overview of the port-fuel injection of methanol and spark-ignition [7]

3.1.3. Combination of port-fuel injection and direct injection
It is also possible to have a combination of both port-fuel and direct injection, making the engine independent of being spark-ignited or pilot fuel ignited. This could be done to improve the operability and response of the engine; especially in varying load conditions. At base load, the engine operates on the port-fuel injection. Methanol is injected into the air inlet of the engine, giving the methanol droplets time to evaporate in the air. However, in case immediate engine power is required, a small delay would be present from the moment methanol is being injected into the air inlet, and its entry into the cylinder and ignition. To solve this problem, an additional direct injection valve is utilised. This injection valve injects methanol directly into the cylinder to ensure a quick response at increased engine loads. The combination of port-fuel and direct injection safeguards a quick response of the engine load, regardless of its ignition mode.

Table 3.1 gives an overall comparison of the above-mentioned techniques. This table is based on a multitude of experimental findings, as stated by Agarwal et al. [16].

Table 3.1: Emission comparison of various methanol induction techniques [16]

Fuel Induction method		Direct injection of methanol-diesel emulsifier blend	Direct injection of methanol and separate pilot fuel injection	Port-fuel injection of methanol and pilot fuel ignition	Port-fuel injection and spark-ignition of methanol
Effect on performance	*Brake thermal efficiency*	↑	–	↑	↑
	BSFC	↑	↑	↑	–
Effect on emissions	*CO*	↓	↓	↑	↓
	UHC	↓	↓	↑	↓
	NO_x	↑	↑	↓	↓
	Smoke	↓	–	↓	–

3.2. Spray structure

During port-fuel injection, methanol is introduced into the scavenge air receiver by a nozzle with a pressure differential between the fuel supply line and scavenger inlet manifold. As the liquid jet of methanol leaves the nozzle it becomes turbulent and spreads out as it entrains and mixes with the surrounding air. The outer surface of the jet breaks up into droplets. The liquid column leaving the nozzle disintegrates over a finite length into drops of different sizes, called the breakup length. The primary and secondary breakup lengths are defined as the distance between the nozzle tip and the location where the liquid sheet is disintegrated into ligaments and ligaments to droplets, respectively [18]. As the liquid jet moves away from the nozzle, the mass of air within the spray increases. This causes the spray to diverge, increasing its width and decreasing its velocity. The methanol droplets evaporate as the air-entrainment process proceeds. The tip of the methanol spray penetrates further into the air receiver as injection proceeds, but at a decreasing velocity [19].

Figure 3.5 illustrate the essential features of each spray under the simplest configuration, involving multiple sprays injected into quiescent air, until interaction with the wall occurs. Each liquid fuel jet atomises into droplets at the exit from the nozzle orifice (or shortly thereafter). The droplets on the outer edge of the spray evaporate first, creating a fuel vapour-air mixture envelope around the liquid-containing core. The highest velocities are on the jet axis. According to Heywood [19], the equivalence ratio is highest at the centerline (and fuel-rich along most of the jet), which decreases to zero (unmixed air) at the spray boundary. The (fuel-air) equivalence ratio describes the ratio of the actual fuel-air ratio to the stoichiometric ratio. Once the spray has penetrated to the outer region of the scavenge air receiver, it will interact with the walls. The spray is than forced to flow tangentially along the wall. Eventually, spray interaction will occur when multihole nozzles are used.
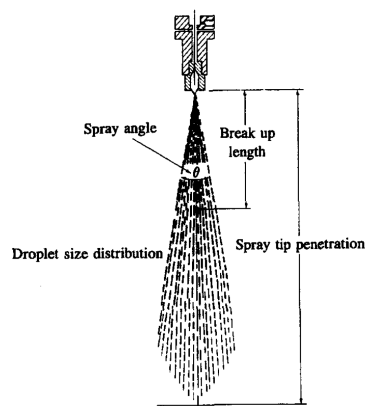
Figure 3.5: Schematic overview of overall spray structure [19]

3.2.1. Atomisation

The fuel jet usually forms a cone-shaped spray at the nozzle exit. This type of behaviour is classified as the atomisation breakup regime, which produces droplets with much smaller sizes than the nozzle exit diameter. This behaviour is different from other modes of liquid jet breakup [19]. At low jet velocity, breakup is caused by the unstable growth of surface waves as a result of surface tension, developing larger droplets than the jet diameter. This phenomenon is known as the Rayleigh regime, where the breakup due to a surface-tension-driven instability results in droplets larger than the nozzle outlet diameter. As jet velocity increases, forces due to the relative motion of the jet and the surrounding air amplify the surface tension force. This leads to droplet sizes of the order of the jet diameter, called the first wind-induced breakup regime. A further increase in jet velocity results in breakup characterised by divergence of the jet spray after an intact or undisturbed length downstream of the nozzle. In the second wind-induced breakup regime, the unstable growth of short-wavelength waves, induced by the relative motion between the liquid and surrounding air, produce droplet diameters that are smaller than the nozzle outlet diameter. Further increases in jet velocity lead to breakup in the atomisation regime, where the droplet sizes are much smaller than the nozzle outlet diameter. The breakup of the outer surface of the jet occurs at, or before, the nozzle exit plane. Aerodynamic interactions at the liquid/gas interface appear to be one major component of the atomisation mechanism in this regime [19].

For jets in the atomisation regime, the spray angle Θ can be found using Eq. 3.1 [20]:

$$\tan\frac{\theta}{2} = \frac{1}{A} \cdot 4\pi \cdot \left(\frac{\rho_g}{\rho_l}\right)^{1/2} \cdot \frac{\sqrt{3}}{6} \tag{3.1}$$

Where, ρ_g and ρ_l are gas and liquid densities, and A is the constant for a given nozzle geometry. An empirical equation for A is shown in Eq. 3.2, where L_n/d_n is the ratio between the nozzle passage length (L_n) and the nozzle exit diameter (d_n). This empirical equation is used to determine the L_n/d_n ratio for sharp-edge inlet nozzles, as currently used on the Caterpillar G3508A test-engine [20].

$$A = 3.0 + 0.28\left(\frac{L_n}{d_n}\right) \tag{3.2}$$

According to Heywood [19], initial jet divergence angles increase with increased gas density. Divergence begins progressively closer to the nozzle as the gas density increases until it reaches the nozzle exit. The nozzle design further affects the onset of the jet atomisation regime. Jet divergence angles decrease with an increase in nozzle length. For the same length, rounded inlet nozzles produce less divergent jets than sharp-edged inlet nozzles. Also, the speed and extent at which the fuel spray penetrates across the scavenge air receiver and into the combustion chamber have an important influence on air utilisation and fuel-air mixing rates.

3.3. Droplet Size Distribution

The spray trajectory is an important feature for the fuel distribution throughout the scavenge air receiver and into the combustion chamber. The atomisation of the liquid fuel into a large number of small droplets is also necessary to create a large surface area across which the liquid fuel can evaporate. The droplet size distribution in the fuel spray depends on injection parameters and the air and fuel properties. Measurements of droplet characteristics in operational engines are extremely difficult, thus most results have come from studies of fuel injection into constant-volume chambers at room temperature [19]. During the injection period, the injection conditions such as injection pressure, nozzle orifice area, and injection rate may vary. Consequently, the droplet size distribution at a given location in the spray may also change with time during the injection period. In addition, since the details of the atomisation process are different in the spray core and at the spray edge, and the trajectories of individual droplets depend on their size, initial velocity, and location within the spray, the droplet size distribution will vary with position within the spray.

The aerodynamic theory of jet breakup in the atomisation regime leads to the prediction that the initial average drop diameter (D_d) is proportional to the length of the most unstable surface waves, as described by Heywood [19]. To characterise the spray, expressions for droplet size distribution and mean diameter are desirable. An appropriate and commonly used mean diameter is the Sauter Mean Diameter (SMD), which characterises a single droplet with the same volume to surface area ratio as the ratio of the respective quantities integrated over the whole droplet size distribution present in a real spray, as shown in Eq. 3.3.

$$SMD = \frac{\left(\int D_d^3 d_n\right)}{\left(\int D_d^2 d_n\right)} = \frac{\sum_{i=1}^{N_{drops}} d_i^3}{\sum_{i=1}^{N_{drops}} d_i^2} \tag{3.3}$$

Where, d_n is the number of droplets with diameter D_d in the range $D_d - dD_d/2 < Dd < D_d + dD_d/2$. The integration is usually carried out by summing over an appropriate number of drop size groups.

3.4. Spray Evaporation

The injected liquid fuel, atomised into small drops near the nozzle exit to form a spray, must evaporate before it can mix with air and burn. Once the start-up phase of the injection process is over, the length of this spray core remains essentially constant until injection ends. This core is surrounded by a much larger vapour-containing spray region that continues to penetrate deeper into the scavenge air receiver. Now, consider a single liquid droplet at close to the ambient temperature. This droplet is being injected into the air conditions present in the scavenge air receiver during the intake stroke. Three phenomena determine the relation of the droplet under these conditions:

1. Deceleration of the droplet due to aerodynamic drag;
2. Heat transfer to the droplet from the air;
3. Mass transfer of vaporised fuel away from the droplet.

As the droplet temperature increases due to heat transfer, the fuel vapour pressure and evaporation rate increases. As the mass transfer rate of vapour away from the droplet increases, because of an increase in the fraction of available heat transferred to the droplet surface, the droplet temperature decreases. As the droplet velocity decreases, the convective heat-transfer coefficient between the air and the droplet decreases. In the spray core (high droplet number density), the evaporation process has a significant effect on the temperature and fuel-vapour concentration in the air within the spray. As fuel vaporises, the local air temperature will decrease and the local fuel vapour pressure will increase. Eventually, a thermodynamic equilibrium would apply, the so-called adiabatic saturation. It must be noted that the liquid fuel vaporisation causes substantial reductions in gas temperature. This equilibrium situation may also not be reached within the spray, the results are still useful for understanding the temperature distribution within an evaporating spray [19].

3.5. Spray characteristics and evaporation of methanol

The atomisation of a liquid fuel is a very important process in engine combustion and emission formation. It is therefore important to understand the effect of methanol properties on the atomisation process. In a direct injection engine, it is expected that the fuel droplets will entirely evaporate before colliding with the cylinder wall. For port-fuel injection engines, methanol spray must be produced fine enough that a significant portion of it would evaporate and follow the airstream directly into the cylinder. In case of liquid impingement of fuel, where the fuel collides with the scavenge air inlet, inlet valve, or cylinder wall, pollutant emissions tend to be higher. It is therefore essential to understand the fuel spray dynamics under realistic engine-like conditions. Detailed studies of evaporating methanol spray characteristics would be vital for adaptation in both DI and PFI engines.

Research by Wang et al. [21] and Zhang et al. [22] were conducted under non-evaporative conditions. Wang et al. [21] studied the spray characteristics of methanol and ethanol with high-pressure swirl injectors at different injection pressures under non-evaporative conditions. They concluded that the spray characteristics of methanol were identical to those of gasoline, although the methanol spray exhibited a slightly higher cone angle than that of gasoline. Zhang et al. [22] studied the effect of ambient gas pressure and injection pressure by investigating the spray characteristics of methanol and dimethyl ether on the swirl nozzle of a Stirling engine. The experimental results showed that the injection and ambient pressure had a significant impact on the spray tip penetration and spray angles. Higher spray pressure made the formation period of spray decrease and the penetration rate increase, whereas higher back pressure inside the injection chamber led to a shrinkage of the spray angle.

Studies by Zeng et al. [23] and Xu et al. [24] researched the flash-boiling phenomenon using methanol. These experiments were conducted by varying the fuel temperature, while the ambient temperature was kept constant at room temperature. The ambient pressure was varied to sub-atmospheric pressures to create flash-boiling conditions. However, these two studies used multihole injectors, which made it difficult to observe a single jet plume due to multiple jet plume interactions. Zeng et al. [23] gave insight into the primary mechanism responsible for the observed spray transformation under flash-boiling conditions. By increasing the fuel temperature or decreasing the ambient pressure, they proved that flash-boiling sprays are able to improve the evaporation of the fuel spray tremendously and increase spray angle for rapid fuel–air mixing. When heated fuel is injected into an ambient environment below its saturation pressure, the fuel can reach a superheated state and experience flash boiling. Xu et al. [24] researched the flash boiling sprays from a multi-hole DI injector by various optical diagnostic techniques. The difference between a non-flash boiling spray and a flash boiling spray is characterised by its nature of two phase flows. Since vapour bubbles are constantly generated inside the liquid phase. This behaviour could introduce prompt spray atomisation and vaporisation, resulting in dramatically different spray characteristics. Xu et al. [24] stated that flash boiling sprays had a much shorter penetration, wider spray angle, more uniformly distributed mass, quicker evaporation, and smaller drop sizes, etc. This makes it ideal for implementation in both port-fuel injection and direct-injection engine. Xu et al. [24] found that the ratio between the ambient pressure and liquid saturation pressure played an important role during the spray flash boiling with good correlations to the spray characteristics.

Research by Lee et al. [25], on the influence of injection pressures up to 300 bar on single liquid jet break-up and atomisation processes, concluded that there is a significant reduction in droplet size and enhanced atomisation for methanol sprays with increased injection pressures. Increasing the injection pressure from 50 to 100 to 200 bar led to a linear decrease in the SMD by approximately 10 µm. However, an injection pressure above 200 bar found no significant reduction in SMD. It must be noted

that such high injection pressures could not be (presently) realised on the Caterpillar G3508A test engine. As this engine uses port-fuel injection, instead of direct injection into the combustion chamber. Moreover, additional research by Ghosh et al. [26] investigated the spray characteristics, i.e. the liquid and vapour penetration of methanol sprays under evaporating conditions. This research used too high injection pressures for implementation on the Caterpillar G3508A test engine; viz. injection pressures of 200 bar, 300 bar, 400 bar, and 480 bar. Results showed, however, that the ambient gas density had a significant effect on both methanol liquid penetration and vapour penetration. The liquid penetration was observed to decrease by 30% when ambient gas density were approximately doubled. The injection pressure had no significant effect on liquid penetration, but had a notable effect on vapour penetration. An increase in ambient gas temperature significantly reduced the methanol liquid penetration, while having only a limited influence on the vapour penetration. A reduction of approximately 13% in liquid length was observed for a rise of ambient gas temperature by 35%.

3.5.1. Injector spray characteristics using methanol port-fuel injection

Dodge et al. [27] research the injector spray characteristics of methanol in reciprocating engines. His approach looked at fine-spray port-fuel injectors producing droplets small enough to follow the airstream past the intake valves and into the engine cylinders. The created spray droplets had to be fine enough, approx. 20 μm in diameter or smaller, to stay suspended in the air and flow into the cylinder. In order to achieve such a fine spray of methanol, air-assist caps were developed and fitted onto standard multi-hole port-fuel injectors. Dodge et al. [27] obtained and spray tested a narrow-beam pintle fuel injector for a Ford Escort 1.9-L engine. It was operated at the design operating pressure of 3 bar and a temperature of 27°C of methanol. This resulted in an average droplet size as represented by the Sauter Mean Diameter (SMD) of 116 μm for the 4-ms pulse width (an idle condition) and 136 μm for the 10-ms pulse width (a higher power condition).

The air-assist cap works as an ejector type of vacuum pump, which produces a low pressure using the Venturi effect. In this case, the working fluid (injected methanol) flows through the nozzle into the cap that narrows in its cross-sectional area. The fluid leaving the nozzle flows at high velocity, which due to Bernoulli's principle results in a low pressure. The air-assist cap then narrows into a mixing section where the high-velocity working fluid (methanol) mixes with the fluid that is drawn in by the low pressure (scavenger air), imparting enough velocity for the mixture to be ejected [28]. These air-assist caps exceeded the goal of producing sprays with SMDs less than 10 pm, and an air pressure differential of 138 kPa_{diff} or less. They used a 1.4-mm exit hole diameter and 100 kPa_{diff} pressure differential from an air-assist injector cap. This produced cross-section average SMDs of approx. 7.5 μm with a fuel-injection pulse width of 4-ms (idle condition), and SMDs of 9 μm with a 10-ms pulse width. The 1.4-mm hole appeared to be the optimum size over the range of pulse width tests.

Most of the spray tests by Dodge et al. [27] were conducted using a variable pressure and temperature test-setup. The test-setup was configured with an air ejector to provide sub-atmospheric pressures, simulating the intake manifold of a spark-ignition automotive engine. Chamber pressures were typically 51 kPa, 76 kPa, and 101 kPa. This type of experimental capability was especially useful when testing the air-assist injector. By adjusting the manifold pressure, the atomising air pressure differential across the injector changes, as well as the air velocity and air density through the exit orifice. All spray measurements were made at an axial distance of 75 mm from the exit of the air-assist injector cap. Increasing the distance, decreased the spray density. This reduced multiple-scattering errors, but increased errors because of evaporation of the spray. Thus, 75 mm was a compromise where multiple-scattering errors were small, but evaporation was limited. The test setup had a laser-diffraction particle sizer and phase-Doppler particle analyser available to conduct the measurements. Only the laser-diffraction instrument was used for these tests, as the phase-Doppler instrument did not perform well on very fine, high-velocity sprays.

Computer modelling of spray evaporation revealed that the droplet evaporation times scale approximately with the square of the droplet diameter. Reducing the droplet size by a factor of ten, reduces the evaporation rates by a factor of 100. Dodge et al. [27] stated that this is true for evaporating methanol sprays until the SMD reaches approx. 10 μm. At or below this size, the evaporation of the spray is so fast that the methanol fuel vapour saturates the air in the cylinder almost instantaneously. Therefore, further reductions in the droplet size below a SMD of approx. 10 μm would not increase evaporation rates. In contrast to the 10 μm limit for the evaporation rate of methanol, reducing the droplet size below 10 μm is effective in increasing the fraction of droplets that would follow the air flow from a port-fuel injector into the cylinder.

Dodge et al. [27] also mentioned some interesting differences between the evaporation-rate controlling mechanisms for the fine sprays for n-heptane and methanol. For n-heptane, fine sprays are limited in the evaporation rate by the mass transfer rate of the fuel from the droplet surface. The difference between the saturation fuel partial pressure at the droplet surface, and the free-stream fuel partial pressure, is the driving force for evaporation at every crank angle. As soon as fuel is injected, it cools the air and is saturated with fuel vapour. There is very little driving force for evaporation between injection and the start of compression. At the start of compression, air temperature rises due to compression heating. This increases the driving force for evaporation. For the methanol fuel, there is again saturation between injection and start of compression. However, beyond the start of compression the difference between the fuel vapour pressure at the surface of the droplet (wet-bulb saturation pressure) and the rest of the in-cylinder gases is much less than for n-heptane; therefore, the driving force for evaporation is much less. The evaporation of the methanol spray is not limited by mass transfer from the droplets, but by the enthalpy (heat energy) available in the cylinder. Methanol has a lower wet-bulb saturation vapour pressure than n-heptane, while the wet-bulb temperature[1] of n-heptane is lower than that of methanol. This is caused by methanol's higher latent heat of vaporisation which cools both the liquid drops and air. Even more significantly, the bulk in-cylinder vapour concentration is much higher for methanol than for n-heptane for two reasons. First, when a given mass of methanol makes the transition from liquid to vapour, more moles of gas are created because of the lighter molecular weight of methanol. Second, because of the lower air/fuel ratio for stoichiometric combustion of methanol a greater mass of methanol fuel must be injected.

3.6. Sub-conclusion

The main objective of this chapter was to describe the theoretical framework behind the injection and evaporation of liquid fuels. Next, the injection spray characteristics and evaporation of methanol using port-fuel injection were covered. By using this theoretical framework, various sub-questions could be answered regarding both the injection and evaporation of methanol.

3.6.1. Injection of methanol

Starting with the injection of methanol, the following sub-question could be answered:

- *How could the injector spray characteristics of methanol be improved by varying the injection pressure, inlet air temperature, spray dimensions, and droplet size?*

Injection, atomisation, and evaporation are important processes in the combustion and emission formation of an internal combustion engine. Previous research showed that the wall-wetting fuel film mass and its evaporation rate directly affect the air-fuel ratio of in-cylinder mixture, as well as the performance of the engine itself. The methanol spray must be fine enough to evaporate and follow the airstream directly into the cylinder.

To summarise, the spray characteristics of methanol can be improved in various ways. Firstly, a higher spray pressure makes the formation period of spray decrease and the penetration rate increase, whereas a higher back-pressure inside the inlet manifold leads to the shrinkage of the spray angle [22]. Secondly, an increase in injection pressure results in a significant reduction in droplet size and enhanced atomisation for methanol sprays [25]. Thirdly, experimental research that varied the fuel temperature, while keeping the ambient temperature constant, showed that the flash-boiling sprays were able to increase the spray angle for rapid fuel–air mixing, and improve the evaporation of the fuel spray tremendously [23]. Moreover, it showed the important role between the ratio of ambient pressure and liquid saturation pressure during the spray flash boiling with good correlations to the spray characteristics [24]. Fourthly, the ambient gas density has a significant effect on both methanol liquid and vapour penetration. Research found that an increase in ambient gas temperature significantly reduces the methanol liquid penetration, however, it has only a limited influence on the vapour penetration [26]. Finally, the droplet size of the injector could be further reduced using a custom air-assist injector cap, as shown by Dodge et al. [27]. Their research used a custom air-assist injector cap to produce cross-section average SMDs of approx. 7.5 µm with fuel-injection pulse widths of 4 ms (idle condition) and SMDs of 9 µm with a 10-ms pulse width, which is a SMD reduction of approx. 93%. These fine-spray droplets were small enough to follow the airstream past the intake valves and into the cylinders.

---

[1]The wet bulb temperature is the lowest temperature to which air can be cooled by the evaporation of a liquid into the air at a constant pressure.

3.6.2. Evaporation of methanol

Next, the following three sub-questions could be (partially) answered on the evaporation of methanol:

- *What is the influence of the inlet air temperature on the evaporation process inside the scavenger air inlet?*
- *What is the influence of fine-spray port-fuel injectors on the evaporation process inside the scavenger air inlet?*
- *How can the evaporation process of methanol inside scavenger air inlet be improved?*

As previously stated, research by Zeng et al. [23] gave insight into the primary mechanism responsible for the observed spray transformation under flash-boiling conditions. By increasing the fuel temperature or decreasing the ambient pressure, their research showed that flash-boiling sprays were able to improve the evaporation of the fuel spray tremendously and increase the spray angle for rapid fuel–air mixing. Moreover, research by Dodge et al. [27] concluded that a custom air-assist injector cap resulted in a significant reduction of cross-section average SMDs. Thus, improving the evaporation process and making the fine-spray droplets small enough to follow the airstream past the intake valves and into the engine cylinders. Their research also described the difference between the evaporation-rate controlling mechanisms for fine sprays for n-heptane and methanol. They state that the fine sprays of n-heptane are limited in evaporation rate by the mass transfer rate of the fuel from the droplet surface, while the evaporation of the methanol spray is not limited by mass transfer from the droplets, but by the enthalpy available in the cylinder. For methanol, the wet-bulb saturation vapour pressure is lower compared to n-heptane. The higher latent heat of vaporisation of methanol cools both the liquid droplets and air, thus having a higher wet-bulb temperature. The bulk in-cylinder vapour concentration of methanol is also much higher because of two reasons. Firstly, more moles of gas are created during the transition from liquid to vapour, since methanol has a lighter molecular weight. Secondly, more methanol must be be injected because of its lower air/fuel ratio for stoichiometric combustion.

To summarise, the evaporation process inside the scavenger air inlet could be improved in various ways. Firstly, increasing the inlet air temperature results in an improved evaporation of the methanol spray. With an increase in inlet air temperature, the droplet temperature increases due to heat transfer resulting in an increase in fuel vapour pressure and evaporation rate, as was stated by Heywood [19]. Note that the evaporation of the methanol spray is not limited by mass transfer from the droplets, but by the enthalpy (heat energy) available in the cylinder [27]. Secondly, using fine-spray port-fuel injectors inside the scavenger air inlet creates spray droplets that are fine enough, approximately 20 μm in diameter or smaller, to stay suspended in the air and flow into the cylinder. In order to achieve such a fine spray of methanol, Dodge et al. [27] developed an air-assist cap and fitted this onto a standard multi-hole port-fuel injector. Thirdly, Dodge et al. found further improvements in the evaporation process of methanol inside the scavenger air inlet. Computer modelling of the spray evaporation revealed that the droplet evaporation times scaled approximately with the square of the droplet diameter. Their research states that this is true for evaporating methanol sprays until the SMD reaches approx. 10 μm. At or below this droplet size, evaporation of the spray is so fast that the methanol fuel vapour saturates the air in the cylinder almost instantaneously. Further reductions in the droplet size would therefore not increase evaporation rates.

3.6.3. Future developments

This section will shortly describe future developments to further improve upon the injector spray characteristic of methanol, as well as improving upon its evaporation process. Firstly, additional research into improving the injector spray characteristics is required to validate if an increase in spray pressure, higher ambient gas temperatures, and ambient gas density indeed results in a reduction of droplet size and enhanced atomisation of methanol sprays. This could be check by means of experimental tests, varying the spray pressure and temperatures. Secondly, it will be necessary to validate the claim by Dodge et al. [27], stating that the droplet size of the injector could be further reduced using a custom air-assist injector cap and thus improve the evaporation of the spray. This could be done by manufacturing a replica of the used air-assist injector cap and checking whether similar results are generated in an experimental setup. Thirdly, additional research is required in validating if an increase in inlet air temperature results in an improved evaporation of the methanol spray. This could be verified by means of experimental tests. The effect of the air temperature on the evaporation could be measured by varying the temperature, while keeping the droplet size the same.

4
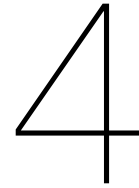
Injection Model

In order to answer the main question of this research, a new low-pressure injection model has to be created. The modelling methodology of this schematic system model is obtained based on the analytic modelling of three parts, i.e. electric, mechanical and hydraulic. These three parts are connected following the principle of Bond graph theory, as described by Thoma [29]. This theory allows the assessment of designs and understanding of cause-effect relationships over entire development phases, even when designs have a rough level of detail before real sample creation [30, 31].

The one-dimensional simulation model is based on a mathematical description of a simplified solenoid valve and mass-spring-damper system. The electrical model describes the generation of an electromagnetic force by a circuit with a coil, in the mechanical model an equilibrium equation of forces acting on the needle resulting in a displacement. In the hydraulic model the injector nozzle is modelled, whereby the needle displacement is transformed into an injection pressure and injection rate over time. The calculations are performed in the MATLAB/Simulink environment, creating voltage pulses, acting forces and plunger displacement.

4.1. Configuration of injector components and functions

Port-fuel injectors have an important additional function to ensure the operation of the internal combustion engine. The mixture-formation components must ensure that the air-fuel mixture is formed properly for a particular system. The main task of a fuel injector is to deliver an exact amount of fuel, at the exact timing, according to the exact engine moment demand, fuel atomisation before the engine intake valve (fuel mixture preparation) and sealing the system when not operated. Another important task of the fuel injector is to form the spray shape, spray angle and fuel droplet size, which influences the formation of air-fuel mixture. Figure 4.1 shows the main components of low pressure fuel injector. A filter strainer is placed in the fuel injector inlet to protect the other components of the injector against any contamination's. The fuel injector is energised through a voltage in pulse format. This generates a magnetic field (B) inside the coil and therefore a magnetic flux (ϕ), which pulls in the armature and lifts the needle of the valve seat. This movement allows fuel to flow through the fuel injector. When the coil is de-energised, the spring and force resulting from the fuel pressure presses the valve needle against the valve seat to seal the fuel-supply system from the intake manifold. The injected volume of fuel per time unit is determined by the system pressure and the available cross section of the spray orifices in the orifices plate. The valve needle closes again when the excitation current is switched off. Figure 4.2 gives a general overview of the working principle of the fuel injector. The electrical ECU signal is an electrical signal in pulse or continuous voltage format. This electrical signal operates the solenoid coil of the injector. The electrical signal has a period and time of injection, both in msec, as shown in Figure 4.3. The time of injection refers to the time that the needle valve should be open for the passage of fuel, also known as the pulse width. In case of a continuous voltage format, the signal mimics the time of injection for a continues length of x msec. While the pulse voltage format gives various injection pulses over the injection time of x msec. However, this pulse voltage format could also be used to mimic various continuous fuel injections over a specific time span.
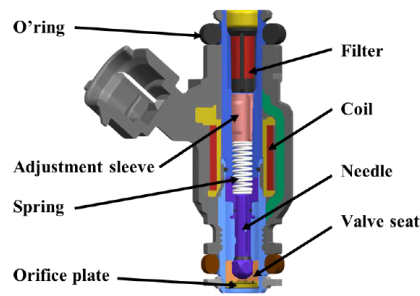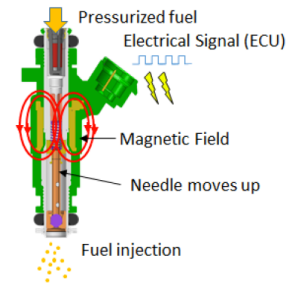
Figure 4.1: Components of fuel injector [31]

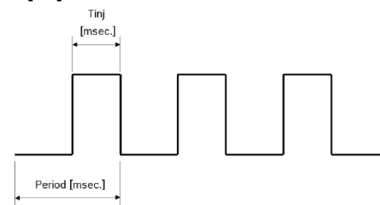Figure 4.2: Working principle of fuel injector [31]

Figure 4.3: Overview of pulse signal [31]

4.2. Modelling Methodology

The development of the one-dimensional simulation model aimed to obtain outputs comparable to real-life measurements of previous studies by Ferreira et al. [31] on the performance of a fuel injector. As starting point, the so-called black box principle was implemented. The fuel injector was sub-divided into three functional sub-groups, i.e. electric (magnetic), mechanic and hydraulic. For each sub-group, all relevant inputs, outputs, and the interaction between groups were identified as illustrated in Figure 4.4. The interaction between the segments can be summarised as a chain effect. Starting at the solenoid controls, a force interaction, and the subsequent lifting of the needle valve.
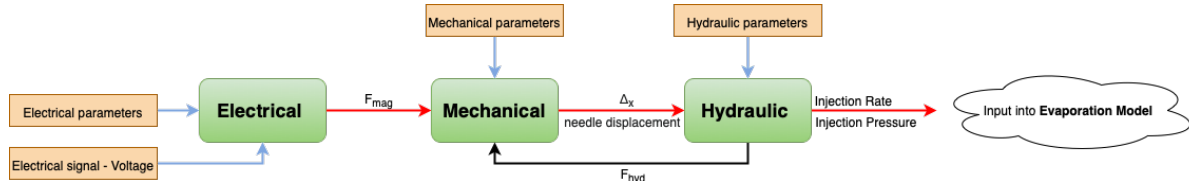

Figure 4.4: General overview of function groups

In order to verify the used modelling methodology, working process, and results of the developed simulation model, contact was made with Ferreira et al. [31]. This meeting resulted in some interesting developments and a recommendation for future work. It showed that the injectors currently installed on the Caterpillar G3508A test-engine are of the wrong sort. At this moment, natural gas injectors are used for the injection of methanol in the scavenge air receiver, instead of the correct EV14 injectors used for the injection of n-heptane fuels. The differences in design of the needle, valve seat, and injector top are both shown in Figure 4.5 and Figure 4.6. It visualises that the NGI injector has grooves in the tip (yellow portion), while EV14 injectors have holes in the plate. It is expected that this would result in overall smaller droplets. Moreover, this made it necessary to review and adjust the injection model itself. But also gives the recommendation to install new injectors of the correct EV14-family for future operations with the engine.
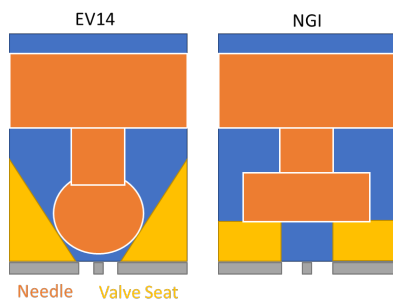

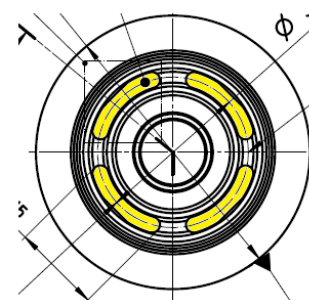Figure 4.5: Comparison between EV14 and NGI injector

Figure 4.6: Arrangement of nozzle inside inlet air receiver

4.2.1. Simplified Solenoid Model

The electric actuation block consists of a solenoid and magnetic force block. These two blocks are responsible of calculating the magnetic force and controlling the injection timing of the injector. The needle displacement is initiated by the magnetic force output of magnetic force block. The simplified solenoid model is based on the resistor–inductor circuit (RL circuit). This is an electric circuit composed of a resistor and inductor driven by a voltage or current source, as shown in Figure 4.7. In a resistor–inductor circuit, the current will not immediately rise to its maximum value when a voltage is applied, due to the presence of inductance. This results in a response delay, as is present in real solenoids. The differential equation corresponding to the transitory regime immediately after closing the resistor–inductor circuit is given by Eq. 4.1 [32]:

$$E - Ri - L\frac{di}{dt} = 0 \rightarrow Ri + L\frac{di}{dt} = E \tag{4.1}$$

The current expression through the resistor–inductor circuit after closing is the solution of the differential equation of the circuit Eq. 4.1, shown by Eq. 4.2 [32].

$$i(t) = \frac{E}{R} \cdot \left(1 - e^{\left(-\frac{R}{L} \cdot t\right)}\right) \tag{4.2}$$

The voltage expression on the coil after connection is given by Eq. 4.3:

$$u(t) = L\frac{di}{dt} = E \cdot e^{\left(-\frac{R}{L} \cdot t\right)} \tag{4.3}$$
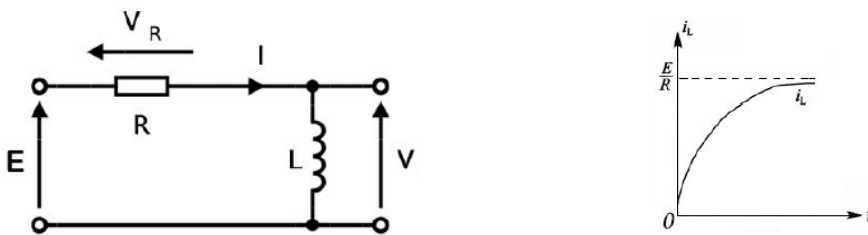
Figure 4.7: General overview of resistor–inductor circuit [13]

The MATLAB/Simulink model of the resistor–inductor circuit after closing was based on Eq. 4.1, where the derivative of the current was separated [32].

$$\frac{di}{dt} = \frac{1}{L}(E - Ri) \tag{4.4}$$

Figure 4.8 and 4.9 show the simplified solenoid block constructed in MATLAB/Simulink for both the continuous and pulse commanding voltage. In these models, the commanding (supply) voltage of 14 volt results in the current (i) and its derivative ($\frac{di}{dt}$). These two parameters are than used to calculate magnetic force to lift the needle valve.
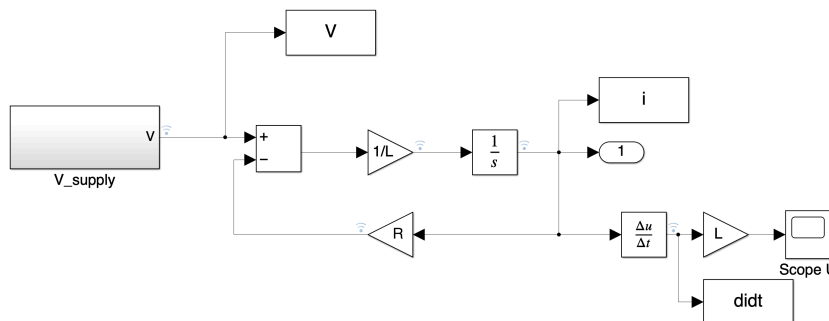
Figure 4.8: Simplified solenoid block - Continuous voltage
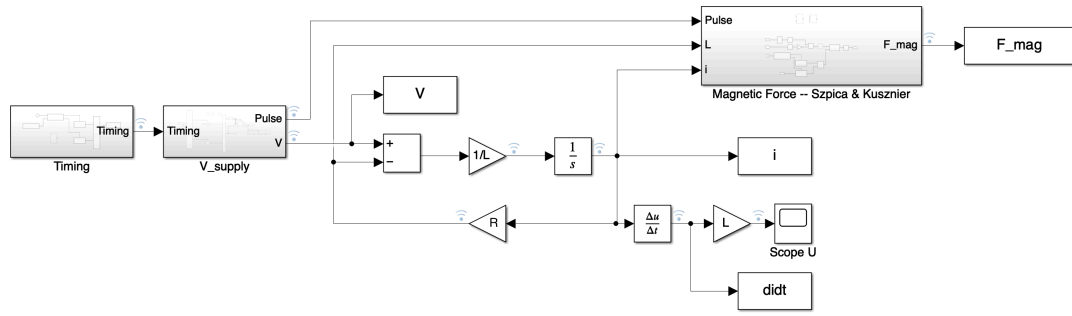
Figure 4.9: Simplified solenoid block - Pulse voltage

4.2.2. Valve Model

The mechanical valve block was modelled according to the principle of the mass–spring–damper system. The mathematical description of this mass–spring–damper function is shown in Eq. 4.5 and Figure 4.10.

$$F_{mag} = F_m + F_p + F_s + F_d \rightarrow F_m = F_{mag} - F_p - F_s - F_d \qquad (4.5)$$
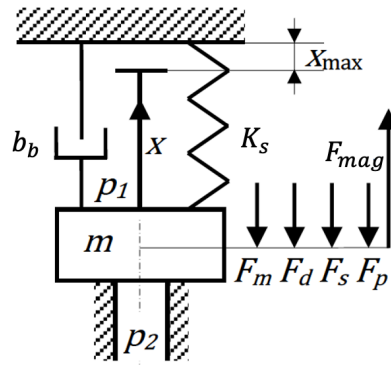
Figure 4.10: Mathematical description of mass–spring–damper system [30]

This equation of equilibrium (Eq. 4.5) is based on five forces. F_m is the resistance force or mass inertia ($m\ddot{x}$), F_d is the damping force of the needle, F_s is the spring force, F_p is the pressure/hydraulic force, and F_{mag} the electromagnetic force of the solenoid.

These forces are calculated as follows:

• The pressure or hydraulic force is calculated using Eq. 4.6.

$$F_p = (P_{rail} \cdot A_{in}) - (P_{manifold} \cdot A_{nozzle}) \qquad (4.6)$$

Where, A_{in} is the cross area over the valve, P_{rail} is the rail pressure, A_{nozzle} the cross area under the valve, and $P_{manifold}$ is the inlet manifold pressure.

• The spring force is calculated using Eq. 4.7.

$$F_s = K_{initial} + k \cdot x \qquad (4.7)$$

Where, $K_{initial}$ is the initial tension of the spring, k is the spring stiffness, and x the displacement of the needle valve.

• The damping force is calculated using Eq. 4.8.

$$F_d = b \cdot \ddot{x} \qquad (4.8)$$

Where, b is the damper rating of the needle valve [N/(m/s)], and $\ddot{x}$ is the velocity of the needle valve.

- The electromagnetic force is calculated using the following equation described by Szpica et al. [30]. The electromagnetic force being the result of the circuit operation can be obtained from the relation shown in Eq. 4.9:

$$F_{mag} = \frac{1}{2}I^2\frac{dL(x)}{dx}$$

(4.9)

Where, I is the current and L is inductance.

- By using Faraday's and Kirchhoff's laws, one may obtain a differential equation describing the change of the current supplying the electromagnetic circuit, as shown in Eq. 4.10

$$\frac{dI}{dt} = \frac{1}{L(x)}\left(U - RI - \frac{dL(x)}{dx}\frac{dx}{dt}I\right)$$

(4.10)

Where, R is the resistance and U is the voltage.

Consequently, substituting Eq. 4.6-4.9 into the second-order differential equation of Eq. 4.5, which governs the dynamics of the needle valve, results in Eq. 4.11 shown below.

$$m \cdot \ddot{x} = \left[\frac{1}{2}I^2\frac{dL(x)}{dx}\right] - \left[b \cdot \ddot{x}\right] - \left[K_{initial} + k \cdot x\right] - \left[(P_{rail} \cdot A_{in}) - (P_{manifold} \cdot A_{nozzle})\right]$$

(4.11)

Where, m is the mass of the needle valve; $\ddot{x}$, $\dot{x}$, and x the acceleration, velocity, and displacement of the needle valve respectively.

Figure 4.11 shows the created MATLAB/Simulink valve model using the implemented second-order differential equation that governs the dynamics of the needle. Inputs into the model are the rail and manifold pressure, geometric coefficients of the needle valve, the initial tension of the spring, and the (previously) calculated electromagnetic force; outputs of the model are the needle velocity and needle displacement. This valve model differs from a typical mass-spring-damping model, since the needle is constrained in its displacement. Hence, the resultant force will not always cause acceleration of the needle.
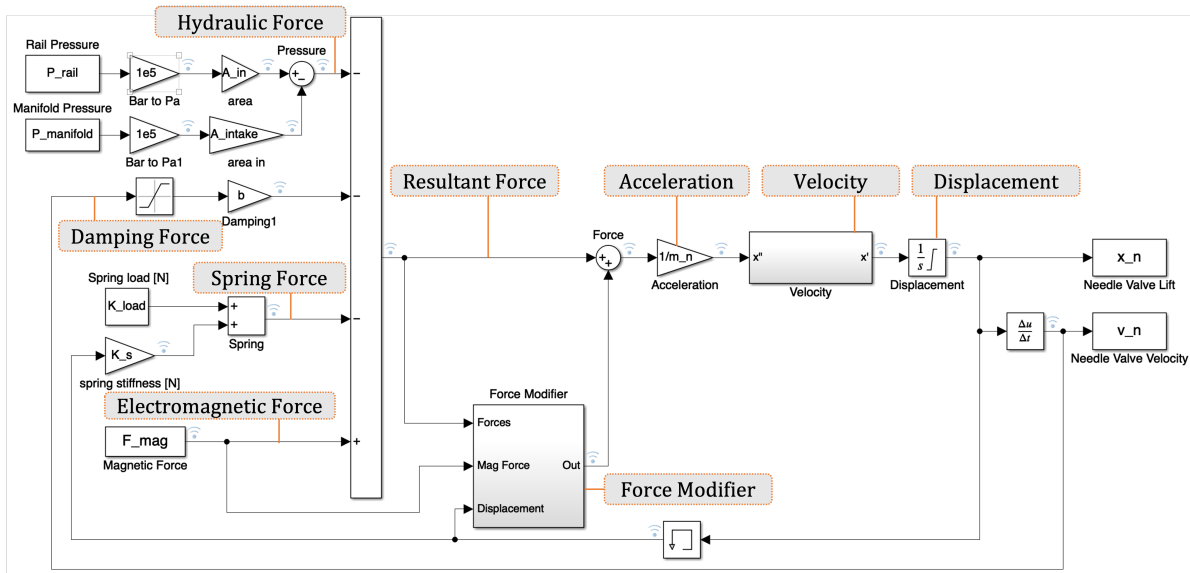
Figure 4.11: Overview of MATLAB/Simulink valve model

Table 4.1 gives the status of the needle valve, as previously described by Zeng [13]. This overview visualises when a force will cause an acceleration of the needle. Yes corresponds to a force that will cause an acceleration, while No means the force will not cause an acceleration of the needle. As shown, only two circumstances result in no acceleration when a force is applied. This is when the needle valve is at its top end, and the resultant force is acting upwards. Or, when the needle valve is at the bottom end, and the resultant force is acting downward. Under both circumstances the needle valve has no displacement change, thus zero velocity and acceleration. Moreover, if the acceleration,

velocity and the displacement of the needle valve are to be directly calculated. The operating results would not be wrapped to zero under these two circumstances. Therefore, additional modifications to the force had to be performed in order to constrain the acceleration, velocity and the displacement output.

Table 4.1: Status of needle valve [13]

Position Force	Top End	Bottom End	In-between
Downwards	Yes	No	Yes
Upwards	No	Yes	Yes

Force Modifier

After the resultant force from the second-order differential equation is calculated, it is sent to the Force Modifier block. This block acts as a filter, to identify under which circumstances the resultant force needs to be modified by a series of logic judgements. The Force Modifier block is shown in Figure 4.12 and works as follows. In case the final output of the Force Modifier block is "0", the resultant force obtained from the second-order differential equation is unaffected. However, when the final output is "-1", the resultant force will be modified to zero. The conditions at which the resultant force will be wrapped to zero are:

- At the top end of the needle valve stroke, and when the solenoid is energised;
- At the bottom end of the needle valve stroke, and the solenoid is not energised;
- At the bottom end of the needle valve stroke, the solenoid is energised but the force is acting downwards.

The latter condition happens when the energising process of the solenoid is initiated. During this short period the gradually increasing magnetic force is smaller than the resistance force. Thus, the resultant force acts downwards, even though the solenoid has been energised. For this reason, the resultant force of the second-order differential equation has to be modified, because at this stage the needle valve has no acceleration.
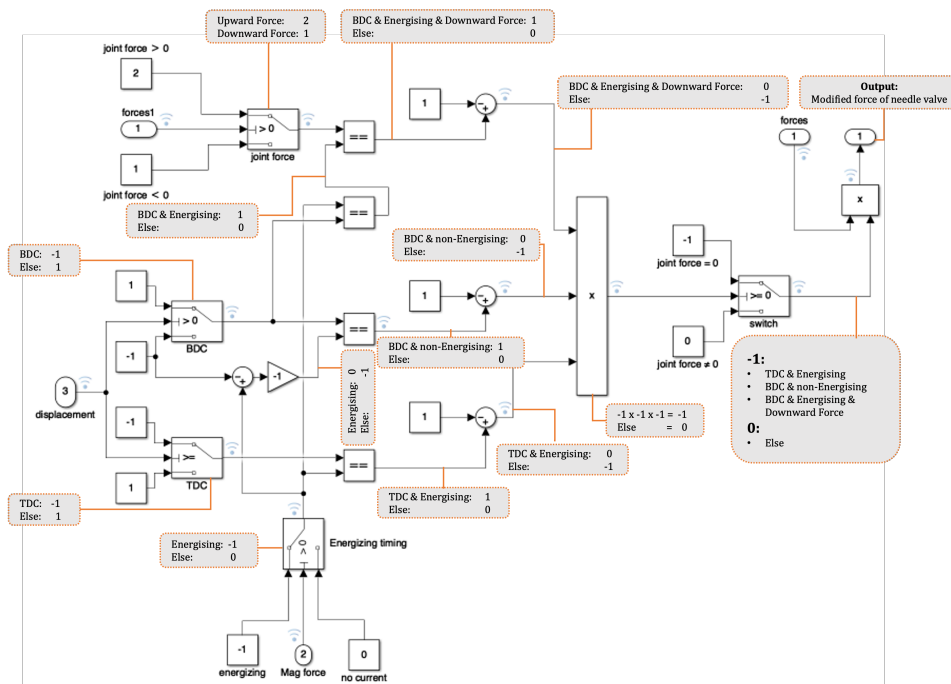
Figure 4.12: Overview of Force Modifier block

Acceleration and Velocity

The acceleration of the needle valve is calculated by dividing the resultant force ($F_{resultant}$) by the needle mass (m_{needle}), as shown in Eq 4.12.

$$a = \ddot{x} = \frac{F_{resultant}}{m_{needle}} \tag{4.12}$$

After the resultant force is modified and the acceleration determined, it would also be essential to modify the velocity of the needle valve. This modification is necessary because a simple integration calculation will keep the velocity at a constant value instead of wrapping to zero when the needle valve is not moving. This modification is done by means of a conditional judgement block as shown in Figure 4.13.
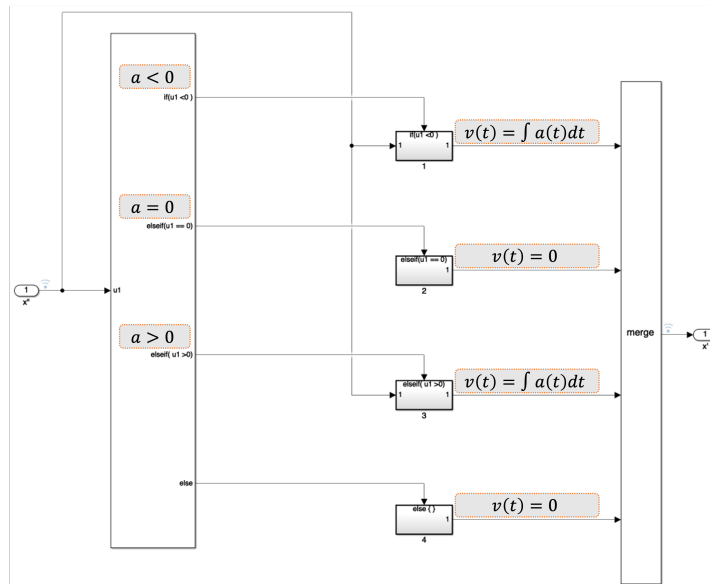
Figure 4.13: Overview of Velocity block

Displacement

Finally, the displacement of the needle valve is determined by means of a simple integration calculation. In order to realise the correct needle displacement, constraints are set on the saturation limits of the integration block. These constraints simulate the total displacement stroke the needle valve has in real-life.

4.2.3. Injector Nozzle Model

The final sub-model is used to determine the injection rate and injection pressure over time; based on the needle displacement, manifold pressure, and pressure drop over time as its input. The model configuration of the injection nozzle is shown in Figure 4.14. In this model is the volumetric flow rate of the methanol calculated using Eq. 4.13:

$$Q_{inj} = \xi_n \cdot C_{d_{needle}} \cdot A_{nozzle} \cdot \sqrt{\frac{2}{\rho} \left| P_{drop} - P_{manifold} \right|} \tag{4.13}$$

Where, ξ_n is a binary number representing the opening of the nozzle determined by the needle lift; $C_{d_{needle}}$ is the discharge coefficient of the outlet orifice; A_{nozzle} is the area of the outlet orifice of the injector; and P_{drop} and $P_{manifold}$ are the pressure drop and manifold pressure outside the injector respectively.

The pressure of the injection nozzle is calculated according Eq. 4.14, as described by Chung and Zeng respectively [13, 33]. In case there is no injection, the pressure inside the injector is equal to the rail pressure of the fuel pump. During injection, as fuel leaves the injector, the injection pressure decreases.

$$P_{inj} = \frac{K_f}{V} \cdot Q_{inj} \tag{4.14}$$

Where, K_f is the bulk modulus of methanol, V is the injection volume, and Q_{inj} is the flow rate of the fuel through the nozzle holes, also referred to as the injection rate. The bulk modulus [N/m^2] is a numerical constant that describes the elastic properties of a solid or fluid when it is under pressure on all surfaces. An applied pressure reduces the volume of the medium, which returns to its original volume when the pressure is removed. The bulk modulus is sometimes referred to as the incompressibility, because it is a measure of the ability of a substance to withstand changes in volume when under compression on all sides.
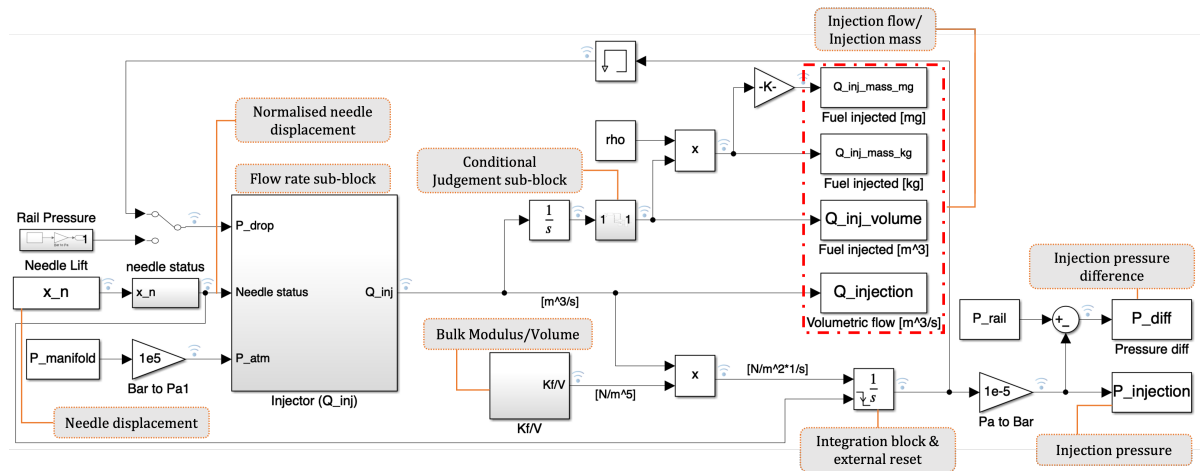

Figure 4.14: Overview of MATLAB/Simulink injection nozzle model

4.3. Simulation and Results

This section will address the simulation results of the low-pressure injection model covered above. As previously stated, two different strategies have been applied; a continuous and pulse injection strategy have been simulated in the low-pressure injection model by varying the commanding voltage. As the name states, the continuous injection strategy reflects a continuous injection of fuel over a fixed time-span. This mimics the time of injection for a continues length of x msec. The pulse injection strategy gives the option to variate the fuel injection timing of x msec in-between pulses, or to have multiple injections of fuel during the inlet stroke of the engine.

Both the continuous and pulse injection strategy operate on the same principle. It could therefore be stated that the continuous injection strategy is a zoomed-in part of the pulse injection strategy. Because of this, only the simulation and results of the pulse injection strategy will be shown in this section.

The low-pressure injection model starts with a commanding voltage that actuates the injector. The commanding voltage is sent to the solenoid model, which generates a current. The current in the solenoid exerts a corresponding electromagnetic force which actuates the needle valve. Figure 4.15 gives an overview of the commanding voltage, current and electromagnetic force. This depicts a responds delay of current, due to the inductance of the coil. The electromagnetic force is modelled as proportional to the generated current.
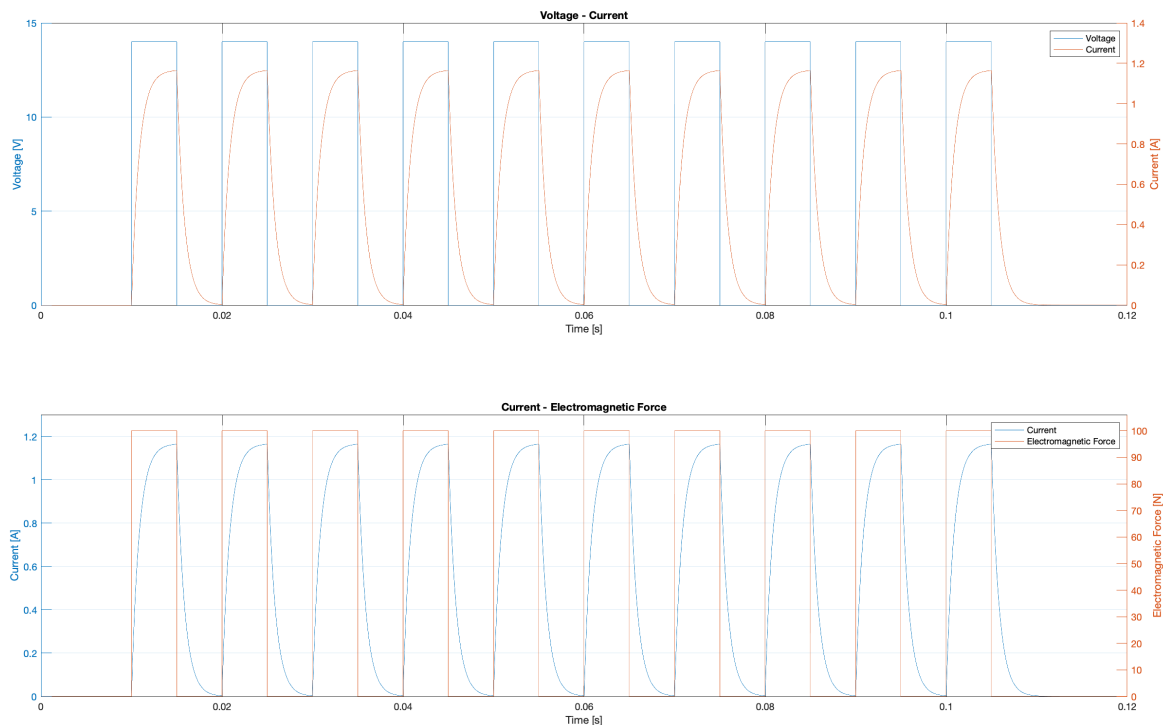
Figure 4.15: Overview of commanding voltage, current, and electromagnetic force response

The resultant force; which is the summation of the electromagnetic force, hydraulic pressure force, damping force, and spring force, controls the displacement of the needle valve. Figure 4.16 shows the response between the resultant force and needle displacement during the pulse injection strategy. Clearly visualising that each commanding voltage pulse results in an equally long opening of the needle valve. The maximum needle displacement was set at 100 μm, as described by Ferreira [31]. The lifting of the needle valve lets fuel flow through the injection holes, and thus initiates the injection. The start and ending of the injection process is strictly described by the lifting of this needle valve, and results in both a fuel injection rate and injection pressure. Figure 4.17 depicts the needle valve displacement and corresponding injected mass per pulse, given in mg. It visualises that for every injection pulse, lasting 5 ms, approximately 22.5 mg (33 cm^3) of fuel is being injected. This totals to approximately 223 mg (330 cm^3) over an entire injection time of 100 ms. Moreover, the linear shape of the injection rate does not have the same gradient over the entire pulse. When zooming in, it becomes apparent that there is a decrease in gradient at the end of each injection pulse, approx. 0.1 ms long. This is most likely caused by the damping effect of the needle valve when returning to its valve seat.
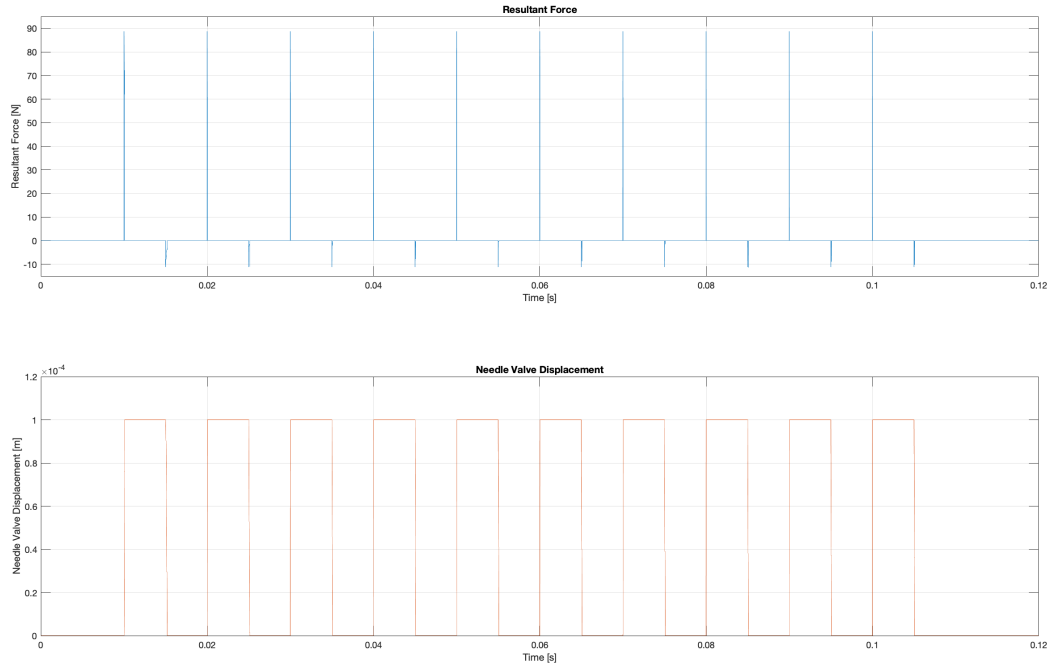
Figure 4.16: Overview of resultant force and needle valve displacement

Figure 4.18 shows the needle valve displacement and corresponding injection pressure. It shows that during each injection pulse, the injection pressure decreases with approximately 0.12 bar per pulse, compared to the initial rail pressure of 5 bar. However, due to the short injection pulses of 5 ms, the injection pressure is almost instantaneously restored to the initial rail pressure when the needle valve is returning to its valve seat.
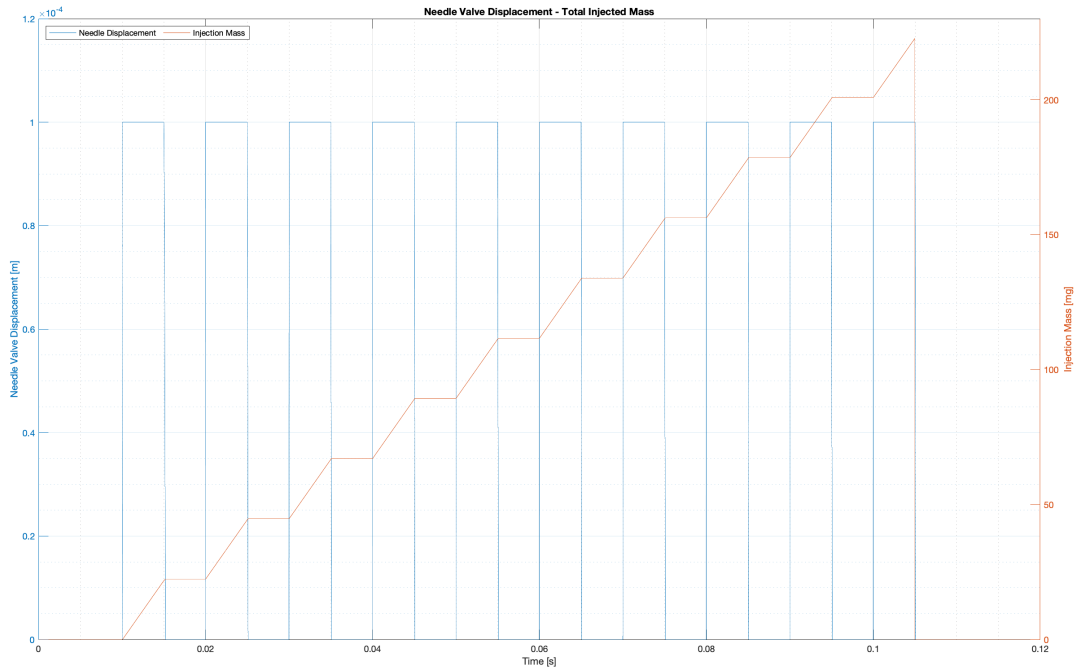

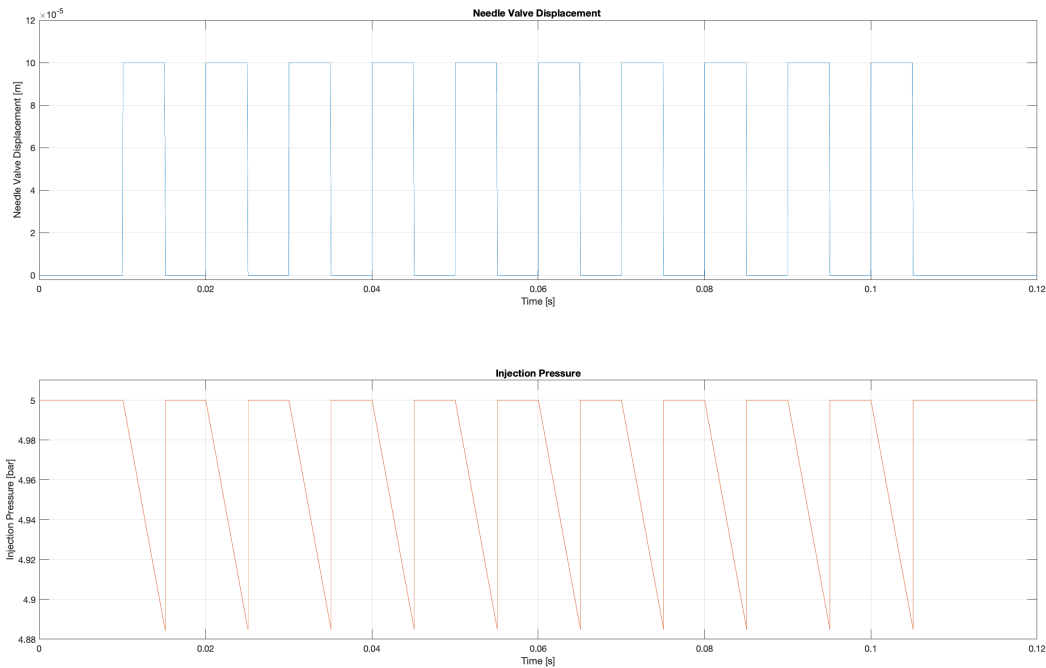Figure 4.17: Overview of needle valve displacement and total injected mass

Figure 4.18: Overview of needle valve displacement and injection pressure per pulse

4.4. Sub-conclusion

The main objective of this chapter was to develop and reproduce a dynamic low-pressure injection model that represents the injection of 100% methanol into the Caterpillar G3508A test engine. In addition, it would answer the following sub-question:

- *How could the port-fuel injector be modelled in such a way that represents the injection of the Caterpillar G3508A test engine?*

To achieve this goal, a literature study was performed to investigate the operating principle and modelling methodology of the low-pressure injection system. This mainly led to literature from the automotive industry, where low-pressure port-fuel injection applications are traditionally common. The development of the low-pressure injection model was focused on reproducing the behaviour of an electrical injector used for port-fuel injection applications. This made two parameters especially important: the flow rate which the model provides, and the droplet distribution which is established experimentally.

The one-dimensional simulation model of a low-pressure injector is based on a mathematical description of a simplified solenoid valve and mass-spring-damper system. The model itself consists of three sub-models; a simplified solenoid model, a valve model, and an injection nozzle model. The simplified solenoid model describes the generation of an electromagnetic force by a circuit with a coil. In the valve model, an equilibrium equation of forces acting on the needle results in a displacement. Lastly, the injection nozzle model describes the injector nozzle. In this model, the needle displacement is transformed into an injection pressure and volumetric flow rate over time. The calculations were performed in the MATLAB/Simulink environment, where the three sub-models were ran sequentially to simulate the process from receiving the electrical commanding voltage to fuel injection into the manifold. The following conclusion could be made on the low-pressure injection model. The proposed mathematical description of the operation of the model allows for the simulation of the injection process, which represents that of the Caterpillar G3508A test engine. The use of experimental results and implementation of these results into an empirical model have been an useful tool in modelling the complex electromagnetic system with a coil and movable core, as was described by Szpica [30]. Lastly, the movement of the needle valve was determined by means of the electromagnetic force, pressure force, damping force, and spring force.

The simulation results of the low-pressure injection model, as shown in Figure 4.19, visualises the needle valve displacement, injection pressure decrease, and volumetric flow rate. It reveals that during each injection pulse, the injection pressure decreases with approximately 0.12 bar per pulse, compared to the initial rail pressure of 5 bar. However, due to the short injection pulses of 5 ms, the injection pressure is almost instantaneously restored to the initial rail pressure when the needle valve

is returning to its valve seat. The volumetric flow rate per pulse is approximately 33 cubic centimetres per pulse. This amounts to approximately 330 cc of fuel over a total injection time of 100 ms. However, the injection volume could be tuned by modifying the area of the needle holes. It can be concluded that the developed mathematical description allowed for the simulation of the injection process to obtain the volumetric flow rate. This volumetric flow rate is an important parameter, as it could be used as input for future spatial evaporation models.
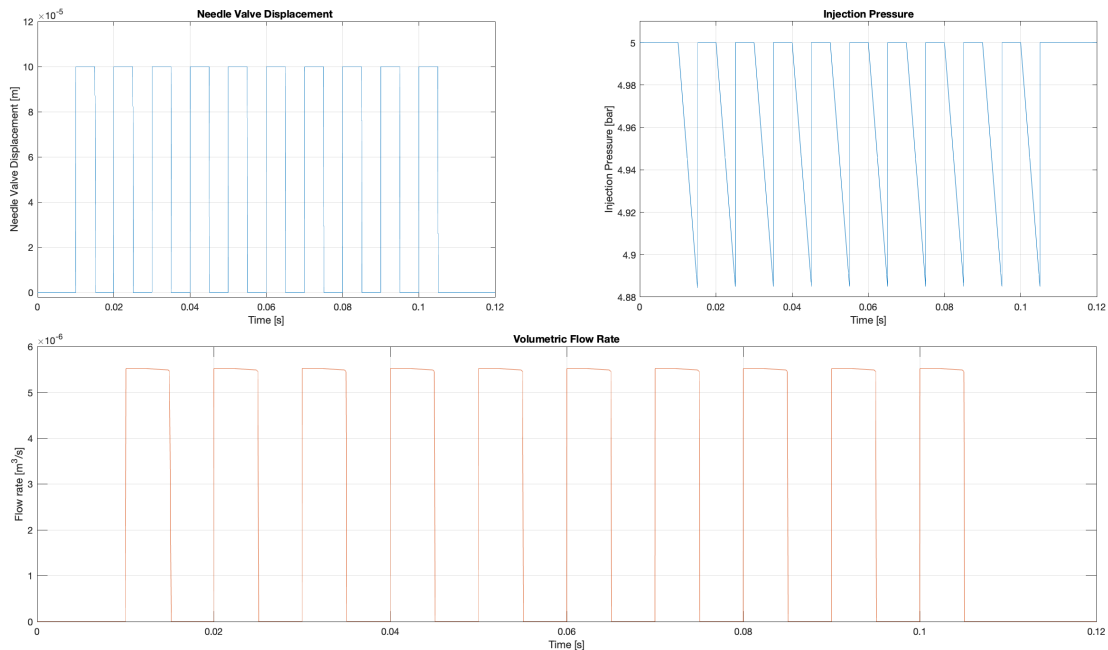

Figure 4.19: Simulation result of low-pressure injection system

4.4.1. Future developments

This section will shortly describe future developments to further improve on the developed low-pressure injection model. An important future development of the injection model is its spray rate characteristic. This parameter could be used as input for CFD analysis of the evaporation and combustion of methanol. Therefore, future research into the spray characteristic is necessary; to obtain a simulated spray rate, spray pattern, and droplet size generated by the nozzle tip. Subsequently, because of the high complexity of the mathematical description, the modelling approach was simplified. Therefore, the following assumptions could be improved upon. The needle movement was not affected by vibrations and other mechanical disturbances. Eddy currents, magnetic saturation and coil temperatures were not included and did therefore not affect the parameters of the electromagnetic circuit. Friction of the needle valve was not included into its movement, future research could implement friction of the needle valve into static, kinetic and viscous friction where its value depends on the needle movement itself. Lastly, due to the complexity of construction, the inductance of the electromagnetic circuit was determined empirically. These assumptions led to some imperfections in the mathematical description and may have influenced the results. For this reason, further mathematical analysis and the necessity to carry out (partial) experimental research would be needed. This (partial) experimental research would be based on the electromagnetic force acting on the needle and frictional resistance. Another improvement to the injection model would be the collision of the needle valve against the valve seat, which is considered fully inelastic in the valve sub-model. It assumes that when the needle valve reaches its boundary/valve seat, the force, velocity, and acceleration are all set to zero. Further research is recommended to use the impulse to simulate the movement of the needle valve, to ensure that the valve does not stop immediately when the collision happens. The low-pressure injection model is capable of simulating all desired injection strategies by varying its commanding voltage setting. As a result, it could be integrated with the in-cylinder combustion model to predict combustion emissions and the heat release rate of the internal combustion engine. However, the low-pressure injection model has not been validated due to lack of available time and resources. Further research is therefore essential to validate the results and improve on the model accuracy. Especially, when the low-pressure injection model becomes integrated as a sub-model into other simulation models.

<div style="text-align: right; font-size: 3em;">5</div>

Evaporation Model

5.1. Introduction

Droplet evaporation is of great importance in case of port-fuel injection applications, as it requires a fine enough spray to ensure that a significant portion of fuel would evaporate and follow the airstream into the cylinder. From a broad perspective, the evaporation process is well understood; however, it is becoming increasingly important to develop detailed and specific models that can simulate how a droplet evolves over time. This droplet evaporation process is no a trivial task as it is affected by a great number of parameters and environmental conditions. Common simplifications include the assumption that the process will be dominant by particular flows, such as in the case of purely diffusive models, or by applying empirical relationships. This chapter will describe the created single-droplet evaporation model used to answer the sub-questions related to the evaporation of methanol. It will explore the development of an one-dimensional mathematical model for the evaporation of a pure liquid droplet suspended in its own vapour. In an attempt to account for all relevant transport mechanisms, a "first principles" approach is taken by developing the model from fundamental conservation equations. Using perturbation analysis, a reduced system of equations was achieved and solved numerically with MATLAB. In this chapter, various responses to varying conditions are demonstrated in several simulations. The main objective is to start with the fundamental conservation principles and, with minimal assumptions, derive an effective droplet evaporation model that can be used to answer the sub-questions related to the evaporation of methanol.

5.2. Model

To investigate the effect of this evaporation process; the model considers a pure liquid droplet, suspended in an atmosphere of its own pure vapour, within a sufficiently large vessel and free from any external forces such as gravity. This assumption provided the basis of the single-droplet evaporation model and is based on a paper by Alroe et al. [34]. Because of the symmetry of a droplet, the physical scenario leads to a two phase one dimensional model, as shown in Figure 5.1.

Figure 5.1: One dimensional domain of the droplet evaporation problem [34]

First, the systems of equations needs to be established in each phase. As previously stated, in an attempt to account for all the relevant transport mechanisms, a "first principles" approach is taken by developing the model from fundamental conservation equations; the principles of conservation of continuity, momentum and energy. These conservation equations have been extensively covered by Bird, Stewart and Lightfoot [35] and will be described below.

Equation of Continuity

The Equation of Continuity is developed by writing a mass balance over a volume element $\Delta x\, \Delta y\, \Delta z$, fixed in space, through which a fluid is flowing. It can be visualised using Eq. 5.1 [35].

$$
\left\{ \begin{array}{c} \text{Rate of} \\ \text{increase} \\ \text{of mass} \end{array} \right\} = \left\{ \begin{array}{c} \text{Rate of} \\ \text{mass} \\ \text{in} \end{array} \right\} - \left\{ \begin{array}{c} \text{Rate of} \\ \text{mass} \\ \text{out} \end{array} \right\} \tag{5.1}
$$

Translating this simple physical statement into mathematical language results in the following equation, as shown in Eq. 5.2.

$$
\frac{\partial \rho}{\partial t} = -\left(\frac{\partial}{\partial x}\rho v_x + \frac{\partial}{\partial y}\rho v_y + \frac{\partial}{\partial z}\rho v_z \right) \tag{5.2}
$$

This shows the equation of continuity, which describes the time rate of change of the fluid density at a fixed point in space. The equation can be written more concisely by using vector notation, as shown in Eq. 5.3.

$$
\frac{\partial \rho}{\partial t} + (\nabla \cdot \bar{V}) = 0 \;\rightarrow\; \frac{\partial \rho}{\partial t} = -(\nabla \cdot \bar{V})
$$

| Rate of increase of mass per unit volume | Net rate of mass addition per unit volume by convection |

$$\tag{5.3}$$

Where, $(\nabla \cdot \rho\bar{V})$ is called the "divergence of $\rho\bar{V}$, also written as "div $\rho\bar{V}$". The vector $\rho\bar{V}$ is the mass flux, and its divergence is the net rate of mass efflux per unit volume.

Note that Eq. 5.2-5.3 are both written in Cartesian coordinates (x, y, z), while for a droplet it is more convenient to use spherical coordinates (r, θ, ϕ). Converting the continuity equation from Cartesian coordinates to spherical coordinates results in Eq. 5.4.

$$
\frac{\partial \rho}{\partial t} + \frac{1}{r^2}\frac{\partial\left(\rho r^2 V_r\right)}{\partial r} + \frac{1}{r\sin(\theta)}\frac{\partial\left(\rho V_\theta \sin(\theta)\right)}{\partial \theta} + \frac{1}{r\sin(\theta)}\frac{\partial\left(\rho V_\varphi\right)}{\partial \varphi} = 0 \tag{5.4}
$$

In some particular flows, Eq. 5.4 could be simplified even further. In case of a purely radial flow, such as that of a point source or sink, the continuity equation becomes:

$$
\frac{\partial \rho}{\partial t} + \frac{1}{r^2}\frac{\partial\left(\rho r^2 V_r\right)}{\partial r} = 0 \longrightarrow \frac{\partial \rho}{\partial t} = -\frac{1}{r^2}\frac{\partial\left(\rho r^2 V_r\right)}{\partial r} \tag{5.5}
$$

Equation of Momentum
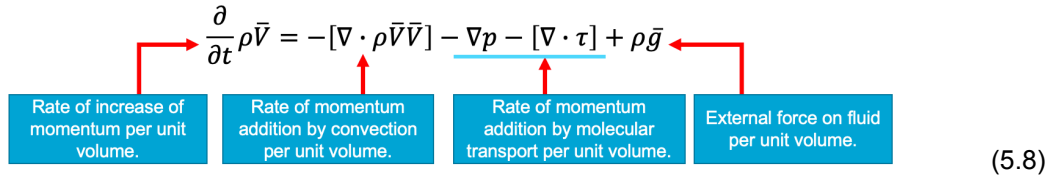
In order to get the Equation of Momentum, a momentum balance is written over the volume elements $\Delta x\, \Delta y\, \Delta z$. This can be visualised using Eq. 5.6 [35].

$$
\left\{ \begin{array}{c} \text{Rate of} \\ \text{increase of} \\ \text{momentum} \end{array} \right\} = \left\{ \begin{array}{c} \text{Rate of} \\ \text{momentum} \\ \text{in} \end{array} \right\} - \left\{ \begin{array}{c} \text{Rate of} \\ \text{momentum} \\ \text{out} \end{array} \right\} + \left\{ \begin{array}{c} \text{External} \\ \text{force on} \\ \text{the fluid} \end{array} \right\} \tag{5.6}
$$

Translating this simple physical statement into mathematical language results in the following equation, as shown in Eq. 5.7.

$$
\frac{\partial}{\partial t}\rho\bar{V} = -[\nabla \cdot \Phi] + \rho\bar{g} \tag{5.7}
$$

It is stated by Bird, Stewart and Lightfoot [35] that the combined momentum flux tensor (Φ) is the sum of the convective momentum flux tensor ($\rho\bar{V}\bar{V}$) and the molecular momentum flux tensor π, and that the latter can be written as the sum of $p\delta$ and τ. Where, τ is the (viscous) momentum flux tensor, δ a unit tensor, and p the fluid pressure. When substituting $\Phi = \rho\bar{V}\bar{V} + p\delta + \tau$ into Eq. 5.7, we obtain following equation of momentum, as shown in Eq. 5.8.

$$\frac{\partial}{\partial t}\rho\bar{V} = -[\nabla \cdot \rho\bar{V}\bar{V}] - \nabla p - [\nabla \cdot \tau] + \rho\bar{g}$$

| Rate of increase of momentum per unit volume. | Rate of momentum addition by convection per unit volume | Rate of momentum addition by molecular transport per unit volume. | External force on fluid per unit volume. |

(5.8)

Where, ∇p is a vector called the "gradient of (the scalar) p", also written as "grad p". The symbol $[\nabla \cdot \tau]$ is a vector called the "divergence of (the tensor) τ", and $[\nabla\rho\bar{V}\bar{V}]$ is a vector called the "divergence of (the dyadic product[1]) $\rho\bar{V}\bar{V}$"

Since the assumption of this model considers that a pure liquid droplet is free from any external forces such as gravity, we can assume $\rho\bar{g} = 0$. This simplifies the Equation of Momentum to:

$$\frac{\partial}{\partial t}\rho\bar{V} = -[\nabla \cdot \rho\bar{V}\bar{V}] - \nabla p - [\nabla \cdot \tau] \longrightarrow \rho\frac{\partial V}{\partial t} = -\nabla \cdot (\rho v^2) - \nabla p - [\nabla \cdot \tau] \quad (5.9)$$

Where, ρ is the density, v is the velocity, p is the pressure, and τ the stress tensor.

Equation of Energy

As stated by Bird, Stewart and Lightfoot [35], the equation of change for energy is obtained by applying the law of conservation of energy to a small element of volume $\Delta x\,\Delta y\,\Delta z$ and then allowing the dimensions of the volume element to become infinitesimally small. The conservation of energy equation can be visualised using Eq. 5.10 [35].

$$\begin{Bmatrix} \text{Rate of} \\ \text{increase of} \\ \text{kinetic and} \\ \text{internal} \\ \text{energy} \end{Bmatrix} = \begin{Bmatrix} \text{Net rate of kinetic} \\ \text{and internal} \\ \text{energy addition} \\ \text{by convective} \\ \text{transport} \end{Bmatrix} + \begin{Bmatrix} \text{Net rate of heat} \\ \text{addition by} \\ \text{molecular} \\ \text{transport} \\ \text{(conduction)} \end{Bmatrix} + \begin{Bmatrix} \text{Rate of work} \\ \text{done on system} \\ \text{by molecular} \\ \text{mechanisms} \\ \text{(i.e., by stresses)} \end{Bmatrix} + \begin{Bmatrix} \text{Rate of work} \\ \text{done on system} \\ \text{by external} \\ \text{forces} \\ \text{(e.g., by gravity)} \end{Bmatrix} \quad (5.10)$$

The most useful form of the energy equation is one in which the temperature appears. This can be used for the prediction of temperature profiles. The following equation of change for internal energy is obtained, when the mechanical energy equation is subtracted from the energy equation, as visualised in Eq. 5.11.

$$\frac{\partial}{\partial t}\rho\hat{U} = -[\nabla \cdot \rho\hat{U}\bar{V}] - [\nabla \cdot \bar{q}] - p(\nabla \cdot \bar{V}) - (\tau : \nabla\bar{V})$$

| Rate of increase in internal energy per unit volume. | Net rate of addition of internal energy by convective transport, per unit volume. | Rate of internal energy addition by heat conduction, per unit volume. | Reversible rate of internal energy increase per unit volume by compression | Irreversible rate of internal energy increase per unit volume by viscous dissipation |

(5.11)

Where, ρ is the density, $\hat{U}$ is the internal energy, $\bar{V}$ is the velocity vector, V is the velocity, $\bar{q}$ is the heat flux vector, p is the pressure, τ is the stress tensor, ∇ is the nabla operator, $\hat{c}_v$ is the volumetric heat capacity, T is the temperature, and $\hat{V}$ is the specific volume.

Equation 5.11 can be put in the substantial derivative form, which describes the change of fluid elements by physical properties such as temperature, density, and velocity components of flowing fluid along its trajectory. This results, with no further assumptions, in Eq. 5.12.

$$\rho\frac{D\hat{U}}{Dt} = -[\nabla \cdot \bar{q}] - p(\nabla \cdot \bar{V}) - (\tau : \nabla\bar{V}) \quad (5.12)$$

Finally, Bird, Stewart and Lightfoot summarised various equations of change for pure fluids in terms of their fluxes. In transport phenomena, fluxes are the vector quantities, which describe the magnitude and direction of the flow of a substance or its property. The Equation of Energy, in terms of $\hat{c}_v$ and T, can be written as shown in Eq. 5.13. Where, for an ideal gas, $T\left(\frac{\partial p}{\partial T}\right)_{\hat{V}} = p$.

$$\rho\hat{c}_v\frac{DT}{Dt} = -[\nabla \cdot q] - T\left(\frac{\partial p}{\partial T}\right)_{\hat{V}}(\nabla \cdot V) - (\tau : \nabla V) \quad (5.13)$$

---

[1]The dyadic product takes in two vectors and returns a second order tensor called a dyadic.

To conclude, below are the conservation equations which have been used by Alroe et al. [34] and during the modelling of this evaporation model.

$$
\begin{array}{r|l}
\text{Continuity} & \dfrac{\partial \rho}{\partial t} = -\dfrac{1}{r^2}\dfrac{\partial(\rho r^2 V_r)}{\partial r} \\[2ex]
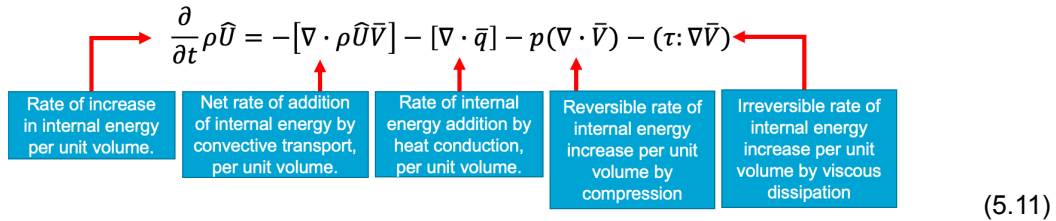\text{Momentum} & \rho\dfrac{\partial V}{\partial t} = -\nabla\cdot(\rho v^2) - \nabla p - [\nabla\cdot\tau] \\[2ex]
\text{Energy} & \rho\hat{c}_v\dfrac{DT}{Dt} = -[\nabla\cdot q] - T\left(\dfrac{\partial p}{\partial T}\right)_{\hat{V}}(\nabla\cdot V) - (\tau:\nabla V)
\end{array}
$$

These general conservation equations will now be written in a system of equations outside the droplet and inside the droplet, based on spherical coordinates (r,θ,ϕ) and an ideal gas $(p = \rho T)$.

Outside the droplet
Conservation of mass:

$$
\frac{\partial \rho}{\partial t} + \frac{1}{r^2}\frac{\partial\left(\rho r^2 u_r\right)}{\partial r} = 0
$$
$$
\frac{\partial \rho_v}{\partial t} = -\frac{1}{r^2}\frac{\partial\left(\rho_v r^2 u_v\right)}{\partial r}
$$

(5.14)

Conservation of momentum:

$$
\rho\frac{D\bar{V}}{Dt} = -[\nabla\cdot\rho\bar{V}\bar{V}] - \nabla p - [\nabla\cdot\tau]
$$

$$
\rho\frac{\partial u_r}{\partial t} + u_r\frac{\partial u_r}{\partial r} = -\frac{\partial p}{\partial r} - \left[\frac{1}{r^2}\frac{\partial}{\partial r}\cancel{(r^2\tau_r r)}\right]
$$

(5.15)

$$
\rho_v\frac{\partial u_v}{\partial t} + u_v\frac{\partial u_v}{\partial r} = -\frac{\partial(\rho_v T_v)}{\partial r}
$$

This equation is based on a symmetrical stress tensor, using an ideal gas $(p = \rho\cdot T)$, and spherical coordinate system.

Conservation of heat:

$$
\rho\frac{D\widehat{U}}{Dt} = -[\nabla\cdot\bar{q}] - p(\nabla\cdot\bar{V}) - (\tau:\nabla\bar{V})
$$

$$
\rho\hat{c}_v\frac{DT}{Dt} = -[\nabla\cdot q] - T\left(\frac{\partial p}{\partial T}\right)_{\hat{V}}(\nabla\cdot u) - \cancel{(\tau:\nabla V)}
$$

(5.16)

$$
\rho\hat{c}_v\left(\frac{\partial T_v}{\partial t} + u_r\frac{\partial T_v}{\partial r}\right) = \frac{1}{r^2}\frac{\partial}{\partial r}\left(r^2\frac{\partial T_v}{\partial r}\right) - p\left[\frac{1}{r^2}\frac{\partial}{\partial r}(r^2 u_r)\right]
$$

Inside the droplet
Heat flux at $r = 0$:

$$
\frac{\partial T_l}{\partial r}(0,t) = 0
$$

(5.17)

Conservation of heat:

$$
\rho\frac{D\widehat{U}}{Dt} = -[\nabla\cdot\bar{q}] - p(\nabla\cdot\bar{V}) - (\tau:\nabla\bar{V})
$$

$$
\rho\hat{c}_v\frac{DT}{Dt} = -[\nabla\cdot q] - T\left(\frac{\partial p}{\partial T}\right)_{\hat{V}}(\nabla\cdot u) - \cancel{(\tau:\nabla u)}
$$

(5.18)

$$
\rho\hat{c}_v\left(\frac{\partial T_l}{\partial t} + u_r\cancel{\frac{\partial T_l}{\partial r}}\right) = \frac{1}{r^2}\frac{\partial}{\partial r}\left(r^2\frac{\partial T_l}{\partial r}\right) - \cancel{p\left[\frac{1}{r^2}\frac{\partial}{\partial r}(r^2 u_r)\right]}
$$

$$
\rho\hat{c}_v\frac{\partial T_l}{\partial t} = \frac{1}{r^2}\frac{\partial}{\partial r}\left(r^2\frac{\partial T_l}{\partial r}\right)
$$

Where, $T\left(\frac{\partial p}{\partial T}\right)_{\hat{V}} = p$, and further simplification of the term $p(\nabla\cdot\bar{V})$ is possible using the Equation of Continuity. Because of the assumption that there is no mass flow within the droplet, this term is neglected. This will be covered in more detail below.

Next, outer boundary conditions were established. These prevent any flows at the centre of the droplet and apply Dirichlet boundary conditions at the far vapour boundary, as it is sufficiently distant

to be unaffected by the droplet over time. In accord with derivations by Lock [36], boundary conditions are applied across the liquid/vapour interface. These boundary conditions enforce the continuity of temperature and mass, momentum, and energy flux. To provide a relationship between the temperature and pressure at the interface, during the phase change process, it will be necessary to include the Clausius-Clapeyron equation [36]. The general form of this equation assumes equal pressures across the interface. To avoid this assumption, Lock examined the continuity of the specific Gibbs function. The mathematical description of the Gibbs energy equation and the complete derivation leading to the modified form of the Clausius-Clapeyron equation can be found in Appendix 9.3.1 [34, 37]. The modified form of the Clausius-Clapeyron equation is shown below:

$$\frac{1}{\rho_v}\frac{dp_v}{dt} - \frac{1}{\rho_l}\frac{dp_l}{dt} = \frac{L}{T_v}\frac{dT_v}{dt} \tag{5.19}$$

Collectively, these equations and boundary conditions form a closed system; however, solving such a highly coupled and non-linear system presents a challenging task. Thus, some simplifications are necessary. Firstly, it is assumed that the vapour can be modelled as an ideal gas and that the liquid is an in-compressible fluid. The former assumption removes vapour pressure from the list of parameters by relating it to density and temperature through the ideal gas law. This can be consider a valid assumption, as the ideal gas law usually agrees with the behaviour of real gases to within 5% at normal temperature and pressure. At low temperatures or high pressures, real gases deviate significantly from ideal gas behaviour [38]. The in-compressible fluid assumption leads to three additional assumptions: constant liquid pressure, no mass flow within the droplet, and no viscous stresses in either phase. As a result, both the conservation of mass and momentum equations can be eliminated from the liquid phase.

Using the previously described general conservation equations inside and outside the droplet, Alroe et al. [34] examined the temperature dependence of physical parameters such as thermal conductivity, thermal diffusivity, and surface tension. In each case, for the relevant temperature ranges, the parameters did not vary significantly and were approximated as constants. After non-dimensionalising the system with the initial droplet radius set equal to one, the original system of equations was obtained. This original system of equations can be found in Appendix 9.3.2. Non-dimensionalising the remaining equations and boundary conditions removed their dependence on units of measurement, grouped any scaling constants as coefficients and allowed an order of magnitude analysis to be performed. The magnitudes of the proportionality constants $v_1 - v_{11}$ were considered by examining the typical ranges of their component parameters. As a result of non-dimensionalising, two coefficients were found to be very small. It demonstrated that v_{11} and the reciprocal of v_2 were very small in comparison to the other proportionality constants. By approximating these two parameters are equal to zero, Alroe et al. [34] performed a perturbation analysis to identify the specific terms that had a negligible influence over the behaviour of the droplet. Conducting this perturbation expansion tested the significance of these terms, as covered by Bush [39]. He demonstrated that the conservation of momentum equation for the vapour phase was equal to:

$$\frac{\partial \rho_v T_v}{\partial r} \approx 0 \tag{5.20}$$

and therefore resulted in:

$$\rho_v = \frac{1}{T_v} \tag{5.21}$$

As a result, $\frac{1}{v_2}$ occurs in the following conservation of momentum equation for the vapour phase. This implies that any changes in the vapour pressure are insignificant. It reduced the conservation of momentum equation in the vapour phase to a simple statement of the isobaric condition.

$$\frac{1}{v_2}\rho_v\left[\frac{\partial u_v}{\partial t} + u_v\frac{\partial u_v}{\partial r}\right] = -\frac{\partial(\rho_v T_v)}{\partial r} \tag{5.22}$$

The second small coefficient, v_{11}, can be seen in the following inter-facial boundary condition. It was derived from the continuity of momentum.

$$\rho_v T_v = p_l - \frac{v_{10}\sigma}{R} + v_{11}u_v\frac{dR}{dt} \tag{5.23}$$

This equation describes an equilibrium of forces at the interface. Thus, the negligible magnitude of v_{11} implies a minimal contribution from vapour evaporating from the surface of the droplet. Using this result and some additional manipulation of the original system of equations, a significantly reduced system was achieved that only relied on the conservation of heat in the liquid phase, and conservation of mass in the vapour phase. This reduced system of equations can be found in Appendix 9.3.3.

Next, Alroe et al. [34] stated that it would be convenient to fix the moving interface by applying a spatial scaling to numerically solve the system. Therefore, an approach mentioned by Crank [40] was used that involved the following Landau scaling, where x becomes the scaled spatial parameter and $R(t)$ is the position of the moving interface.

$$r = xR(t) \tag{5.24}$$

The scaling of Eq. 5.24 is ideal within the droplet itself, but not within the vapour phase. As the droplet radius decreases due to evaporation, the Landau scaling progressively reduces the relative size of the vapour phase. This makes the Dirichlet boundary condition increasingly inaccurate. To maintain a fixed interface position, the following spatial translation in the vapour phase was applied.

$$r = x + R(t) - 1 \tag{5.25}$$

As a result of these simplifications and the spatial transformations, the following reduced system of equations was obtained:

Liquid phase (Conservation of heat):

$$\frac{\partial T_l}{\partial \tau} = \frac{\dot{R}x}{R}\frac{\partial T_l}{\partial x} + \left(\frac{v_1}{R^2 x^2}\right)\frac{\partial}{\partial x}\left[x^2 \frac{\partial T_l}{\partial x}\right] \tag{5.26}$$

Vapour phase (Conservation of mass):

$$\frac{\partial}{\partial \tau}\left[\frac{1}{T_v}\right] = \dot{R}\frac{\partial}{\partial x}\left[\frac{1}{T_v}\right] - \frac{v_3}{(1+v_4)r^2}\frac{\partial}{\partial x}\left[\frac{r^2}{T_v}\frac{\partial T_v}{\partial x}\right] \tag{5.27}$$

Initial conditions:

$$T_l(x,0) = 1 \quad ; \quad T_v(x,0) = 1 \quad ; \quad R(0) = 1$$

Outer boundary conditions:

$$\frac{\partial T_l}{\partial x}(0,t) = 0 \quad ; \quad \lim_{x \to \infty} T_v(x,\tau) = 1 \tag{5.28}$$

Boundary conditions at the droplet surface:

$$T_l = v_5 T_v \quad ; \quad T_v = T_i \exp\left(\frac{v_{10}\sigma}{v_8 v_9}\left(1 - \frac{1}{R}\right)\right) \tag{5.29}$$

$$\dot{R} = \frac{1}{v_7}\left(v_6 \frac{\partial T_l}{\partial x} - \frac{\partial T_v}{\partial x}\right) \quad ; \quad T_i = \frac{L}{\hat{R}}\left(\frac{T_b}{\frac{L}{\hat{R}} - T_b \ln\left(\frac{p_v}{p_b}\right)}\right) \tag{5.30}$$

It is now possible to apply spatial and temporal discretisations to allow the reduced system to be solved numerically. As outlined by Patankar [41], these equations are well suited to a control volume scheme for spatial discretisation, due to their conservative nature. Alroe et al. [34] applied this technique to Eq. 5.26 by integrating across the control volume, which resulted in the following equation for the conservation of heat at the liquid phase:

$$\frac{\partial T_p}{\partial \tau} = \frac{3}{x_e^3 - x_w^3}\left[\frac{(x_e^4 - x_w^4)}{4}\frac{\dot{R}}{R}\frac{\partial T_p}{\partial x} + \frac{v_1}{R^2}\left(x_e^2 \frac{\partial T_e}{\partial x} - x_w^2 \frac{\partial T_w}{\partial x}\right)\right] \tag{5.31}$$

Where, the subscripts e and w refer to values at the east and west face of the control volume, and the p subscript refers to values at the central node. The non-linear terms were manage by assuming that the temporal derivative of T_l on the left hand side and the spatial derivative in the advective term were approximately constant across the control volume.

Next, temporal discretisation was applied by the integration of Eq. 5.31 over a discrete timestep with the use of the backward Euler, or implicit Euler, method to minimise any instability. The non-linearity in the advective term was managed by lagging the spatial derivative and using its value from the previous iteration.

$$T_p^{n+1} - T_p^n = \frac{3}{x_e^3 - x_w^3}\left[\frac{x_e^4 - x_w^4}{4} \frac{\partial T_p^m}{\partial x} \ln\left(\frac{R^{n+1}}{R^n} \right) \frac{\Delta\tau\, v_1}{(R^{n+1})^2}\left(x_e^2 \frac{\partial T_e^{n+1}}{\partial x} - x_w^2 \frac{\partial T_w^{n+1}}{\partial x} \right) \right] \tag{5.32}$$

Alroe et al. [34] applied a similar process to Eq. 5.27; however, the non-linearity within the diffusion term required the use of an averaging scheme and lagging. This resulted in the following equation for the conservation of mass at the vapour phase:

$$\frac{\partial}{\partial\tau}\left[\frac{1}{T_p}\right] = \dot{R}\frac{\partial}{\partial x}\left[\frac{1}{T_p}\right] - \frac{v_3}{(1+v_4)r^2}\frac{\partial}{\partial x}\left[\frac{r^2}{T_p}\frac{\partial T_p}{\partial x}\right] \tag{5.33}$$

$$\frac{1}{T_p^{n+1}} - \frac{1}{T_p^n} = \Delta\tau\left[\left(\dot{R}\frac{\partial}{\partial x}\frac{1}{T_p}\right) - \frac{1}{r^2}\frac{\partial}{\partial x}\left(\frac{2\,v_3}{(1+v_4)}\frac{r^2}{T_p}\frac{\partial T_p}{\partial x}\right)\right] \tag{5.34}$$

Finally, these two equations (Eq. 5.32 and Eq. 5.34) were numerically solved using MATLAB. This numerical solver applied the Newton–Raphson method to iteratively solve for droplet radius and temperature at each timestep. Moreover, it utilised mesh refinement in the vicinity of the interface to improve the accuracy of the finite volume approximations. This resulted in an efficient, stable convergence of the solution at each timestep through adaptive timestepping.

5.3. Results

In order to verify the model, it must behave similar to established rules of droplet evaporation. In particular, it needs to follow the D^2-law, as discussed by McGaughey et al. [42] and Dodge et al. [27]. This law was the first widely accepted theory developed to model droplet evaporation. It predicts that the square of the droplet diameter will change linearly over time. The behaviour was investigated using an initial simulated droplet evaporation. For this simulation, an initial droplet size diameter of 100 µm was used. The temperature of the methanol was set at 15°C, while the air temperature was set at 50°C. Lastly, the ratio partial pressure of methanol vapour at interface was set at 0.211%. This value "*ratio partial pressure of methanol vapour at interface*" is the ratio between partial pressure of methanol over the saturated vapour pressure at variable temperatures conditions. The saturated vapour pressure of methanol was determined using the Antoine equation, as shown below [43]:

$$\log_{10}(P_{sat}) = A - \frac{B}{(T+C)} \rightarrow P_{sat} = 10^{A - \frac{B}{(C+T)}} \cdot 10^5$$

Where, P_{sat} is the vapour pressure in Pa, T is the temperature in K, and coefficients A, B, and C are temperature dependent. In this case, the Antoine equation used the coefficients determined for a temperature between 288.1 and 356.83 K by Ambrose and Sprake [44]. The actual partial pressure of methanol was determined using a look-up table for the specific air temperature, selected volume, injector type, and specific injection timing; these four parameters were also present in the custom built experimental setup, as will be described in Section 6.1.1. In this case an air temperature of 50°C, a 22 litre volume, the Bosch EV14 237 g/min injector, and 350 ms of injection duration were selected as baseline. Figure 5.2 and Figure 5.3 show that there is a complete droplet evaporation (100 µm diameter) within one second (860 ms) and the square of the droplet diameter closely approximates the linear trend. This provides support for the model to follow the D^2-law.
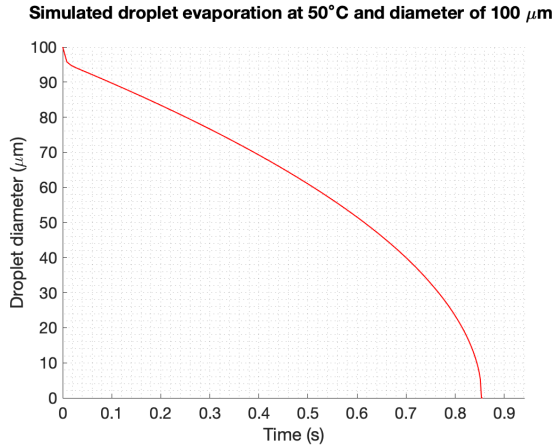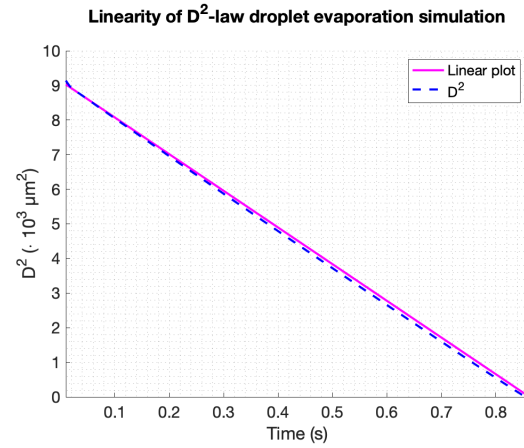
Figure 5.2: Droplet evaporation simulation at 50°C

Figure 5.3: Comparison of D^2-law to an arbitrary linear function

Next, the evolution of the temperature profiles in the vicinity of the liquid/vapour interface were examined. Figure 5.4 shows the temperature throughout the liquid phase. It indicates that the liquid phase requires less than 90 ms to reach the same level as the interface. At this point, the entire liquid phase has a uniform temperature, approx. -50°C. Thus, no heat flow can occur from the interface into the liquid. However, the steep temperature gradients in the vapour phase guarantees heat flow from the vapour phase into the interface. Therefore, in order to avoid violating the conservation of energy equation, it is necessary for the interface to move left into the liquid phase. This clearly shows that the imbalance in heat flux is the driving mechanism behind the evaporation process [34]. As similar explanation on the spray evaporation was given by Heywood [19], as previously described in Section 3.4. In addition, some important boundary conditions must be explained. Figure 5.4 assumes the most extreme and ideal situation, considering a pure liquid droplet suspended in an atmosphere of its own pure vapour. The ratio of pure vapour was calculated and set as a constant of 0.211%, as described above; and considers only the partial pressure of methanol and no other partial pressures e.g., water vapour. It is the ratio of partial pressure of methanol vapour directly outside the interface and is kept constant during the evaporation of the droplet, i.e. a simplification of reality. This results in the steep temperature drop to -50°C at the interface at the start of evaporation, from +50°C at an infinite distance away from the droplet. Both the liquid temperature and vapour temperature at liquid/vapour boundary are calculated using the two equations listed in Eq. 5.29. It must also be noted that the temperature at an infinite distance from the droplet remains equal to the set parameter of 50°C. The temperature decrease was not implemented into the model and will remain constant. Subsequently, the temperature decrease of the liquid phase is consistent with theory described by Heywood [19]. He uses the steady-flow energy equation for a constant-pressure flow with liquid fuel evaporation and heat transfer, as shown below:

$$[\dot{m}_a h_a + (1 - x_e)\dot{m}_f h_{f,L} + x_e \dot{m}_f h_{f,V}]_A = \dot{Q} + (\dot{m}_a h_a + \dot{m}_f h_{f,L})_B$$

This steady-flow energy equation can be rewritten into Eq. 5.35, with the temperature before evaporation (B) and after evaporation (A). Approximating the change in enthalpy per unit mass of each component of the mixture by $c_p \Delta T$, and where $h_{f,V} - h_{f,L} = h_{f,LV}$ is the (latent) heat of vaporisation or enthalpy of vaporisation.

$$T_A - T_B = \frac{(\dot{Q}/\dot{m}_a) - x_e(F/A)h_{f,LV}}{c_{p,a} + (F/A)c_{f,L}} \tag{5.35}$$

Where, $\dot{Q}$ is the heat transfer rate, $\dot{m}$ is the mass transfer rate, x_e is the mass fraction evaporated, $h_{f,LV}$ is the enthalpy of vaporisation, F/A is the fuel/air ratio, and c_p is the specific heat coefficient. The subscripts denote: a air properties; f fuel properties; L liquid; V vapour. Since $c_{f_L} \approx 2c_p$ the last term in the denominator can often be neglected.

Heywood states that if no heat transfer to the inlet mixture occurs, the mixture temperature decreases as liquid fuel is vaporised. For the complete evaporation of methanol and using an equivalence ratio (ϕ) of one, i.e the ratio of the actual fuel-air ratio to the stoichiometric ratio, the value $T_A - T_B$ would be -128°C. In practice, heating occurs and the methanol is not necessarily fully evaporated prior to

entry into the cylinder [19]. Moreover, the value $T_A - T_B$ of Heywood uses a c_p of air, while the temperature profiles are plotted in an extremely ideal situation that considers a pure liquid droplet suspended in an atmosphere of its own pure vapour. This gives a possible explanation regarding the difference in ΔT from the theory and plotted results having a ΔT of -100°C. It could therefore be discussed that the temperature decrease to -50°C in the liquid phase is physically possible in this specific model and using these the set boundary conditions and assumptions.
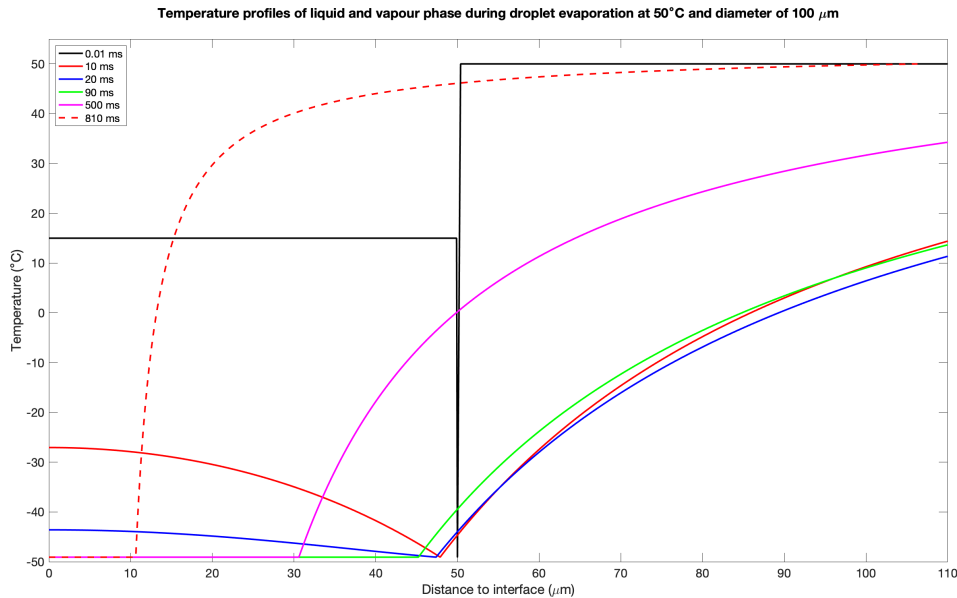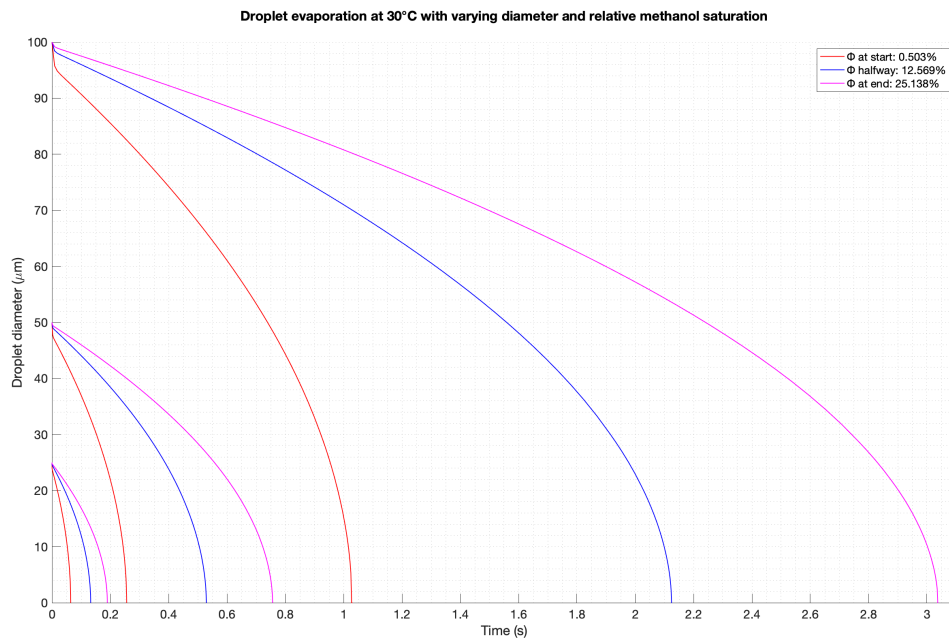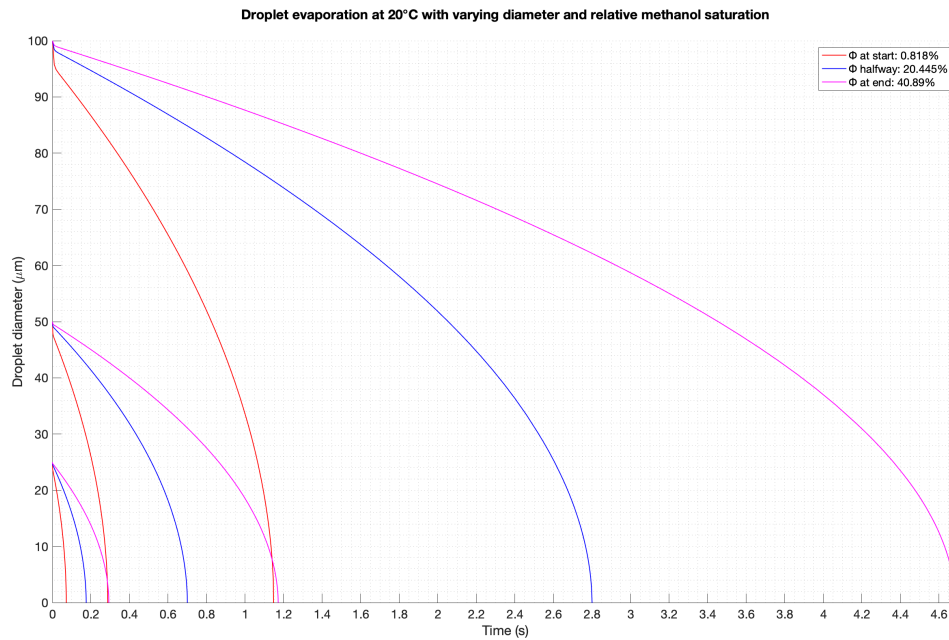

Figure 5.4: Overview of temperature profiles near liquid-vapour interface

In order to investigate the response to changing conditions, three sets of simulations have been performed under the same initial temperature conditions. But with three different droplet size diameters; 100 µm, 50 µm and 25 µm, and with a varying partial pressure ratio of methanol vapour at the interface. As previously described above, the value "*ratio partial pressure of methanol vapour at interface*" is the ratio between partial pressure of methanol over the saturated vapour pressure at variable temperatures conditions. It was determined using a look-up table at the specific air temperature and during three different stages of the evaporation; at the start of injection (no methanol present), halfway, and at the end of injection. This simulates the saturation of the air with methanol, thus slowing down the overall evaporation process. We could compare this with our understanding of the evaporation of water. Increasing the humidity in the air results in a slower evaporation rate, as the vapour content in the surrounding atmosphere approaches the saturated vapour pressure. Moreover, the saturated vapour pressure increases with an increase in temperature. Thus, lowering the partial pressure ratio at the interface at a higher air temperature, as clearly shown in the plotted figures below. The look-up table was generated using a MATLAB script to solve the ratio partial pressure over the saturated vapour pressure of methanol at various temperatures. It utilises the thermodynamic properties of methanol described by Goodwin [45]. Figure 5.5–5.7 depict the simulations at 20°C, 30°C, and 50°C. It clearly indicates that with an increasing partial pressure ratio of methanol vapour, the evaporation rate slows down. In each of the three simulations, the expected linear change in the square of the diameter was visualised. This would demonstrate the appropriate change to the evaporation rate and sufficiently confirms the validity of the model.

Figure 5.5: Droplet evaporation 20°C with varying diameter and relative methanol saturation

Figure 5.6: Droplet evaporation 30°C with varying diameter and relative methanol saturation

Based on the three figures, it can be concluded that with an increasing temperature and decreasing droplet diameter the evaporation rate of a single-droplet increases, i.e. the droplet evaporates faster. Figure 5.7 shows that with an air temperature of 50°C and droplet diameter of 100 µm, the evaporation of a single droplet takes between 1800 and 860 ms. This reduces to between 480 and 210 ms with a droplet diameter of 50 µm, and between 110 and 50 ms with a droplet diameter of 25 µm. The spray characteristics, especially the fine-spray of the port-fuel injector, are of great importance on the influence of the evaporation process inside the scavenger air inlet. Smaller droplets and a higher temperature result in a faster evaporation process, as previously stated in the literature and covered in Section 3.6.
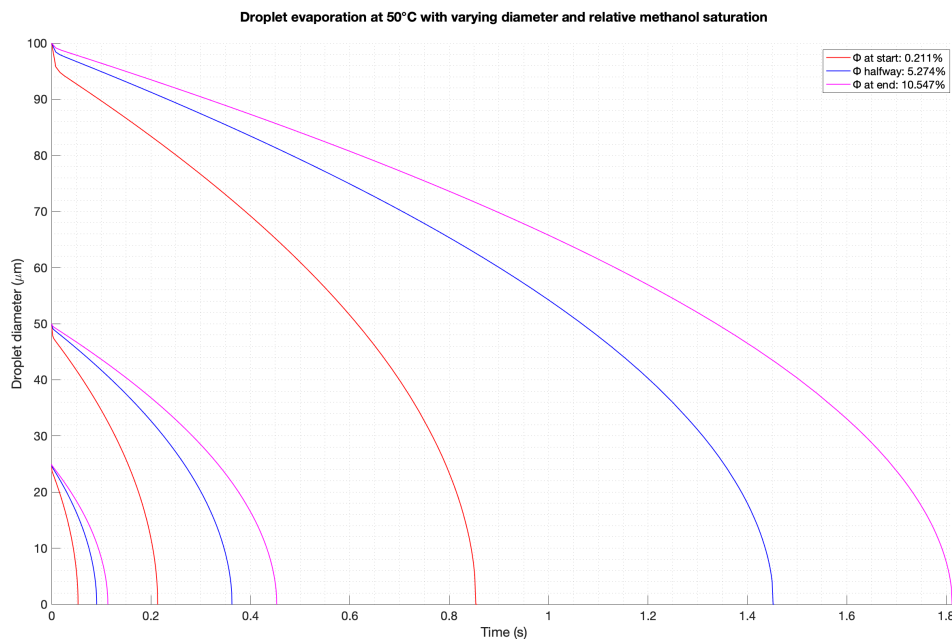
Figure 5.7: Droplet evaporation 50°C with varying diameter and relative methanol saturation

5.4. Sub-conclusion

The main objective of this chapter was to develop an one-dimensional mathematical single-droplet evaporation model for the evaporation of methanol droplets. To achieve this goal, a literature study was preformed to investigate the operating principle and modelling methodology of a single-droplet evaporation model. This mainly led to literature from Alroe et al. [34] and Dodge et al. [27], whom described such a single-droplet evaporation model and eventually led to the basis of a similar single-droplet evaporation model. In addition, the results generated by the evaporation model will answer the following three sub-questions:

- *How could the evaporation process of methanol be modelled, using a single-droplet evaporation model?*
- *What is the influence of fine-spray port-fuel injectors on the evaporation process inside the scavenger air inlet?*
- *How can the evaporation process of methanol inside scavenger air inlet be improved?*

It was noted that the droplet evaporation process is not a trivial task, as it is affected by a great number of parameters and environmental conditions. To answer the first sub-question, an one-dimensional mathematical model for the evaporation of a pure liquid droplet suspended in its own vapour was developed. In an attempt to account for all relevant transport mechanisms, a "first principles" approach was taken by developing the model from fundamental conservation equations. With the use of perturbation analysis, a reduced system of equations was achieved and solved numerically with MATLAB. Although the model required a limited set of assumptions to assist with the numerical analysis, it demonstrated a realistic response to the temperature, droplet size, and ratio partial pressure over the saturated vapour pressure of methanol. Moreover, all simulations consistently followed the D^2-law, validating the model. The model demonstrated that the evaporation is ultimately governed by imbalances in heat flow from the vapour phase into the liquid/vapour interface; and the necessity for the interface to move left into the liquid phase to avoid violating the conservation of energy equation. Note that the model did not include the temperature decrease of the vapour phase due to the evaporation of the droplet.

To answer the second and third sub-question, it was concluded that with an increased temperature and decreased droplet diameter the evaporation rate of the single-droplet increased. This makes the spray characteristics of the port-fuel injector of great importance on the influence of the evaporation process inside the scavenger air inlet. Simulating smaller droplets produced by the port-fuel injector and higher temperatures inside the scavenger air inlet both resulted in a faster evaporation process. This conclusion was already mentioned in the literature and covered in Section 3.6, but is now visualised and verified with this one-dimensional mathematical single-droplet evaporation model. Another influence

that was simulated and verified in the model was the varying partial pressure ratio of methanol vapour at the interface. It simulated the saturation of the air with methanol, and looked at three different stages of the evaporation; at the start of injection (no methanol present), halfway, and at the end of injection. This saturation of the air with methanol slowed down the overall evaporation process, as is the case with the evaporation of water. An increase in the humidity of the air will result in a slower evaporation rate. Because the vapour content in the surrounding atmosphere approaches the saturated vapour pressure. This saturated vapour pressure increases with an increase in temperature, consequently lowering the partial pressure ratio at the interface. To conclude, the droplet size, scavenger air temperature and liquid temperature, and the partial pressure ratio of methanol vapour at the interface are the only parameters that have a large effect on the evaporation rate of the single-droplet evaporation model. However, some parameters have a greater impact to the evaporation rate compared to others.

5.4.1. Future developments

This section will shortly describe future developments to further improve on the developed one-dimensional mathematical single-droplet evaporation model for the evaporation of methanol droplets, as well as the evaporation model in general. The most important recommendation is to extend the modelling framework of the single-droplet evaporation model. It would result in the next step to include the heat transfer between the methanol droplet, liquid/vapour interface, and the surrounding air and hot engine parts, as this would directly influence the evaporation process. The current single-droplet evaporation model is too limited in its ability to display the engine-like evaporation process, a switch to Computational Fluid Dynamics (CFD) modelling is therefore recommended to further investigate the evaporation process in more detail. In addition, this model assumes the most extreme and ideal situation at the liquid-vapour interface. It considers a constant vapour ratio directly outside of the interface, which does not vary during the evaporation of the droplet. This assumption is a strong simplification considering the real-life situation, whereby the vapour ratio increases over time during the evaporation process (as a function of the distance from the interface of the droplet) and partial pressures of for example water vapour plays a role. It is therefore recommended to improve upon this process analytically by considering multiple layers of increasing vapour ratios around the droplet. This would simulate the evaporation process over time and its impact on the temperature profiles. Next, to solve the highly coupled and non-linear system, some simplifications were performed. These simplifications may have led to imperfections in the mathematical description, which may have influenced the results. For this reason, further mathematical analysis and the necessity to carry out additional experimental research would be required. Moreover, further improvements could be to add droplet size distribution to the model, as well as consider the effect of multiple droplets. This would require the development of a multi-droplet evaporation model, or a switch to CFD modelling. Another future development would be to connect the evaporation model to a heat release rate model of the inlet manifold and, subsequently, to the in-cylinder heat release rate model designed for the Caterpillar G3508A test-engine by Bosklopper [11].

<div align="right">

6

</div>

Experimental Research

This chapter will cover the measurements and verification and/or validation of the single-droplet evaporation model. It will describe the custom built experimental setup able to test various low-pressure injection nozzles at atmospheric pressure and temperature, as well as measure their individual spray characteristics and droplet size in those conditions using the shadowgraphy technique. This droplet size is of meaningful importance, as it has a significant effect on the evaporation time of a single droplet. Subsequently to the measurements and post-processing, an attempt in validating the single-droplet evaporation model will be made using this post-processed data. It was expected that both the initial droplet size and the evaporation time of the spray from the experimental setup were to be determined from the post-processed data. Unfortunately, it became immediately clear that the current setup did not allow the ethanol spray to evaporate within the evaporation chamber, resulting in a spray to the back-glass of the chamber. Nevertheless, the post-processed data was used to determine the initial droplet size, droplet speed, and overall spray pattern generated by the injection nozzle. This was still qualified as valuable information, as such data was not yet available and gave an overall inside into the injection process of the Bosch EV14 injector.

6.1. Measurements

6.1.1. Experimental Setup

During this research, various iterations of the experimental setup have been designed. Only the final iteration will be covered in this section. The custom built experimental setup consists of three subsystems; an evaporation chamber, a fuel system and injector, and an electronic control system. The experimental setup tried to mimic the inlet air receiver of the Caterpillar G3508A test-engine, as shown in red in Figure 6.1. However, the conditions of the experiment vary with those in the inlet air receiver. The tests are performed at atmospheric pressure and air temperature, without any airflow, and inside an evaporation chamber volume larger than available in the inlet air receiver.
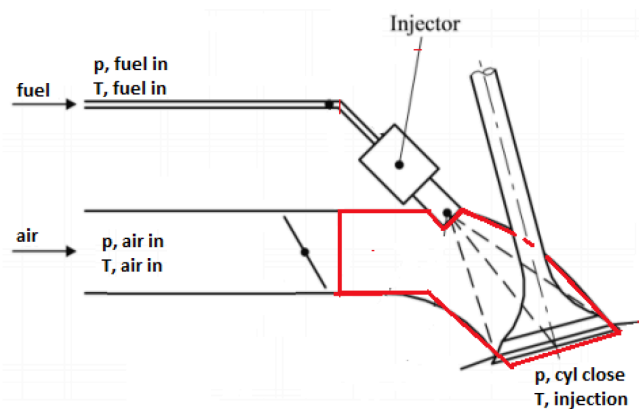

Figure 6.1: General arrangement of inlet air receiver

Evaporation chamber

The evaporation chamber used during the experimental setup was constructed from a 22 litre fish aquarium. This evaporation chamber has a length of 40.5 cm, a width of 25.7 cm, and a height of 22 cm, wherein the injector has been installed longitudinally to the chamber. To prohibit any leaks along the nozzle, an O-ring was installed to seal the opening. In addition, a top cover was manufactured to seal of the volume inside the evaporation chamber. This top cover was fixed using twelve bolts and a gasket, making the evaporation chamber "airtight" from the environment. On top of the top cover, two PT-100 temperature sensors were installed. One sensor was used to measure any temperature change inside the volume due to the evaporation of injected methanol, while the other sensor was used to measure a reference temperature. In addition, a forward-looking infrared (FLIR) camera was available for on the spot temperature measurements of the evaporation chamber, injection spray, and other components of the experimental setup. Figure 6.2 gives a schematic overview of the evaporation chamber and top cover, whereas Figure 6.3 shows a closeup of the constructed evaporation chamber.
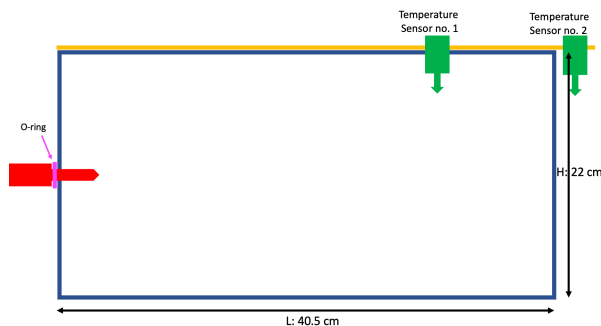

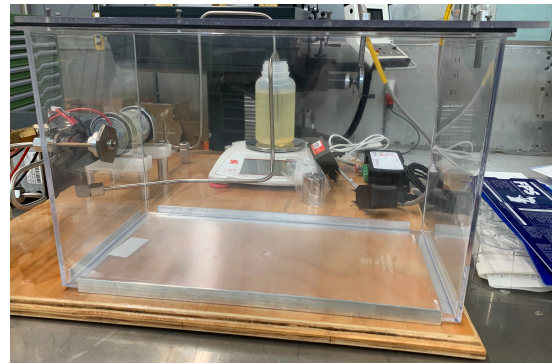Figure 6.2: Schematic front view of evaporation chamber

Figure 6.3: Closeup view of evaporation chamber

Fuel system

In order to supply the injector with sufficient fuel, a separate fuel system had to be designed and constructed. The designed fuel system is schematically visualised in Figure 6.4, whereas a closeup of the constructed fuel system is shown in Figure 6.5. It consists of six different components: a injector, a pressure regulator and pressure transmitter, a fuel pump, a portable balance, and a plastic container acting as fuel tank. The fuel tank is positioned on top of a portable balance. This balance is used to measure the exact amount of fuel being injected into the evaporation chamber. Since the exact mass flow of methanol through a single injector is still unknown, measuring the weight decrease over a specific time-frame could determine the exact amount of fuel being injected. Next, a fuel pump is used to transport the fuel and supply this to the injector. The Bosch FP165 is an inline roller cell pump for the installation outside the fuel tank, and is capable of providing 165 l/h at 5 bar. The delivery volume of the pump could be tuned by changing the operating voltage to the pump, at a constant delivery pressure. After the fuel pump, fuel is delivered to a three-way fuel pressure regulator. This ensures that a constant fuel pressure is supplied to the injector. The fuel pressure regulator is tuned to deliver 5 bar of pressure to the injector, any over-pressure is discharged along a return-line back to the fuel tank. The fuel pressure is measured using a pressure transmitter installed after the regulator. Moreover, the continuous flow through the system is required to cool the fuel pump. Finally, the Bosch EV14 injector is supplied with fuel. For these experimental tests, two different injectors were purchased. The difference between the two injectors was the rated flow rate at the specific operating pressure; one EV14 injector injects 237 g/min n-heptane, while the other injects 670 g/min n-heptane. The Bosch EV14 injector is operated by means of an electronic control system, this system will be covered next.
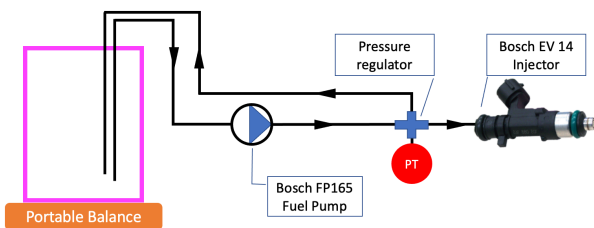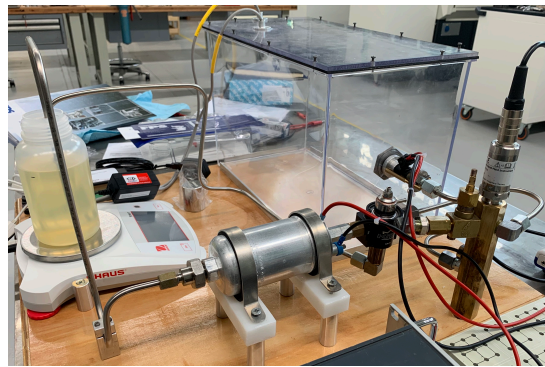
Figure 6.4: Schematic view of fuel system

Figure 6.5: Closeup view of fuel system

Electronic control system

The last sub-system of the custom built experimental setup is an electronic control system used to operate the Bosch EV14 injector. As previously described in Section 4.1, an electrical ECU signal is required to operate the injector. This electrical signal actuates the solenoid coil and has a period and time of injection. The time of injection refers to the time that the needle valve should be open for the passage of fuel, also known as the pulse width. In order to mimic this Electronic Control Unit signal required to open the needle valve, the following electronic control system was build. Figure 6.6 shows the schematic drawing of the electronic control system, whereas Figure 6.7 shows a closeup view of the system. It consists of two transistors (one NPN and one PNP), two resistors (150Ω and 1000Ω), a main power source, and a pulse generator. The pulse generator is used to tune the time of injection by modifying the pulse width. This pulse width is a percentage of the period (T), which is the time taken to complete one cycle. The use of the main power source was necessary because not enough voltage was generated by the pulse generator to actuate the solenoid coil. The working principle of the electronic control system is as follows: in case the pulse generator gives a pulse (U+ control), the basis of the NPN transistor is engaged. This results in a current flow over the collector (C) to the emitter (E), and results in an additional current flow from emitter (E) to basis (B) of the PNP transistor. This current flow engages a flow from the emitter (E) to collector (C) of the PNP transistor, which results in a pulse signal of the main power source (U+ Main) to the injector and back to the negative terminal (U- Main & Control). The two resistors are required to protect the transistors from burning out.
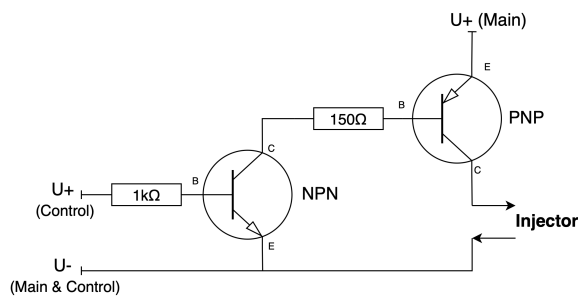

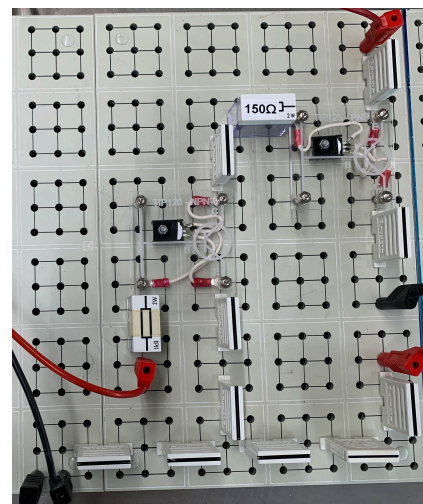Figure 6.6: Schematic drawing of electronic control system

Figure 6.7: Closeup view of electronic control system

6.1.2. Shadowgraphy

For this experimental setup, the shadowgraphy measuring technique is used to measure the droplet size, droplet speed, and overall spray pattern generated by the injection nozzle. The shadowgraphy technique is the simplest form of optical system suitable for observing a flow exhibiting variations of the fluid density. It could therefore be applied and observed in many situations outside of a laboratory with the sun serving as the light source. In principle, shadowgraphy does not need any optical component except a light source and a recording plane, i.e. photographic film, chip or an electronic camera, onto which to project the shadow of the varying density field, as shown in Figure 6.8. An essential feature of the method is the use of a point-shaped light source. The light diverges from its source, and is transmitted through the test object. Because of the inhomogeneous density field a shadow pattern is observed in the vertical plane at a distance behind the object. This shadow effect is generated because the individual light rays are refracted and bent out of their original path, so that the light intensity on the recording plane where the undeflected rays would arrive is altered. At the same time, the position where the deflected rays arrive on the recording plane appear brighter than in the undisturbed environment. As a result, a visible pattern of variations in illumination is produced. For laboratory experiments one often uses an arrangement with a beam of parallel light transmitted through the flow, as shown in Figure 6.9. The camera that records a down-scaled picture is focused by means of the camera lens onto a plane at distance l from the object. The intensity of the shadow effect, or the sensitivity of the shadowgraph, increases with the distance l. On the other hand, a picture is more out of focus with a greater l. Thus, a compromise between optical sensitivity and image quality has to be found [15, 46, 47].
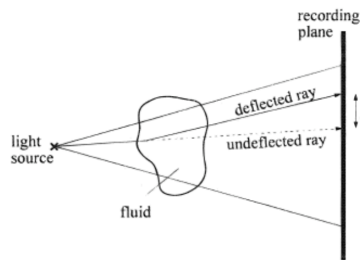
Figure 6.8: Shadowgraphy setup without optical components [15]
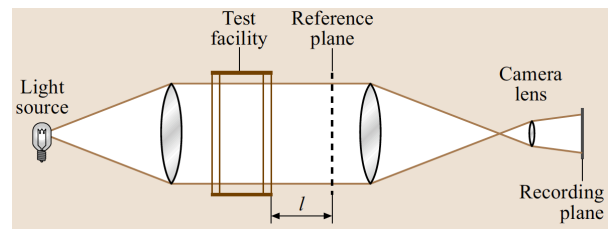
Figure 6.9: Shadowgraphy setup with parallel beams transmitted through test object [47]

Now, using the theory described above, the following shadowgraphy measuring arrangement was installed on the experimental setup in order to measure the droplet size, droplet speed, and overall spray pattern generated by the injection nozzle. The measuring arrangement, shown in Figure 6.10, consisted of the Nikon D7000 digital single-lens reflex camera (left), and the Nikon SB-26 Autofocus Speedlight (right). The Nikon D7000 is a 16.2-megapixel digital single-lens reflex camera (DSLR) which is fitted with a 23.6 mm x 15.6 mm Nikon DX format RGB CMOS sensor, 1.5 times FOV crop, and a 4.78µm pixel size. The Nikon D7000 shoot pictures at a maximum resolution of 4,928 x 3,264 pixels. As a light source, the Nikon SB-26 Autofocus Speedlight was used. This Nikon SB-26 is a versatile camera flash that offers a variety of convenient features to enhance flash photography.
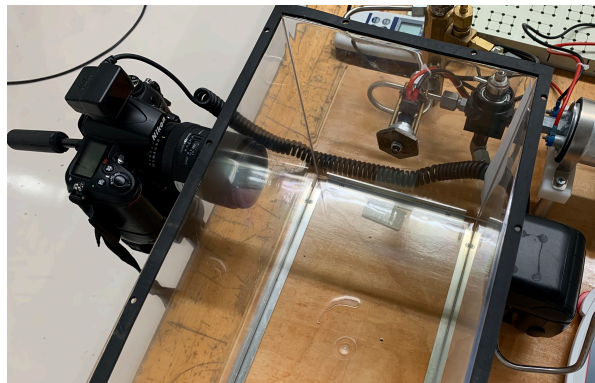
Figure 6.10: General arrangement of shadowgraphy setup

6.1.3. Human Health, Fire Safety, and Environmental Impact

Despite the benefits of methanol as fuel, the substance is met with resistance due to toxicological and fire safety concerns. Bromberg et al. [48] reviewed its safety aspects and concluded that although it is a toxic and dangerous agent, this is also true for all other fuels being considered to substitute gasoline and diesel. A study by Machiele for the US Environmental Protection Agency concluded even that methanol, in many respects, can be actually regarded safer than gasoline [49, 50]. As stated by Verhelst et al. [17], the major issue facing methanol is the toxicity by skin exposure, inhalation or eye contact. Methanol is produced in small amounts in the human body as part of the metabolic process, and occurs naturally in some fruits. However, at high enough concentrations methanol is poisonous. Ingestion of 10 ml can cause blindness, and 60-100 ml can be fatal if the condition is untreated [48]. It must be noted that the toxicity of gasoline is similar to that of methanol, although its toxicity results from different reasons. Symptoms of acute methanol poisoning from direct ingestion include dizziness, nausea, respiratory problems, coma and finally death. However, this process takes between 10 and 48 hours after ingestion, and the cure for acute methanol poisoning is well understood. Curing consists of intravenous administration of ethanol, which the body preferentially metabolises, while the methanol is ejected. Additionally, Bromberg et al. [48] stated that skin or eye contact with methanol, as well as inhalation of methanol vapours are generally of much lower concern, as long as it does not persist for hours. Animal tests, to determine the toxicity of various fuels by inhalation, oral and dermal contact, have shown that the toxicity of alcohol fuels are comparable, and in many cases better, than those of common gasoline or diesel. To conclude, it must be stated that exposure to methanol by humans should be avoided at all times, since high concentrations can lead to death. In order to avoid people from being exposed to methanol, safety must be the main concern when designing fuel systems and storage. Moreover, the safety regulations and emergency protocols for handling methanol must be known to all personal involved.

Fire Safety

When looking at fire safety, methanol shows clear advantages over gasoline. Machiele [50] reports that methanol is not readily ignitable below 10°C, and that it has a similar flammability index to diesel. Comparing methanol and gasoline showed a lower volatility, vapour density and heat release rate in a pool fire. The latter being about 11% lower that gasoline. It also requires a greater concentration to form a combustible mixture in air. Methanol has the significant hazard that its flames are practically invisible in sunlight, but this can be overcome with adding additives. An advantage of methanol, however, is that due to its miscibility, pure methanol fires can be extinguished using water. This inherent fire safety factor makes it well suited for use on board ships.

Environmental Impact

Unlike hydrocarbon fuels, methanol is soluble in water. This makes that methanol is transported at a much faster rate through diffusion and convection in the environment, compared with hydrocarbons. Methanol has a low vapour pressure and will vaporise into air. With volatilization into the air, methanol degrades by reacting with airborne hydroxyl radicals. This is shown in the following equation: $CH_3OH + OH^\bullet = CH_3O^\bullet + H_2O$. If methanol is released into the soil, it is expected to degrade and be susceptible to leaching. Because of its low vapour pressure, rapid evaporation from dry surfaces occurs. Bromberg et al. [48] stated that methanol ground spills migrate substantially through the subsurface water, while the mobility of hydrocarbons is much lower. For example, gasoline will agglomerate above the water table thereby forming Non-Aqueous Liquid Phase pockets. Methanol has also a much faster bio-degradation compared to hydrocarbons. This fast transport and degradation results in shorter lifetimes. On the other hand, hydrocarbons comprise of many stable compounds that include some, such as aromatics, that are highly toxic to bio-organisms and degrade slowly. The half-life time of methanol in the soil (both at the surface and in the ground) is between 1-7 days, and between 3-30 days in the air. This makes that in case of a large methanol spill, the environment is likely to recover quickly [48]. The International Programme on Chemical Safety of the World Health Organization (WHO) investigated the LC50 values of a methanol spill. The LC50 value gives the contamination at which half of the population dies for various organisms. For aquatic organisms, this LC50 range was between 1,300 and 15,900 mg/litre for invertebrates (over a 48 and 96 hour exposure), and between 13,000 and 29,000 mg/litre for fish (over a 96 hour exposure) [51]. However, in the event of such a large scale spill, these exposure times are unlikely to occur due to the high dissipation rate of methanol.

Task Risk Analysis and Safety Data Sheet
Safety is of great importance when executing experiments. For this reason, ethanol instead of methanol was used due to its toxicity and fire safety concerns. Before starting with the experiments a Task Risk Analysis (TRA) for both methanol and ethanol was created to cover all safety aspects of the experiment. This entailed operations with the test setup itself, the filling of the "fuel tank", entry into the room, first aid, firefighting, and decommissioning of the test setup. Moreover, the safety data sheets of methanol and ethanol were carefully studied and implemented into the Task Risk Analysis. The Task Risk Analysis for both methanol and ethanol are listed in Appendices 9.1 and 9.2 respectively.

6.2. Results

After preforming the measurements using the custom built experimental setup, the data had to be post-processed. It was expected that both the initial droplet size and the evaporation time of the spray from the experimental setup were able to be determined from the post-processed data. These parameters would than be used to validate if the single-droplet evaporation model generates a similar evaporation timing at an equal initial droplet size as visualised during the experimental setup. During these experimental tests, the Bosch EV14 injector (237 g/min n-heptane) was used to inject an ethanol spray into the evaporation chamber. The injection pressure was set at 5 bar, with an atmospheric room temperature of around 18°C to 20°C. A rough calculation of the injected mass gave an average of approx. 5 g/s ethanol per injection, based on multiple injections into the evaporation chamber. The original goal was to measure the evaporation process of a single-droplet in the injection spray using the data of the shadowgraphy measuring technique. Unfortunately, it became immediately clear that the current setup did not allow the ethanol spray to evaporate within the evaporation chamber, resulting in a spray to the back-glass of the chamber. It is assumed that this lack of evaporation is simply caused by the very low atmospheric temperature inside the room, which was approx. 18°C. This is expected as the evaporation of a single-droplet of 100 μm in ambient conditions (20°C and atmospheric pressure) takes approx. 980 ms, while the droplet travels across the entire evaporation chamber in approx. 11 ms. It is therefore recommended to perform additional experimental tests at higher atmospheric temperatures inside the evaporation chamber, in order to see if any evaporation might be detected. As a result of the lack of ethanol evaporation, the single-droplet evaporation model could not be validated using the custom built experimental setup.

Measuring equipment
Another problem present with the performed experimental tests was caused by the measuring equipment. The current measuring equipment is insufficient to obtain the desired results, especially focused on the evaporation process and speed of the jet spray generated by the nozzle. This limitation is caused by the flash and camera, which are both of an older type. Because the droplets are passing the camera lens at speeds between 30-35 m/s, they are not clearly visible as droplets but rather appear as white streaks on the photograph. It is therefore recommended to procure better measuring equipment, or implement another measuring technique such as laser diffraction or phase Doppler particle analysis.

6.2.1. Post-processing

Although there was a lack of ethanol evaporation within the evaporation chamber at atmospheric temperature and pressure. The post-processed data was able to measure and reveal the droplet size, droplet speed, and overall spray pattern generated by the injection nozzle. This post-processing looked at four different shadowgraphy photographs; three spray jets between 0-5 cm, 0-10 cm, and 0-20 cm from the nozzle, and one random picture of the periphery of a spray jet. In this case, the spray jet between 0-10 cm will be covered for further explanation. To execute a droplet search by MATLAB, the photography had to be post-processed. This started with subtracting the background of the jet spray photograph, and applying a Neutral Density (N-D) filter, as shown in Figure 6.11. This filter reduces or modifies the intensity of all wavelengths of light equally. As a result, MATLAB was able to execute a droplet search which detected more circular objects with both weak and strong edges, depending on the set threshold. Two different circle radii thresholds were used during the radius search; the first search was set between a circle radius of 5 and 20 pixels, resulting in a total droplet count of 2054 droplets. The second search was set between a circle radius of 1 and 8 pixels, resulting in a total droplet count of 4246 droplets. It must be noted that this count is not an accurate representation of the total amount of droplets in the spray jet, due to the fact a large part of the picture is out of focus. Thus, more droplets are present in the total spray jet as shown and counted in Figure 6.12.
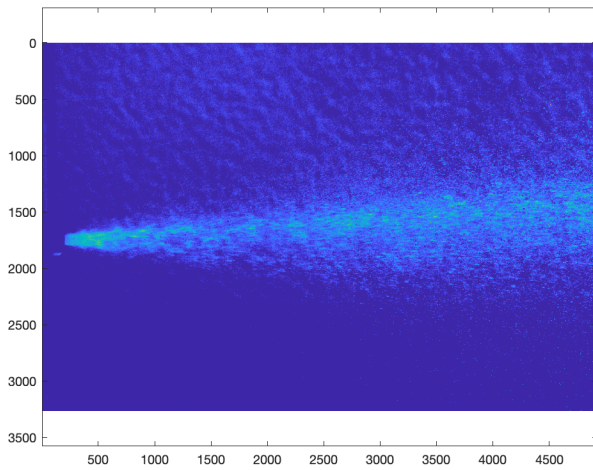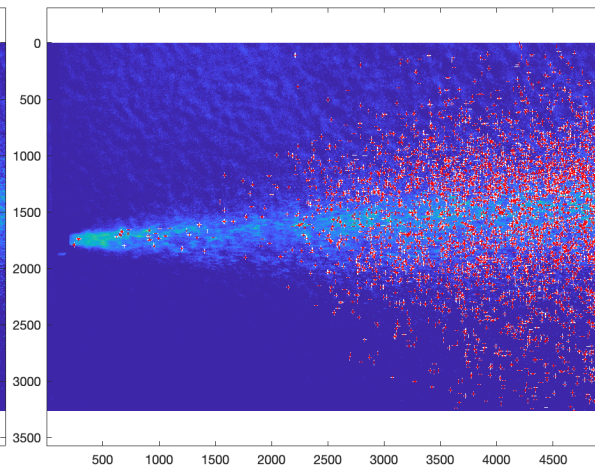
Figure 6.11: N-D filter of jet spray

Figure 6.12: Droplet search of jet spray

The average droplet size could be determined by counting the average amount of pixels for each single droplet and multiplying this with the specific scale of that photograph. This was done on three different photographs; the spray jet between 0-10 cm and 0-20 cm from the nozzle, and one random picture of a periphery of a spray jet. It concluded that the average droplet size was between 100 and 120 μm, with some droplets exceeding 130 μm. Moreover, the average droplet speed was determined at 35.6 m/s, by using the equation for dynamic pressure [52]. It assumed an in-compressible fluid of which the flow speed can be calculated using Eq. 6.1, where the ρ of ethanol is 789 kg/m^3 and the dynamic pressure is 5 bar.

$$p = \tfrac{1}{2}\rho v^2 \rightarrow v = \sqrt{\frac{p}{\tfrac{1}{2} \cdot \rho}} \rightarrow v = \sqrt{\frac{5 \cdot 10^5}{\tfrac{1}{2} \cdot 789}} = 35.6 \; m/s \tag{6.1}$$

Next, the overall spray pattern generated by the injection nozzle was examined, as shown in Figure 6.13. This overall spray pattern gave inside into the overall structure, injection and breakup length, droplet distribution, and spray angle. It is visualised in Figure 6.13 that the spray diverges away from the nozzle. From the literature, the figure confirms the statement that as one moves away from the nozzle, the mass of air within the spray increases, the spray diverges, its width increases, and the spray velocity decreases [19]. Subsequently, it distinguish the liquid-containing core of the jet and the extent of the droplet region of the spray which surrounds the liquid core. This droplet region contains the droplet size distribution of the spray, clearly visualising that more droplets are formed further away from the liquid core as the overall spray velocity decreases, as also visualised in the droplet search of Figure 6.12. The spray angle (α) is defined as the angle the jet forms at the moment when it leaves the nozzle orifice. This spray angle was determined to be 20° which corresponds by with the data sheet of the Bosch EV14 injector valve. The breakup length is defined as a liquid column that disintegrates over a finite length into different droplet sizes. It is divided into a primary and secondary breakup. The primary breakup length is the distance between the nozzle and the disintegration of the liquid sheet into ligaments; the secondary breakup length is the distance between the disintegration of the ligaments into droplets. Lastly, the injection length of the spray is determined, also known as the spray tip penetration. This length is defined as the distance along the spray axis to the boundary of the spray. Based on the performed experiments, the injection spray ended against the back-glass of the evaporation chamber. Thus, it can be stated that the injection length exceeds at least the ±40 cm at atmospheric temperature and pressure.

In addition, it is possible to calculate the horizontal distance a droplet travels, assuming a laminar flow and neglecting its vertical component. This calculation assumes Stokes flow, where the Reynolds number is less than one and thus the particle drag coefficient is inversely proportional to the Reynolds number itself. The horizontal distance is than calculate using the following equation [52, 53]:

$$x = x_0 + \frac{v\rho D^2}{\rho D^2 + 18\mu t} \cdot t \tag{6.2}$$

Where, x_0 is the initial distance, v is the flow velocity of the droplet, ρ is the density of ethanol, D^2 is the diameter of the droplet, μ is the dynamic viscosity of air, and t is the time the droplet is suspended in the air. The derivation of Eq. 6.2 could be found in Appendix 9.4.
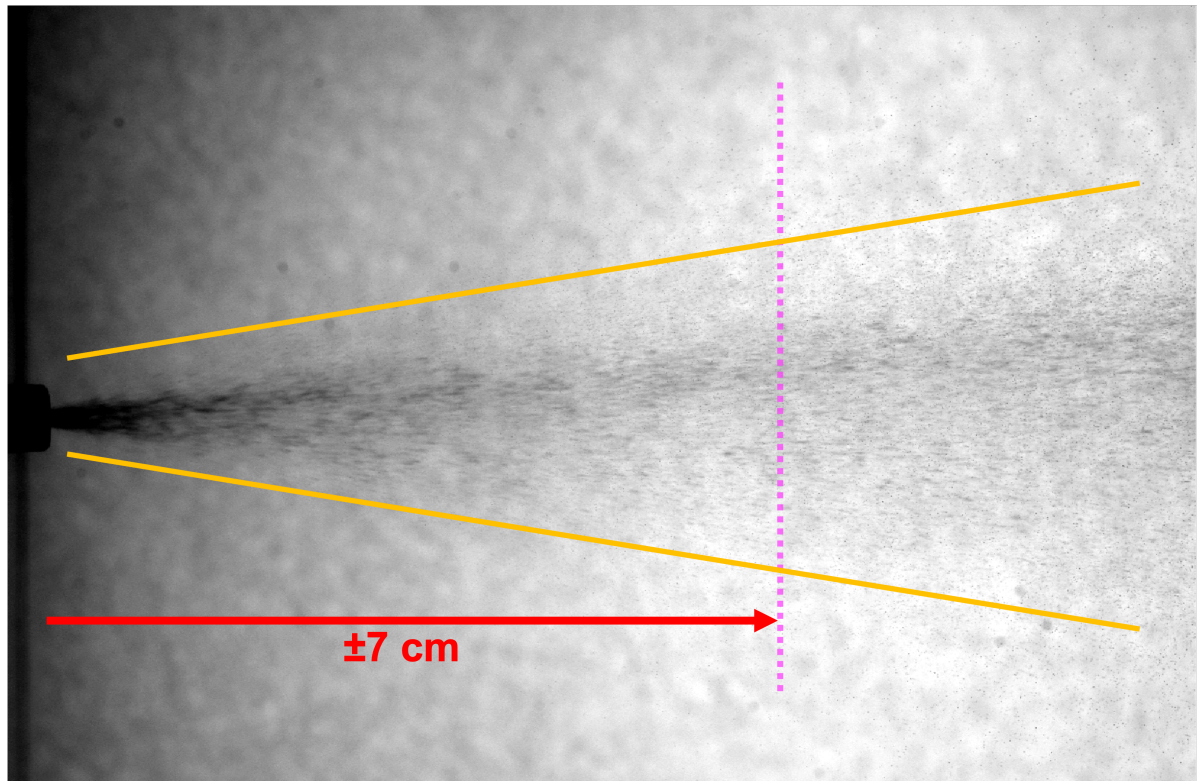
Figure 6.13: Overall spray pattern generated by nozzle

For this calculation, an atmospheric pressure and temperature of 1 atm and 20°C is used. Moreover, this simple calculation does not consider the evaporation of the droplet and influence of gravity. To estimate the horizontal distance, it was assumed that the droplets had to descend 5 feet (approx. 1.5 meter). The US *Centers for Disease Control and Prevention* (CDC) estimated the time it takes for a droplet of 100 µm diameter to descend 5 feet at 5.8 seconds [54]. Thus, the horizontal distance could be calculated using Eq. 6.2.

$$x = x_0 + \frac{v\rho D^2}{\rho D^2 + 18\mu t} \cdot t x = 0 + \frac{35 \cdot 789 \cdot 0.0001^2}{789 \cdot 0.0001^2 + 18 \cdot 1.8 \cdot 10^{-5} \cdot 5.8} \cdot 5.8 = 0.8488 \; m \qquad (6.3)$$

Where the previously mentioned parameters are written as: v is 35 m/s, ρ is 789 kg/m^3, D^2 is 100 µm, μ is $1.8 \cdot 10^{-5} \; \frac{Ns}{m^2}$, and t is 5.8 seconds.

Based on this calculation, it can be stated that a droplet of 100 µm diameter travels a horizontal distance of approximately 85 cm, assuming a laminar flow. In order to check whether the laminar flow assumption is justified for every droplet, the following can be stated. A laminar flow requires a low Reynolds number. The highest Reynolds number for a droplet is realised at the start of injection, as here the higher velocity is present [52, 53]. This Reynolds number is calculated as:

$$Re = \frac{\rho_{air} v_0 D}{\mu_{air}} = \frac{1.2 \cdot 35 \cdot 0.0001}{1.8 \cdot 10^{-5}} = 233.3333$$

Using this Reynolds number for laminar flows to calculate the drag coefficient (C_D) results in a value of 0.103. When comparing this Reynolds number with that of the drag coefficient for a sphere, as obtained from laboratory experiments, gives a C_D value of 0.722. It can be seen that the resistance from the laboratory experiments is higher than the resistance according to the equation for laminar flow. This means that the actual resistance is higher and that the estimated distance is therefore an upper limit. For the first droplet, the laminar assumption will give a reasonable estimate. However, for the second droplet this difference will be much larger. Thus, making this laminar assumption incorrect [53].

6.3. Sub-conclusion

The main objective of the custom built experimental setup was to perform measurements and verify and/or validate of the single-droplet evaporation model. This would answer the final sub-question of this research regarding the modelling of the single-droplet evaporation model.

- *Does the injection and evaporation model give comparable results, as found in the experimental data?*

Unfortunately, it became immediately clear that the current setup did not allow the ethanol spray to evaporate within the evaporation chamber. This resulted in the injection spray hitting the back-glass of the chamber, and is expected as the evaporation of a single-droplet of 100 μm in ambient conditions (20°C and atmospheric pressure) takes approx. 980 ms, while the droplet travels across the entire evaporation chamber in approx. 11 ms. Consequently, this setback prevented the validation of the single-droplet evaporation model and the ability to answer the final sub-question mentioned above. Nevertheless, the post-processed data was used to determine the initial droplet size, droplet speed, and overall spray pattern generated by the injection nozzle. This was still qualified as valuable information, as such data was not yet available and gave in overall inside into the injection process of the Bosch EV14 injector. The post-processed data of the 0-10 cm spray jet was able to detect a total droplet count of 2054 droplets set between a circle radius of 5 and 20 pixels. The second search resulted in a total droplet count of 4246 droplets set between a circle radius of 1 and 8 pixels. It must be noted that this count is not an accurate representation of the total amount of droplets in the entire spray jet, due to the fact a large part of the picture is out of focus. Thus, more droplets are present in the total spray jet as shown and counted. In addition, the average droplet size and droplet speed were determined. It concluded that the average droplet size was between 100 and 120 μm, with some droplets exceeding 130 μm, while the average droplet speed was determined at 35.6 m/s. Subsequently, the overall spray pattern gave inside into the overall structure, injection and breakup length, droplet distribution, and spray angle. Based on the overall structure, the spray diverges away from the nozzle which confirms statements given in the literature [19]. The spray clearly distinguish the liquid-containing core of the jet and the extent of the droplet region of the spray which surrounds the liquid core. This droplet region contains the droplet size distribution of the spray, clearly visualising that more droplets are formed further away from the liquid core as the overall spray velocity decreases. The spray angle (α) was determined to be 20° which corresponds by with the data sheet of the Bosch EV14 injector valve. The breakup length is clearly visible, showing the breakup of the liquid column over a finite length into different droplet sizes. Lastly, the injection length was determined. Based on the performed experiments, the injection spray ended against the back-glass of the evaporation chamber. Thus, it can be stated that the injection length exceeds at least the ±40 cm at atmospheric temperature and pressure. In addition, the horizontal distance a droplet travels was calculated. This calculation stated that a droplet of 100 μm travels a horizontal distance of approx. 85 cm, assuming a laminar flow.

6.3.1. Future developments

This section will shortly describe future developments to further improve upon the custom built experimental setup and its used measuring technique. Because the current setup was not able the detect any ethanol evaporation, the custom built experimental setup could not be used to validate the single-droplet evaporation model. It is therefore recommended to obtain a more advanced experimental setup that could measure the spray and evaporation in engine-like conditions. Especially, the impact of the injection pressure, higher manifold charge pressure, and higher temperatures on the evaporation speed. This more advanced setup would give an inside into the evaporation speed of (m)ethanol. Thus, it could be used to validate the single-droplet evaporation model. An additional modification is recommended to design and build an external camera mount. This mount would facilitate better overall photographs at set and equal distances from the injection nozzle. Moreover, another improvement could be to modify the droplet search script. This script currently searches for circular objects, while the spray generates more elliptical droplets due to its speed across the picture. It is therefore recommended to develop and try an elliptical search script and check whether this detects more droplets as previously found. Lastly, it was found that the current measuring equipment is insufficient to obtain the desired results, especially focused on the evaporation process and speed of the jet spray generated by the nozzle. This limitation is caused by the outdated camera equipment. It is therefore recommended to procure better measuring equipment, or implement another measuring technique such as laser diffraction or phase Doppler particle analysis.

7

Discussion

This chapter discusses the results of the performed research and translates the findings of this report to the real-time situation inside the engine. Especially, the results of the experiment and its influence on the engine regarding the lack of space in the inlet manifold. Consequently, the following three questions need to be answered:

1. What could be concluded from the experimental research?
2. How could this be linked to the engine itself?
3. What could/should be improved to obtain better results during future (full-scale) experiments?

First, based on the experimental research, it became clear that the current setup did not allow the ethanol spray to evaporate within the evaporation chamber. As a result, the injection spray hit the back-glass of the chamber and prevented the validation of the single-droplet evaporation model. On the other hand, the post-processed data was still useful to determine the initial droplet size, droplet speed, and overall spray pattern generated by the injection nozzle. We could conclude that the average droplet size was between 100 and 120 µm, with some droplets exceeding 130 µm. The average droplet speed was determined at 35.6 m/s, and the spray angle was determined at 20°. Subsequently, the injection spray ended against the back-glass of the evaporation chamber. This concluded that the injection length exceeded at least the ±40 cm at atmospheric temperature and pressure, which does not contradict the results of single-droplet evaporation model. In addition, calculations regarding the injection length determined a maximum horizontal droplet distance of approximately 85 cm when assuming a laminar flow and neglecting its vertical component.

Second, the above mentioned results could be linked to the engine itself. As previously described in Chapter 2, the overall vertical distance available for the entire evaporation of methanol inside the scavenger air manifold was determined at approx. 7 cm. This represents the distance between the nozzle and flame arrestor, as shown in Figure 2.2. It shows the total space available to achieve injection and complete evaporation of methanol without causing wall-wetting. From the performed experimental tests, it is known that the injection length exceeded at least the ±40 cm at atmospheric temperature and pressure. Therefore, it could be discussed that the tested injection nozzle did not sufficiently perform under these circumstances, as the methanol jet would have hit the inlet valve. However, the tested atmospheric conditions of the experiment do not represent the conditions in the scavenger air manifold and engine when operating. Based on recent trial runs with the Caterpillar G3508A engine, air temperatures were estimated between 50 and 70°C after the intercooler. The effects of these higher temperatures on the actual injection length and evaporation rate inside the engine are still to be determined. Although a simulated droplet evaporation rate was determined at 860 ms at an air temperature of 50°C, compared to a droplet evaporation rate of 1.1 seconds at an air temperature of 20°C. These results were both based on the developed single-droplet evaporation model and used an average droplet size of 100 µm. It can be concluded that this evaporation rate is insufficient when operating the Caterpillar G3508A engine. As with this engine, only limited time is available for the injection and evaporation of fuel, as stated by the operating manual of Caterpillar-Woodward. As a result, based on the theoretical framework, small droplet sizes and/or higher air temperatures could result in the faster evaporation rate of the methanol inside the scavenger air manifold. Consequently, future research must determine whether these higher air temperatures and/or smaller droplet sizes are sufficiently enough to evaporate all injected methanol within the available space of ±7 cm.

Third, in order to obtain better results during future (full-scale) experiments and measurements, the following improvements are discussed to be implemented and/or researched. The first improvement is based on the single-droplet evaporation model. It could be discussed that the single-droplet assumption is not consistent with the actual inlet manifold conditions, i.e. the spray pattern of the Bosch EV14 injection valves. This leads to the limitation and conclusion that the single-droplet evaporation model is inadequate compared to the actual injection spray consisting of multiple droplets. Thus, a more detailed Computational Fluid Dynamics (CFD) model is required to further investigate the evaporation process. This CFD model would be beneficial in obtaining a more detailed overview of the generated spray pattern and its influence on the multi-droplet evaporation process. The second improvement is based on the custom air-assist injector cap. It will be necessary to validate the claim by Dodge et al. [27], stating that the droplet size of the injector could be further reduced using a custom air-assist injector cap. The necessity in validating this claim would be beneficial in obtaining smaller droplets using the standard Bosch EV14 injection valve. Especially when these droplets are in the range of 10 μm and thus improving the evaporation of the spray. This could be done by manufacturing a replica of the used air-assist injector cap and checking whether similar results are generated in the experimental setup. The third improvement is based on the Bosch EV14 injection valves. Currently, the tested Bosch EV14 injection valves have maximum flow rates which are inadequate to operate the Caterpillar engine at full load and one single injector per cylinder. Future research must therefore be performed in finding injection valves that create droplets with diameter smaller than 100 μm, but still injects sufficient amounts of fuel to operate the engine. The last improvement is based on the experimental setup and subsequent measuring equipment. It could be discussed that the current experimental setup is not consistent with the actual inlet manifold conditions, as the experimental setup works at atmospheric pressure and temperature. This leads to the discussion that a more advanced setup is required to experiment with the injection valves. In order to gain inside into the jet spray generated by the nozzle at higher pressures and the subsequent evaporation process at higher temperatures. Moreover, it was found that the current measuring equipment is insufficient to obtain the desired results, especially focused on the evaporation process and speed of the jet spray generated by the nozzle. Therefore, it could be discussed to procure better measuring equipment, or implement another measuring technique such as laser diffraction or phase Doppler particle analysis.

8
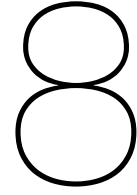
Conclusion & Recommendations

This chapter will give the conclusions and recommendations of this thesis and future work into methanol as a fuel alternative for the maritime sector.

8.1. Conclusions

This report was written to find an answer to the following main research question:
"How could the highest evaporation of methanol inside the scavenger air inlet be obtained before the installed flame arrestor; by varying the injection pressure, inlet air temperature, spray dimensions, and droplet size?

The injection, atomisation, and evaporation of a liquid fuel are important processes in the combustion and emission formation of an internal combustion engine. Previous research showed that the wall-wetting fuel film mass and its evaporation rate directly affect the air-fuel ratio of in-cylinder mixture, as well as the performance of the engine itself. This makes the evaporation of sufficient methanol and reducing its wall-wetting effect the limiting factor. With port-fuel injection, the air-fuel mixture is prepared in the intake manifold itself by injecting the fuel, after which it is fed into the combustion chamber. This requires the production of a methanol spray which is fine enough that a significant portion of the spray would evaporate and follow the airstream directly into the cylinder.

The spray characteristics of methanol can be improved in various ways, based on the theoretical frame work: Firstly, a higher spray pressure makes the formation period of spray decrease and the penetration rate increase, whereas a higher back-pressure inside the inlet manifold leads to the shrinkage of the spray angle [22]. Secondly, an increase in injection pressure results in a significant reduction in droplet size and enhanced atomisation for methanol sprays [25]. Moreover, the droplet size of the injector could be further reduced using a custom air-assist injector cap, as shown by Dodge et al. [27]. Their research used a custom air-assist injector cap to produce cross-section average SMDs of approx. 7.5 μm with fuel-injection pulse widths of 4 ms (idle condition) and SMDs of 9 μm with a 10-ms pulse width, which is a reduction of approx. 93% to the initial diameter. These fine-spray droplets were small enough to follow the airstream past the intake valves and into the engine cylinders. Thirdly, experimental research that varied the fuel temperature, while keeping the ambient temperature constant, showed that the flash-boiling sprays were able to increase the spray angle for rapid fuel–air mixing, and improve the evaporation of the fuel spray tremendously [23]. Fourthly, research found that an increase in ambient gas temperature significantly reduces the methanol liquid penetration and results in a faster evaporation of spray, however, it has only a limited influence on the vapour penetration [26]. Although the spray characteristics of methanol can be improved in various ways. It could be concluded that the important factors for atomisation inside the engine, i.e. a smaller droplet size, could be best achieved either by higher injection pressure or by use of the custom air-assist injector cap.

The evaporation process of methanol inside the scavenger air inlet can be also improved in various ways, based on the theoretical frame work: Firstly, increasing the inlet air temperature results in an improved evaporation of the methanol spray. With an increase in inlet air temperature, the droplet temperature increases due to heat transfer resulting in an increase in fuel vapour pressure and evaporation rate [19]. Secondly, research showed that the developed air-assist cap fitted onto a standard multi-hole port-fuel injector created spray droplets that were fine enough, approximately 20 μm in diameter or smaller, to stay suspended in the air and flow into the cylinder [27]. Subsequently, computer

modelling of the spray evaporation revealed that the droplet evaporation times scaled approximately with the square of the droplet diameter. Their research states that this is true for evaporating methanol sprays until the SMD reaches approx. 10 μm. At or below this droplet size, evaporation of the spray was so fast that the methanol fuel vapour saturated the air in the cylinder almost instantaneously [27]. Further reduction in the droplet size would therefore not increase the evaporation rate. Although the evaporation process of methanol can be improved in various ways. It could be concluded that higher inlet air temperatures and smaller droplets have the greatest effect on the evaporation rate.

The development of the one-dimensional simulation model of a low-pressure injector was focused on reproducing the behaviour of an electrical injector used for port-fuel injection applications. The model is based on a mathematical description of a simplified solenoid valve and mass-spring-damper system and consists of three sub-models; a simplified solenoid model, a valve model, and an injection nozzle model. It can be concluded that the developed mathematical description allowed for the simulation of the injection process to obtain the volumetric flow rate, which is the input for future spatial evaporation models and represents that of the Caterpillar G3508A test-engine. The use of experimental results and subsequent implementation into an empirical model have been an useful tool in the modelling process.

Next, an one-dimensional mathematical single-droplet evaporation model for the evaporation of methanol droplets was developed. However, the droplet evaporation process is not a trivial task, as it is affected by a great number of parameters and environmental conditions. To investigate the effect of this evaporation process, the model assumed a pure liquid droplet suspended in its own vapour. This assumption provided the basis of the single-droplet evaporation model. In an attempt to account for all relevant transport mechanisms, a "first principles" approach was taken by developing the model from fundamental conservation equations. Although the model required a limited set of assumptions to assist with the numerical analysis, it demonstrated a realistic response to the temperature, droplet size, and ratio partial pressure over the saturated vapour pressure of methanol. Moreover, all simulations consistently followed the D^2-law, validating the model. From the evaporation model, it was concluded that with an increased temperature and decreased droplet diameter the evaporation rate of the single-droplet increased. This conclusion was already discovered in the theoretical background, but is now visualised and verified with the evaporation model. For this reason, smaller droplet diameters are required in case of engine-like conditions, preferably less than 20 μm, and the temperature needs to be sufficient for fast evaporation. The exact temperature could not be investigated, as the heat transfer from inlet air and hot engine parts to methanol liquid and vapour were not included into the model. For this spatial (CFD) analysis would be required, that could use the mechanism of this developed single-droplet evaporation model.

The custom built experimental setup is able to test various low-pressure injection nozzles at atmospheric pressure and temperature and measure their individual spray characteristics and droplet size using the shadowgraphy measuring technique. The measurements taken by the experimental setup could not be used to establish the evaporation rates, also, because the evaporation at ambient conditions was very slow. This was expected as the simulated evaporation of a single-droplet of 100 μm in ambient conditions took approx. 980 ms, while the droplet travels across the entire evaporation chamber in approx. 11 ms. However, the current setup could be used to investigate how smaller droplet sizes can be achieved. For evaporation rate experiments, more engine-like conditions are required.

8.2. Recommendations

Based on the performed literature review and research objective of this thesis, the following recommendations can be given on the future work into methanol as a fuel alternative for the maritime sector.

Additional research is required into improving the injector spray characteristics. In order to validate if an increase in spray pressure, higher ambient gas temperatures, and higher back-pressure indeed result in a reduction of droplet size and enhanced atomisation of methanol sprays. This could be checked by means of experimental tests, varying the spray pressure and temperatures. Secondly, it will be necessary to validate the claim by Dodge et al. [27], stating that the droplet size of the injector could be further reduced using a custom air-assist injector cap and thus improve the evaporation of the spray. This could be done by manufacturing a replica of the used air-assist injector cap and checking whether similar results are generated in an experimental setup. Thirdly, additional research is required in validating if an increase in inlet air temperature and back-pressure result in an improved evaporation of the methanol spray. For this a more advanced setup is required that could measure the spray and evaporation in engine-like conditions, such as 3 bar charge pressure and 50 to 90°C inlet air temperature.

An important recommendation regarding the injection model is the spray rate characteristic, which could be used as an input for CFD analysis for the evaporation and combustion of methanol. This additional research entails the spray characteristic, to obtain a simulated spray rate, spray pattern, and droplet size generated by the nozzle tip. Moreover, the low-pressure injection model has not been validated due to a lack of available time and resources. Further research is therefore essential to validate the generated results and improve upon the model's accuracy. This is highly recommended when the low-pressure injection model becomes integrated into other simulation models, e.g., the Heat Release Rate model for the Caterpillar G3508A test-engine.

The most important recommendation is to extend the modelling framework of the single-droplet evaporation model. It would result in the next step to include the heat transfer between the methanol droplet, liquid/vapour interface, and the surrounding air and hot engine parts, as this would directly influence evaporation process. The current single-droplet evaporation model is too limited in its ability to display the engine-like evaporation process. A switch to Computational Fluid Dynamics (CFD) modelling is therefore recommended to further investigate the evaporation process in more detail.
Subsequently, the model assumes the most extreme and ideal situation at the liquid-vapour interface. It considers a constant vapour ratio directly outside of the interface, which does not vary during the evaporation of the droplet. This assumption is a strong simplification considering the real-life situation, whereby the vapour ratio increases over time during the evaporation process (as a function of the distance from the interface of the droplet) and partial pressures of for example water vapour plays a role. It is therefore recommended to improve upon this process analytically by considering multiple layers of increasing vapour ratios around the droplet. This would simulate the evaporation process over time and its impact on the temperature profiles. In addition, this model assumes the most extreme and ideal situation at the liquid-vapour interface. It considers a constant vapour ratio directly outside of the interface, which does not vary during the evaporation of the droplet. This assumption is a strong simplification considering the real-life situation, whereby the vapour ratio increases over time during the evaporation process (as a function of the distance from the interface of the droplet) and partial pressures of for example water vapour plays a role. It is therefore recommended to improve upon this process analytically by considering multiple layers of increasing vapour ratios around the droplet. This would simulate the evaporation process over time and its impact on the temperature profiles.

The performed experimental test showed no evaporation of ethanol within the evaporation chamber, resulting in a spray to the back-glass of the chamber. This is expected as the evaporation of a single-droplet of 100 μm in ambient conditions (20°C and atmospheric pressure) takes approx. 980 ms, while the droplet travels across the entire evaporation chamber in approx. 11 ms. An important recommendation is additional research into the spray characteristics of methanol at low-pressure injection. The current experimental setup is very useful for the evaluation of spray formation, droplet size distribution in the spray, and flow rate of the injector. These parameters are a crucial starting point for spatial CFD evaporation modelling. Moreover, it would be necessary to visualise the spray characteristics and determine the (initial) droplet sizes at various pressures, temperatures, and distances along the spray length. It is therefore recommended to obtain a more advanced experimental setup that could measure the spray and evaporation in engine-like conditions. Especially, the impact of the injection pressure, higher manifold charge pressure, and higher temperatures on the evaporation speed. This

more advanced setup may also give an inside into the evaporation speed of (m)ethanol. Thus, it could be used to validate the single-droplet evaporation model.

Finally, the following recommendations may also be of interest in future experimental research:

1. Additional research into which injector nozzle to install on the Caterpillar G3508A test-engine. This research must determine the most suitable design of a single injector nozzle, or the implementation of multiple injection nozzles into the air inlet manifold; looking at the spray angle, breakup length, droplet size distribution, spray tip penetration, and atomisation.
2. Additional research in determining the exact amount of (m)ethanol being injected into the air inlet manifold for each of the used injection nozzles. This research is recommended as the exact mass flow of (m)ethanol through the various types of injectors is still unknown. It could be determined by measuring the weight decrease over a specific injection timing.
3. Additional research into the effect of ethanol as fuel. In order to compare the results with methanol. Since ethanol is part of the alcohol-family, comparable performances are expected. In addition, no research projects have been found that used ethanol as fuel for marine size engines.
4. Additional research is recommended to analyse the effect of the partial pressure ratio of (m)ethanol vapour in the air, and its effect on the remaining evaporation speed of (m)ethanol being injected.
5. Lastly, the current measuring equipment installed on the experimental setup is insufficient to obtain the desired results. Especially when focused on the evaporation process and speed of the jet spray generated by the nozzle. It is therefore recommended to procure better measuring equipment or implement another measuring technique, such as laser diffraction or phase Doppler particle analysis.

9

Appendix

9.1. Appendix A

<u>Task Risk Analysis – Methanol</u>

Nr.	Activiteiten	Gevaren	Beheersmaatregelen

1.	Vullen van "brandstoftank"	• Lekkage methanol
		• Methanol brand
		• Bloodstelling aan methanol
			• PPE's bij het werken aan het brandstofsysteem;
			   ○ Veiligheidslaarzen of schoencovers
			   ○ Chemisch bestendige kleding // Chemicaliën handschoenen – Ansell Solvex 37-185
			   ○ Volgelaatsmasker met AX filter
			• Brandblusser – CO_2 of BC-poederblusser
			• Minimaal een sluitende veiligheidsbril en nitril/chemicaliën handschoenen aan
			   ○ Chemisch bestendige materialen omvatten butyl rubber of nitril rubber.
			• Gebruik van chemische veiligheidsbril wanneer er een potentieel is voor oogcontact met methanol, inclusief damp.
			   ○ Volledig gelaatsmasker kan over veiligheidsbril worden gedragen voor extra bescherming, maar niet als vervanging voor veiligheidsbril.
			• Chemisch bestendige kleding/ materialen moeten worden gedragen indien herhaaldelijk of langdurig huidcontact met ethanol wordt verwacht. Dit omvat rubberen laarzen, resistente handschoenen en andere ondoordringbare en resistente kleding.
			• Gebouw ventilatie aan en garagedeur geopend // mobiele ventilator stand-by.

2.	Aansluiten en testen van brandstofleidingen	• Lekkage methanol
		• Methanol brand
		• Bloodstelling aan methanol
			• PPE's bij het vullen van de "brandstoftank";
			   ○ Veiligheidslaarzen of schoencovers
			   ○ Chemisch bestendige kleding // Chemicaliën handschoenen – Ansell Solvex 37-185
			   ○ Volgelaatsmasker met AX filter
			• Brandblusser – CO_2 of BC-poederblusser
			• Gebouw ventilatie aan en garagedeur geopend // mobiele ventilator stand-by.

3.	Proefopstelling	• Lekkage methanol
		• Methanol brand
		• Bloodstelling aan methanol
			• Gebruik correcte PPE's:
			   ○ Gelaatsmasker met AX filter
			   ○ Rubberen handschoenen
			   ○ Chemisch bestendige kleding/ handschoenen
			• Ventilatie in testruimte, zowel gebouw gebonden als mobiele ventilatie.
			• Brandblusser – CO_2 of BC-poederblusser

4.	Betreden van ruimte na proef	• Lekkage methanol
		• Methanol brand
		• Bloodstelling aan methanol
			• Toegang tot testruimte alleen bij goede ventilatie
			• Gebouw ventilatie aan en garagedeur geopend // mobiele ventilator stand-by.
			• Correcte PPE's.
			   ○ Veiligheidslaarzen of schoencovers
			   ○ Chemicaliën handschoenen – Ansell Solvex 37-185
			   ○ Volgelaatsmasker met AX filter
			• Brandblusser stand-by en paraat– CO_2 of BC-poederblusser

5.	Ventileren test opstelling na proef	• Lekkage methanol • Methanol brand • Bloodstelling aan methanol	• Zie punt (4) • Mobiele ventilator beschikbaar bij betreden van testruimte en als ventilatie van test box na injectie.
6.	Uit bedrijf nemen van testopstelling	• Lekkage methanol • Methanol brand • Bloodstelling aan methanol	• Zie punt (4) • Leidingen zoveel mogelijk leegspuiten – rest laten verdampen in omgeving met voldoende ventilatie.

<u>Task Risk Analysis – Methanol</u>

Nr.	Activiteiten	Gevaren	Beheersmaatregelen
7.	Eerste hulpmaatregelen	• Lekkage, vrijkomen van methanol.	**Na het inademen:** • Verse lucht of zuurstof toedienen; deskundige medische hulp inroepen. Bij bewusteloosheid ligging en vervoer in stabiele zijligging. • Slachtoffer in de open lucht brengen en rustig neerleggen. **Na huidcontact:** • Onmiddellijk met water en zeep afwassen en goed naspoelen. • Wanneer die huid geïrriteerd blijft, een dokter raadplegen. **Na oogcontact:** • Ogen met open ooglid een aantal minuten onder stromend water afspoelen en dokter raadplegen. • Oogdouche gebruiken – stationair of losse units **Na inslikken:** • Geen braken teweegbrengen • Een brakende, op zijn rug liggende persoon in stabiele zijligging leggen. • Deskundige medische hulp inroepen. • MSDS Methanol – Zie *Sectie 4* – Eerste hulpmaatregelen.
8.	Brandbestrijding	• Lekkage, vrijkomen van methanol, brand.	• Geschikte blusmiddelen: CO_2, BC-bluspoeder, alcoholbestendig schuim, of sproeistraal. ○ Gebruik <u>GEEN</u> volle waterstraal • Brandblusmaatregelen op omgeving afstemmen. • MSDS Methanol – Zie *Sectie 5* – Brandstofbestrijdingsmaatregelen.
9.	Maatregelen accidenteel vrijkomen van methanol	• Blootstelling aan methanol	• MSDS Methanol – Zie *Sectie 6* – Maatregelen bij het accidenteel vrijkomen van methanol

9.2. Appendix B

Task Risk Analysis – Ethanol

Nr.	Activiteiten	Gevaren	Beheersmaatregelen
1.	**Vullen van "brandstoftank"** *Beperk grote van deze "brandstoftank" tot max 2 liter; waarbij 1 liter geprefereerd wordt.*	• Lekkage ethanol • Ethanol brand • Bloodstelling aan ethanol	• PPE's bij het werken aan het brandstofsysteem; 　○ Veiligheidslaarzen of schoencovers 　○ Chemisch bestendige kleding // Chemicaliën handschoenen – Ansell Solvex 37-185 　○ Volgelaatsmasker met AX filter • Brandblusser – CO$_2$ of BC-poederblusser • Minimaal een sluitende veiligheidsbril en nitril/chemicaliën handschoenen aan 　○ Chemisch bestendige materialen omvatten butyl rubber of nitril rubber. • Gebruik van chemische veiligheidsbril wanneer er een potentieel is voor oogcontact met ethanol, inclusief damp. 　○ Volledig gelaatsmasker kan over veiligheidsbril worden gedragen voor extra bescherming, maar niet als vervanging voor veiligheidsbril. • Chemisch bestendige kleding/ materialen moeten worden gedragen indien herhaaldelijk of langdurig huidcontact met ethanol wordt verwacht. Dit omvat rubberen laarzen, resistente handschoenen en andere ondoordringbare en resistente kleding. • Gebouw ventilatie aan en garagedeur geopend // mobiele ventilator stand-by.
2.	**Aansluiten en testen van brandstofleidingen**	• Lekkage ethanol • Ethanol brand • Bloodstelling aan ethanol	• PPE's bij het vullen van de "brandstoftank"; 　○ Veiligheidslaarzen of schoencovers 　○ Chemisch bestendige kleding // Chemicaliën handschoenen – Ansell Solvex 37-185 　○ Volgelaatsmasker met AX filter • Brandblusser – CO$_2$ of BC-poederblusser • Gebouw ventilatie aan en garagedeur geopend // mobiele ventilator stand-by.
3.	**Proefopstelling**	• Lekkage ethanol • Explosie in bak • Ethanol brand • Bloodstelling aan ethanol	• Gebruik correcte PPE's: 　○ Gelaatsmasker met AX filter 　○ Rubberen handschoenen 　○ Chemisch bestendige kleding/ handschoenen • Ventilatie in testruimte, zowel gebouw gebonden als mobiele ventilatie. • Probeer explosielimiet onder de 2.5 vol% te houden (LEL). • Brandblusser – CO$_2$ of BC-poederblusser
4.	**Betreden van ruimte na proef**	• Lekkage ethanol • Explosie in bak • Ethanol brand • Bloodstelling aan ethanol	• Toegang tot testruimte alleen bij goede ventilatie • Gebouw ventilatie aan en garagedeur geopend // mobiele ventilator stand-by. • Correcte PPE's. 　○ Veiligheidslaarzen of schoencovers 　○ Chemicaliën handschoenen – Ansell Solvex 37-185 　○ Volgelaatsmasker met AX filter • Brandblusser stand-by en paraat– CO$_2$ of BC-poederblusser
5.	**Ventileren test opstelling na proef**	• Lekkage ethanol • Ethanol brand • Bloodstelling aan ethanol	• Zie punt (4) • Mobiele ventilator beschikbaar bij betreden van testruimte en als ventilatie van test box na injectie.
6.	**Uit bedrijf nemen van testopstelling**	• Lekkage ethanol • Ethanol brand • Bloodstelling aan ethanol	• Zie punt (4) • Leidingen zoveel mogelijk leegspuiten – rest laten verdampen in omgeving met voldoende ventilatie.

Task Risk Analysis – Ethanol

Nr.	Activiteiten	Gevaren	Beheersmaatregelen
7.	**Eerste hulpmaatregelen**	• Lekkage, vrijkomen van ethanol.	Laat het slachtoffer niet onbeheerd achter. Verplaats slachtoffer uit de gevarenzone. Houd het slachtoffer warm, rustig en bedekt. Verontreinigde kleding onmiddellijk uittrekken. Bij twijfel of bij aanhoudende symptomen een arts raadplegen. Bij bewusteloosheid het slachtoffer in stabiele zijligging leggen. Niets via de mond toedienen. **Na het inademen:** • Zorg voor verse lucht. • Bij onregelmatige ademhaling of ademstilstand direct een arts raadplegen en eerste hulp toedienen. **Na huidcontact:** • Onmiddellijk met water en zeep afwassen en goed naspoelen. • Wanneer die huid geïrriteerd blijft, een dokter raadplegen. **Na oogcontact:** • Contactlenzen verwijderen, indien mogelijk. Blijven spoelen. Minstens 10 minuten met schoon, vloeiend water spoelen, en dokter raadplegen. • Oogdouche gebruiken – stationair of losse units **Na inslikken:** • Geen braken teweegbrengen • Een brakende, op zijn rug liggende persoon in stabiele zijligging leggen. • Deskundige medische hulp inroepen. • MSDS Ethanol – Zie **Sectie 4** – Eerste hulpmaatregelen.
8.	**Brandbestrijding**	• Lekkage, vrijkomen van ethanol, brand.	• Geschikte blusmiddelen: CO$_2$, BC-bluspoeder, alcoholbestendig schuim, of sproeistraal. 　○ Gebruik GEEN volle waterstraal • Brandblusmaatregelen op omgeving afstemmen. • MSDS Ethanol – Zie **Sectie 5** – Brandstofbestrijdingsmaatregelen.
9.	**Maatregelen accidenteel vrijkomen van ethanol.**	• Blootstelling aan ethanol	• MSDS Ethanol – Zie **Sectie 6** – Maatregelen bij het accidenteel vrijkomen van ethanol

9.3. Appendix C

9.3.1. Appendix C.1

To provide a relationship between the temperature and pressure at the interface, during the phase change process, it will be necessary to include the Clausius-Clapeyron equation [36]. The general form of this equation assumes equal pressures across the interface. To avoid this assumption, Lock examined the continuity of the specific Gibbs function. The mathematical description of the Gibbs energy equation is as follows [37]:

$$G = U + pV - TS = H - TS \tag{9.1}$$

Where, G is the Gibbs energy of the system. The fundamental thermodynamic equation for Gibbs energy follows directly from its definition and the fundamental equation for enthalpy. The mathematically description of enthalpy is defined as [37]:

$$H = U + pV \tag{9.2}$$

Where, H is enthalpy of the system, p is pressure, and V is volume. The fundamental thermodynamic equation for enthalpy follows directly from it definition and the fundamental equation for internal energy. The fundamental thermodynamic equation for internal energy follows directly from the first law of thermodynamic and the principle of Clausius, being: $dU = TdS - pdV$. This results in the following fundamental equation for enthalpy, where S is entropy, p is pressure, and V is volume [37].

$$\begin{aligned} dH &= dU + d(pV) \\ dH &= dU + pdV + VdP \qquad \text{where } dU = TdS - pdV \\ dH &= TdS - pdV + pdV + Vdp \\ dH &= TdS + Vdp \end{aligned} \tag{9.3}$$

To conclude, substituting the above mentioned equations into the Gibbs energy equation of Eq. 9.1, results in the following fundamental equation for G [37]:

$$\begin{aligned} G &= U + pV - TS & &= H - TS \\ dG &= dH - d(TS) & &= dH - TdS - SdT \\ dG &= \cancel{TdS} + Vdp \cancel{-TdS} - SdT \\ dG &= Vdp - SdT & &= \widehat{V}\frac{dp}{dt} - \widehat{S}\frac{dT}{dt} \end{aligned} \tag{9.4}$$

Where, p and T are the pressure and temperature respectively. By assuming continuity of the specific Gibbs function across the interface, it is possible to equate the above equation on either side of the interface. This requires the use of the Clausius-Clapeyron equation.

The Clausius-Clapeyron equation relates the latent heat (heat of transformation) of vaporisation or condensation to the rate of change of vapour pressure with temperature. In case a liquid is in equilibrium with its vapour (i.e. at its boiling point), the specific Gibbs free energies of liquid and vapour are equal. The same is true for the molar Gibbs free energies. This results therefore in the following equation [55]:

$$\begin{aligned} H_1 - TS_1 &= H_2 - TS_2 \\ T(S_2 - S_1) &= H_2 - H_1 \end{aligned} \tag{9.5}$$

Where, H is the enthalpy and S the entropy. To simplify Eq. 9.5, the following equations for latent heat (L) and specific volume ($\widehat{V}$) could be substituted [56]. Where, ρ is the density, and subscripts l and v refer to the liquid and vapour phase.

$$\begin{aligned} L &= H_2 - H_1 \\ \widehat{V} &= \frac{V}{m} = \frac{1}{\rho} \\ [\widehat{V_v} - \widehat{V_l}] &= [\frac{1}{\rho_v} - \frac{1}{\rho_l}] \end{aligned} \tag{9.6}$$

This results in:

$$L = T(S_2 - S_1)$$
$$L = T \cdot \hat{S}$$
$$\hat{S} = \frac{L}{T}$$

(9.7)

With some further manipulation using the Gibbs function mentioned above, the following modified form of the Clausius-Clapeyron equation is obtained [34]:

$$dG = \hat{V}\frac{dp}{dt} - \hat{S}\frac{dT}{dt}$$
$$dG_l = dG_v$$
$$\hat{V}dp = \hat{S}dT$$
$$\left[\frac{1}{\rho_v} - \frac{1}{\rho_l}\right]dp = \frac{L}{T}dT$$
$$\frac{1}{\rho_v}\frac{dp_v}{dt} - \frac{1}{\rho_l}\frac{dp_l}{dt} = \frac{L}{T_v}\frac{dT_v}{dt}$$

(9.8)

Collectively, these equations and boundary conditions form a closed system; however, solving such a highly coupled and non-linear system presents a challenging task. Thus, some simplifications are necessary.

9.3.2. Appendix C.2
Original system of equations
Inside the droplet
Heat flux at $r = 0$:

$$\frac{\partial T_l}{\partial r}(0, t) = 0 \tag{9.9}$$

Conservation of heat:

$$\frac{\partial T_l}{\partial t} = \frac{v_1}{r^2} \frac{\partial}{\partial r}\left(r^2 \frac{\partial T_l}{\partial r}\right) \tag{9.10}$$

Outside the droplet
Conservation of mass:

$$\frac{\partial \rho_v}{\partial t} = -\frac{1}{r^2} \frac{\partial\left(\rho_v r^2 u_v\right)}{\partial r} \tag{9.11}$$

Conservation of momentum:

$$\rho_v\left[\frac{\partial u_v}{\partial t} + u_v \frac{\partial u_v}{\partial r}\right] = -v_2 \frac{\partial(\rho_v T_v)}{\partial r} \tag{9.12}$$

Conservation of heat:

$$\rho\left[\frac{\partial T_v}{\partial t} + u_v \frac{\partial T_v}{\partial r}\right] = \frac{v_3}{r^2} \frac{\partial}{\partial r}\left[r^2 \frac{\partial T_v}{\partial r}\right] - \frac{v_4 \rho_v T_v}{r^2} \frac{\partial(r^2 u_v)}{\partial r} \tag{9.13}$$

At the interface
Continuity of temperature:

$$T_l = v_5 T_v \tag{9.14}$$

Continuity of heat flux:

$$\frac{\partial T_v}{\partial r} = v_6 \frac{\partial T_l}{\partial r} - v_7 \frac{dR}{dt} \tag{9.15}$$

Continuity of mass flux:

$$\rho_v\left[u_v - \frac{dR}{dt}\right] = -v_8 \frac{dR}{dt} \tag{9.16}$$

Clausius-Clapeyron Equation:

$$\frac{1}{\rho_v}\left[\frac{\partial(\rho_v T_v)}{\partial t} + \frac{dR}{dt} \frac{\partial(\rho_v T_v)}{\partial r}\right] = \frac{1}{v_8}\left[\frac{\partial p_l}{\partial t} + \frac{dR}{dt} \frac{\partial p_l}{\partial r}\right] + \frac{v_9}{T_v}\left[\frac{\partial T_v}{\partial t} + \frac{dR}{dt} \frac{\partial T_v}{\partial r}\right] \tag{9.17}$$

Pressure jump condition:

$$\rho_v T_v = p_l - \frac{v_{10}\sigma}{R} + v_{11} u_v \frac{dR}{dt} \tag{9.18}$$

Where, the proportionality constants v_1–v_{11}, T_i, and t_0 are written as:

v_1	$\dfrac{\lambda_l \cdot t_0}{\rho_l \cdot c_{vl} \cdot R_{initial}^2}$	v_7	$\dfrac{L \cdot \rho_l \cdot R_{initial}^2}{\lambda_v \cdot T_\infty \cdot T_0}$
v_2	$\dfrac{\rho_\infty \cdot T_\infty}{\rho_l \cdot T_l}$	v_8	$\dfrac{\rho_l}{\rho_\infty}$
v_3	$\dfrac{\lambda_v \cdot t_0}{\rho_\infty \cdot c_{vv} \cdot R_{initial}^2}$	v_9	$\dfrac{L}{\widehat{R} \cdot T_\infty}$
v_4	$\dfrac{\widehat{R}}{c_{vv}} \rightarrow \widehat{R} = \dfrac{R}{M}$	v_{10}	$\dfrac{1}{2 \cdot \rho_\infty \cdot \widehat{R} \cdot T_\infty \cdot R_{initial}}$
v_5	$\dfrac{T_\infty}{T_l}$	v_{11}	$T_i \rightarrow \quad T_i = \dfrac{L}{\widehat{R}} \cdot \dfrac{\left[\dfrac{T_b}{\frac{L}{\widehat{R}} - T_b \cdot log(\frac{\phi \cdot p_{vsat}}{p_b})}\right]}{T_\infty}$
v_6	$\dfrac{\lambda_l \cdot T_l}{\lambda_v \cdot T_\infty}$	t_0	$\dfrac{L \cdot \rho_l \cdot R_{initial}^2}{\lambda_v \cdot T_\infty}$

9.3.3. Appendix C.3
Reduced system of equations
Assuming $\frac{1}{v_2}$ and v_{11} are negligible.

Inside the droplet (Equations remain unchanged)
Heat flux at $r = 0$:

$$\frac{\partial T_l}{\partial r}(0, t) = 0 \tag{9.19}$$

Conservation of heat:

$$\frac{\partial T_l}{\partial t} = \frac{v_1}{r^2}\frac{\partial}{\partial r}\left(r^2 \frac{\partial T_l}{\partial r}\right) \tag{9.20}$$

Initial conditions

$$T_l(r, 0) = 1 \quad ; \quad R(0) = 1 \quad ; \quad u_l(r, t) = 0$$

Outside the droplet
Conservation of mass:

$$\frac{1}{T_v}\left[\frac{\partial T_v}{\partial t} + u_v \frac{\partial T_v}{\partial r}\right] = \frac{1}{r^2}\frac{\partial(r^2 u_v)}{\partial r} \tag{9.21}$$

Conservation of heat:

$$\frac{\partial T_v}{\partial r} = \left(\frac{1 + v_4}{v_3}\right)u_v \tag{9.22}$$

Initial conditions

$$T_v(r, 0) = 1 \quad ; \quad u_v(r, 0) = 1$$

Boundary condition as $r \to \infty$:

$$T_v(r, t) = 1 \tag{9.23}$$

At the interface
Continuity of temperature:

$$T_l = v_5 T_v \tag{9.24}$$

Continuity of heat flux:

$$\frac{\partial T_v}{\partial r} = v_6 \frac{\partial T_l}{\partial r} - v_7 \frac{dR}{dt} \tag{9.25}$$

Continuity of mass flux:

$$\frac{dR}{dt} = \frac{u_v}{1 - v_8 T_v} \tag{9.26}$$

Clausius-Clapeyron Equation:

$$\frac{v_{10}\sigma}{R^2} = \frac{v_8 v_9}{T_v}\left[\frac{\partial T_v}{\partial t} + \frac{dR}{dt}\frac{\partial T_v}{\partial r}\right] \tag{9.27}$$

9.4. Appendix D

Below an estimate of the horizontal direction of a droplet at terminal velocity for laminar flow (Stokes flow), and neglecting its vertical component [53]. In order to determine the horizontal distance a droplet travels in a laminar flow, the derivation starts with the force balance in x-direction [53]. This force balance is written as:

$$F_x = ma_x \longrightarrow a_x = \frac{F_x}{m}$$

Next, the resistance force on the droplet in laminar flow is calculated, where $V_d = \frac{1}{6}\pi D^3$, $S = \frac{\pi D^2}{4}$, and for laminar flows the drag coefficient is $C_D = \frac{24}{Re} \rightarrow C_D = \frac{24\mu}{\rho V D}$.

$$F_D = C_D \frac{1}{2}\rho v^2 S = \frac{24}{Re}\frac{1}{2}\rho v^2 S = \frac{12\mu}{\rho V D}\rho v^2 \frac{\pi D^2}{4} = 3\pi\mu D v$$

The acceleration divided by the density and volume results in:

$$a = \frac{-F_D}{m} = \frac{-3\pi\mu D v}{mV_d} = \frac{-3\pi\mu D v}{\rho\frac{1}{6}\pi D^3} = -\frac{18\mu v}{\rho D^2}$$

The horizontal acceleration as function of $a = f(v, \mu, \rho, D)$ results in:

$$a = -\frac{18\mu v}{\rho D^2}$$

Now, the velocity can be calculated using the following equation:

$$v = v_0 + at = v_0 - \frac{18\mu v}{\rho D^2}t$$

Rewriting the velocity as function of the variables and parameters of $v = f(v_0, \mu, \rho, D, t)$ gives:

$$v(1 + \frac{18\mu t}{\rho D^2}) = v_0 \longrightarrow v = \frac{v_0}{1 + \frac{18\mu t}{\rho D^2}} = \frac{v_0\rho D^2}{\rho D^2 + 18\mu t}$$

This results in the final equation for horizontal distance:

$$x = x_0 + vt = x_0 + \frac{v_0\rho D^2}{\rho D^2 + 18\mu t}t$$

Bibliography

[1] International Monetary Fund. *World Economic Outlook Update*. 2022. URL: `https://www.imf.org/en/Publications/WEO/Issues/2022/01/25/world-economic-outlook-update-january-2022`.

[2] UN Conference on Trade and Development. *Review of the Maritime Transport 2019*. 2019. URL: `https://unctad.org/system/files/official-document/rmt2019ch1_en.pdf`.

[3] UK Research and Innovation. *Shipping industry reduces carbon emissions with space technology*. 2021. URL: `https://www.ukri.org/news/shipping-industry-reduces-carbon-emissions-with-space-technology/`.

[4] DNV. *Future Fuels*. URL: `https://www.dnv.com/maritime/hub/decarbonize-shipping/fuels/future-fuels.html`.

[5] L. van Biert et al. "A review of fuel cell systems for maritime applications". In: *Journal of Power Sources* 327 (2016). ISSN: 03777753. DOI: `10.1016/j.jpowsour.2016.07.007`.

[6] A.P. Moller - Maersk. *A.P. Moller - Maersk accelerates fleet decarbonisation with 8 large ocean-going vessels to operate on carbon neutral methanol*. 2021. URL: `https://www.maersk.com/news/articles/2021/08/24/maersk-accelerates-fleet-decarbonisation`.

[7] R.G. van de Ketterij. "Impact of Methanol on the combustion process - An experimental study". In: (2020).

[8] Methanol Institute. *Measuring Maritime Emissions - Policy recommendations regarding GHG accounting of the maritime industry*. 2020. URL: `%5Curl%7Bhttps://www.methanol.org/wp-content/uploads/2020/04/Methanol-Institute-Measuring-Maritime-Emissions-Policy-Paper-August-2021.pdf%7D`.

[9] R. Edwards, J-F. Larivé, D. Rickeard. "Well-to-tank report 4.a – JRC well-to-wheels analysis". In: (2014).

[10] DNV GL. "Methanol as marine fuel: Environmental benefits, technology readiness, and economic feasibility". In: (2016).

[11] J.J. Bosklopper. *Experimental and simulation based investigation of the performance of a 100% methanol port-injected spark-ignited engine*. `https://repository.tudelft.nl/islandora/object/uuid%3A946dbdf6-ea99-4f57-8441-5a012e704d37?collection=education`. 2020.

[12] Dong Wei Yao, Xin Chen Ling, and Feng Wu. "Evaporate prediction and compensation of intake port wall-wetting fuel film for spark ignition engines fueled with ethanol-gasoline blends". In: *Journal of Zhejiang University: Science A* 13 (8 2012). ISSN: 1673565X. DOI: `10.1631/jzus.A1200068`.

[13] Jiyuan Zeng. "Modelling and Simulation of the Diesel Engine Injection Systems". 2019.

[14] R.S. Tol. *Combustion of diesel/methanol blends in a compression ignited engine*. `https://repository.tudelft.nl/islandora/object/uuid%3A51d875d8-19cf-4397-8755-680de1cbc080?collection=education`. 2020.

[15] Thermopedia. *Shadowgraph Technique*. 2011. URL: `https://www.thermopedia.com/content/1117/`.

[16] Avinash Kumar Agarwal et al. *Methanol and the Alternate Fuel Economy*. Springer, 2019.

[17] Sebastian Verhelst et al. "Methanol as a fuel for internal combustion engines". In: *Progress in Energy and Combustion Science* 70 (2019), pp. 43–88. ISSN: 03601285. DOI: `10.1016/j.pecs.2018.10.001`.

[18] Nasser Ashgriz. *Handbook of Atomization and Sprays*. 2011.

[19]   John B. Heywood. *Internal Combustion Engine Fundamentals*. 1988.

[20]   R. D. Reitz and F. B. Bracco. "On the dependence of spray angle and other spray parameters on nozzle design and operating conditions". In: *SAE Technical Papers* (1979). ISSN: 26883627. DOI: `10.4271/790494`.

[21]   Xibin Wang et al. "Spray characteristics of high-pressure swirl injector fueled with alcohol". In: *Frontiers of Energy and Power Engineering in China* 1 (1 2007). ISSN: 16737393. DOI: `10.1007/s11708-007-0012-z`.

[22]   Wugao Zhang et al. "Experimental study of the spray characteristics of USLD, methanol and DME on the swirl nozzle of a Stirling engine". In: *Fuel Processing Technology* 119 (2014). ISSN: 03783820. DOI: `10.1016/j.fuproc.2013.10.006`.

[23]   Wei Zeng et al. "Atomization and vaporization for flash-boiling multi-hole sprays with alcohol fuels". In: *Fuel* 95 (2012). ISSN: 00162361. DOI: `10.1016/j.fuel.2011.08.048`.

[24]   Min Xu et al. "Flash Boiling: Easy and Better Way to Generate Ideal Sprays than the High Injection Pressure". In: *SAE International Journal of Fuels and Lubricants* 6 (1 2013). ISSN: 19463960. DOI: `10.4271/2013-01-1614`.

[25]   Sanghoon Lee and Sungwook Park. "Experimental study on spray break-up and atomization processes from GDI injector using high injection pressure up to 30MPa". In: *International Journal of Heat and Fluid Flow* 45 (1 2014). ISSN: 0142727X. DOI: `10.1016/j.ijheatfluidflow.2013.11.005`.

[26]   Anupam Ghosh, Prasad Boggavarapu, and R. V. Ravikrishna. "Measurement of liquid and vapor penetration of evaporating methanol sprays". In: *Atomization and Sprays* 30 (10 2021). ISSN: 10445110. DOI: `10.1615/ATOMIZSPR.2020034377`.

[27]   L. Dodge and D. Naegeli. "Injector Spray Characterization of Methanol in Reciprocating Engines". In: *Southwest Research Institute* (1994).

[28]   Wikipedia. *Vacuum ejector*. 2022. URL: `https://en.wikipedia.org/wiki/Vacuum_ejector#cite_ref-hv_1-1`.

[29]   J. U. Thoma and Alan S. Perelson. "Introduction to Bond Graphs and Their Applications". In: *IEEE Transactions on Systems, Man, and Cybernetics* SMC-6 (11 2008). ISSN: 0018-9472. DOI: `10.1109/tsmc.1976.4309468`.

[30]   Dariusz Szpica and Michał Kusznier. "Modelling of the Low-Pressure Gas Injector Operation". In: *Acta Mechanica et Automatica* 14 (1 2020). ISSN: 18984088. DOI: `10.2478/ama-2020-0005`.

[31]   André Morais Ferreira et al. "Development of 1D Simulation Model of Fuel Injector for PFI Application". In: (2017). DOI: `10.5151/engpro-simea2017-13`.

[32]   Niculescu Titu. *Chapter 2: Study of Inductive-Capacitive Series Circuits Using the Simulink Software Package*. May 2012. ISBN: ISBN 978-953-51-0635-7. DOI: `10.13140/2.1.3883.4245`.

[33]   N. H. Chung, B. G. Oh, and M. H. Sunwoo. "Modelling and injection rate estimation of common-rail injectors for direct-injection diesel engines". In: *Proceedings of the Institution of Mechanical Engineers, Part D: Journal of Automobile Engineering* 222 (6 2008). ISSN: 09544070. DOI: `10.1243/09544070JAUTO647`.

[34]   Joel Alroe, A Prof T Farrell, and S Psaltis. "Modelling the Evaporation of a Liquid Droplet". In: *National Collaboration in the Mathematical Sciences* (February 2013).

[35]   R Byron Bird, Warren E Stewart, and Edwin N Lightfoot. "Transport Phenomena, Revised 2nd Edition". In: *John Wiley & Sons, Inc.* (2006). ISSN: 01436112.

[36]   G S H Lock. "Latent Heat Transfer: An Introduction to Fundamentals, by G.S.H. Lock, Oxford University Press, UK (1994). 288 pages. ISBN 0-19-856284-5." In: *Developments in Chemical Engineering and Mineral Processing* 5 (2008).

[37]   Andreana Rosnik. *Differential Forms of Fundamental Equations*. 2020. URL: `https://chem.libretexts.org/Bookshelves/Physical_and_Theoretical_Chemistry_Textbook_Maps/Supplemental_Modules_(Physical_and_Theoretical_Chemistry)/Thermodynamics/Energies_and_Potentials/Differential_Forms_of_Fundamental_Equations`.

[38] Purdue University. *Deviations from Ideal Gas Law Behaviour*.

[39] A. W. Bush. *Perturbation Methods for Engineers and Scientists*. 2018. DOI: `10.1201/9780203743775`.

[40] J. Crank. "The mathematics of diffusion. 2nd Edn." In: (1979). ISSN: 0031-9112. DOI: `10.1088/0031-9112/26/11/044`.

[41] S. V. Patankar. "Numerical heat transfer and fluid flow." In: (1980). ISSN: 0029-5639. DOI: `10.13182/nse81-a20112`.

[42] A. J.H. McGaughey and C. A. Ward. "Temperature discontinuity at the surface of an evaporating droplet". In: *Journal of Applied Physics* 91 (10 I 2002). ISSN: 00218979. DOI: `10.1063/1.1471363`.

[43] National Institute of Standards and Technology. *Methyl Alcohol*. 2021. URL: `https://webbook.nist.gov/cgi/cbook.cgi?ID=C67561%5C&Mask=4%5C&Type=ANTOINE%5C&Plot=on#ref-2`.

[44] D Ambrose and C H S Sprake. "Thermodynamic properties of organic oxygen compounds XXV. Vapour pressures and normal boiling temperatures of aliphatic alcohols". In: *The Journal of Chemical Thermodynamics* 2 (5 1970), pp. 631–645. ISSN: 0021-9614. DOI: `https://doi.org/10.1016/0021-9614(70)90038-8`. URL: `https://www.sciencedirect.com/science/article/pii/0021961470900388`.

[45] Robert D. Goodwin. "Methanol Thermodynamic Properties From 176 to 673 K at Pressures to 700 Bar". In: *Journal of Physical and Chemical Reference Data* 16 (4 1987). ISSN: 15297845. DOI: `10.1063/1.555786`.

[46] W. Merzkirch. "Flow visualization. Second edition." In: (1987).

[47] *Springer Handbook of Experimental Fluid Mechanics*. 2007. DOI: `10.1007/978-3-540-30299-5`.

[48] L Bromberg and W K Cheng. *Methanol as an alternative transport fuel in the US: Options for sustainable and/or energy-secure transportation*. 2010.

[49] Paul A. MacHiele. "Flammability and toxicity tradeoffs with methanol fuels". In: 1987. DOI: `10.4271/872064`.

[50] Paul A. MacHiele. "Summary of the fire safety impacts of methanol as a transportation fuel". In: 1990. DOI: `10.4271/901113`.

[51] International Programme on Chemical Safety - World Health Organization. "Health and Safety Guide No. 105 - Methanol Health and Safety Guide". In: (Geneva). 1997.

[52] Hibbeler R. C. *Fluid mechanics*. Pearson, 2015.

[53] R. de Kat. "TSTL 28 oktober 2020 – Opgave 5: Uitwendige stromingen". In: *Netherlands Defence Academy* (2020).

[54] Centers for Disease Control and Prevention. *Generation and Behavior of Airborne Particles (Aerosols)*. 2011. URL: `https://www.cdc.gov/niosh/topics/aerosols/pdfs/aerosol_101.pdf`.

[55] Jeremy Tatum. *The Clausius-Clapeyron Equation*. 2020. URL: `https://phys.libretexts.org/Bookshelves/Thermodynamics_and_Statistical_Mechanics/Book%5C%3A_Heat_and_Thermodynamics_(Tatum)/14%5C%3A_The_Clausius-Clapeyron_Equation`.

[56] Jeremy Tatum. *Latent Heat and Enthalpy*. 2020. URL: `https://phys.libretexts.org/Bookshelves/Thermodynamics_and_Statistical_Mechanics/Book%5C%3A_Heat_and_Thermodynamics_(Tatum)/09%5C%3A_Enthalpy/9.03%5C%3A_Latent_Heat_and_Enthalpy`.